ORNL/TM-5534

Effect of Steam Corrosion on Core Post Strength Loss: I. Low, Chronic Steam Ingress Rates

R. P. Wichner

OAK RIDGE NATIONAL LABORATORY
OPERATED BY UNION CARBIDE CORPORATION FOR THE ENERGY RESEARCH AND DEVELOPMENT ADMINISTRATION

Printed in the United States of America. Available from
National Technical Information Service
U.S. Department of Commerce
5285 Port Royal Road, Springfield, Virginia 22161
Price: Printed Copy $4.50; Microfiche $2.25

ORNL/TM-5534
Dist. Category UC-77

Contract No. W-7405-eng-26

CHEMICAL TECHNOLOGY DIVISION

EFFECT OF STEAM CORROSION ON CORE POST STRENGTH LOSS: I. LOW, CHRONIC STEAM INGRESS RATES

R. P. Wichner

Date Published: October 1976

OAK RIDGE NATIONAL LABORATORY
Oak Ridge, Tennessee 37830
operated by
UNION CARBIDE CORPORATION
for the
ENERGY RESEARCH AND DEVELOPMENT ADMINISTRATION

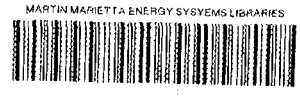

TABLE OF CONTENTS

EFFECT OF STEAM CORROSION ON CORE POST STRENGTH LOSS: I. LOW, CHRONIC STEAM INGRESS RATES

R. P. Wichner

ABSTRACT

The purpose of this study was to assess the effect of chronic, low levels of steam ingress into the primary system of the HTGR on the corrosion, and consequent strength loss of the core support posts. The assessment necessarily proceeds through the following three steps: (1) The impurity composition in the primary system was estimated as a function of a range of steady ingress rates of from 0.001 to 1.0 g/sec, both by means of an analysis of the Dragon steam ingress experiment and a computer code, TIMOX, which treats the primary system as a well-mixed pot. (2) The core post burnoffs which result from 40-year exposures to these determined impurity atmospheres were then estimated using a corrosion rate expression derived from published ATJ-graphite corrosion rate data. Burnoffs were determined for both the core posts at the nominal and the maximum sustained temperature, estimated to be 90°C above nominal. (3) The final step involved assessment of the degree of strength loss resulting from the estimated burnoffs. An empirical equation was developed for this purpose which compares reasonably well with strength loss data for a number of different graphites and specimen geometries.

Steps (1) and (2) yield an error band of predicted burnoffs with varying ingress rate for both the nominal and hot core posts. Step (3) was used to estimate a burnoff range which may cause 50% strength loss – the maximum allowable degree of strength loss – for both the nominal and hot core posts. A method was developed for estimating the probability for 50% strength loss for the general case of overlapping error bands.

The results show that the nominal core posts have small probability (8%) for 50% strength loss even at the maximum assumed 40-year ingress rate of 1 g/sec (corresponding to 850 vpm* total oxygen). The nominal core posts have 0% probability of 50% strength loss for ingress rates below 0.025 g/sec (20 vpm total oxygen). The hot core posts show significantly greater probability for 50% strength loss: 50% at 0.004 g/sec ingress (3.4 vpm total oxygen), 80% at 0.007 g/sec (6 vpm total oxygen), and 100% probability for ingress rates above 0.01 g/sec (9 vpm total oxygen).

---

*vpm = parts per million on a volumetric basis.

Thus, a major problem this study calls to attention is the potentially excessive loss of graphite strength in the hotter core post regions. It is recommended that a more accurate definition of the size, location, and temperature excess of the sustained core post hot zones (created by regional power peaking, hot streaking, and non-ideal coolant flow distributions) be obtained.

Modest changes in purification rate appear to have minor effect on the degree of strength loss. Significantly improved results begin to show only for purification flows above about five times the nominal rate. Similarly, modest changes in core temperature do not significantly affect core post strength loss. In some cases, small increases in temperature are shown to benefit the core posts because of improved oxidant gettering by the core and the increased tendency for the corrosion to be confined to a narrower surface zone, which results in lower strength loss.

1. INTRODUCTION

1.1 Objective and Method

The objective of this study was to assess the effect of slow, long-term steam leakages into the primary system of the HTGR on the corrosion, and consequent strength loss, of the core posts.*

As the first step in the approach to the problem, the impurity level and composition in the primary coolant for series of assumed steady-state ingress rate were estimated. No attempt was made to calculate ingress rates. Instead, the rate of steam inleakage was treated as a parameter ranging from 0.001 g/sec, which corresponds to a total oxygen level of 0.85 vpm (parts per million on a volumetric basis) at the nominal purification rate in the reference plant, to 1.0 g/sec, which corresponds to 850 vpm total oxygen. While the total impurity level depends solely on the steam inleakage and purification rates, the composition of the impurity atmosphere also depends on the reaction rate of steam with the core graphite.

Two basic methods were used to determine effective core reactivity to steam and the resulting impurity composition. Section 5.2 describes one method based on the analysis of steam ingress experiments performed at the Dragon Reactor. A second method, outlined in Sect. 5.3, utilizes a computer program that treats the primary coolant as a well-stirred pot. The core graphite is separated into four reactive zones, each characterized by an appropriately weighted mean temperature calculated from a more detailed temperature distribution. Impurity compositions are computed by the program as a function of time following the onset of a steady-steam ingress until steady state conditions are reached. The calculations are carried through employing three published corrosion rate equations as an estimate of the core reactivity to steam corrosion. These three estimates, together with impurity compositions extracted using the Dragon ingress data, yield a band of equilibrium impurity compositions as a function of rate of steam ingress.

---

*In this report, the term "core post strength" refers solely to the compressive strength of the body of the post. Consideration of the contact stresses at each end of the post is excluded.

The second step in the assessment was the estimation of the extent of long-term corrosion experienced by the core posts as a consequence of exposure to the above determined impurity compositions. A corrosion rate equation for ATJ graphite,* the reference core-post material, was derived for this purpose from published rate data taken under reasonably representative conditions of temperature and impurity concentraions (see Sect. 4.1). The uncertainties inherent in the use of the derived equations for predicting ATJ corrosion rates are significant; these are detailed in Sect. 4.1. Nevertheless, corrosion rates predicted for ATJ fall within a band of estimates using other rate equations and generally follow similar trends.

The final step in the assessment was to correlate the estimated 40-year core post burnoffs with strength loss. An empirical strength loss model is developed in Sect. 6.1 based on the concept that the fractional strength degradation of a graphite member is related to the ratio of an effective corrosion depth to member size. The effective corrosion depth is determined by computing the surface burnoff (the so-called onion skin burnoff) multiplied by a penetration factor, which varies inversely with temperature. The penetration factor is estimated from published strength loss data in the temperature range of 950 to 1030°C. Extrapolating the correlation down to core-post temperatures involves considerable uncertainty; consequently, a range of penetration factors are assumed for the core posts that yield a range of estimates for strength loss.

In Sect. 6.4, the estimated range of 40-year burnoffs is compared with the estimated range required to cause 50% core post strength loss (called the target burnoff) at both the nominal and upper sustained core post temperatures.

Intersecting error bands of estimated and target burnoffs yield some nonzero probability for 50% strength loss. A method for computing this probability is described in Appendix A, based on the assumption that each error band represents a zone in which the estimated burnoff (or target burnoff) could lie with equal probability. Probabilities for reaching

---

*ATJ is the registered tradename for a type of graphite manufactured by Carbon Products Division of Union Carbide.

50% core post strength loss for a range of assumed steam ingress rates are calculated in Sect. 6.4 by using this assumption of flat frequency function within each error band.

1.2 Interim Nature of This Study

A number of developments were known to be in progress during the course of this study that may have a significant impact on the calculated results. Most notable is the projected increase in the diameter of the core support posts from 6 in., specified in GASSAR-6,[1] to a range of from 7-3/4 in. directly under the core to 9 in. around the periphery. A second design change being considered is the replacement of ATJ as a prime candidate for the core post material with an alternate graphite, possibly Stackpole 2020. The change of graphite type will probably have less of an impact on the conclusions than the projected change in diameter.

In addition, corrosion rate constants for the reference core graphite, H-451, are still being developed and should be available soon. Use of these new values would tend to diminish some of the uncertainties of this assessment, since the reactivity to steam corrosion of the core graphite determines the oxidizing environment that the core posts experience for any given steam ingress rate. In the absence of rate constants specific to the reference-core graphite, several kinetics expressions for a number of graphites were selected from the literature, which yielded a range of calculated impurity compositions. It would therefore appear advisable to repeat these calculations at an opportune time using the newly established post dimensions and revised kinetics constants for the core graphite.

1.3 Reference Reactor Parameters

This study began at a time when the principal authoritative summary of HTGR reactor parameters was the Delmarva Power PSAR.[2] For this reason, and because the first licensing actions for HTGRs would relate to reactors of this size, the 2000 MW(t) HTGR was selected for this study. In the course of the analysis, a need arose for core temperature distribution data exceeding in detail those provided by the PSAR. This additional

detail was provided by General Atomic Company (GAC) via informal transmission of a portion of a safety analysis report that was published later.[3] The temperature levels however differed, the exit coolant temperatures from the core being about 30°C higher in the later safety study as compared with the Delmarva PSAR.

Hence basically, the reference reactor selected for this study is a 2000 MW(t), Summit-type reactor employing the higher temperature levels indicated by ref. 3. The anticipated effect of this modest temperature difference on the results is shown in Sect. 6.4 to be minor.

Finally, GASSAR-6 became available rather late so that no GASSAR-6 parameters were adopted which would have required major calculational revisions. However, wherever otherwise possible, GASSAR-6 was used as the most recent authoritative source for design dimensions, material properties or other descriptive information. Table 1.1 lists the pertinent parameters of the reference reactor used in this study.

1.4 Flaw Sizes to Yield Assumed Inleakage Rates

It is well to have in mind some approximate scale of the flaws in the steam generator tubing that would result in the range of inleakage flows assumed in this study. Two cases will be examined, each of which was selected to avoid two-phase flow: (1) a tubing flaw located near the feedwater inlet of the steam generator where the water temperature is sufficiently low so that decompression to the helium side pressure does not cause vaporization; (2) a tubing flaw sufficiently far into the superheater region so that isenthalpic expansion within the flaw does not bring the steam into the two-phase region.

1.4.1 Inleakage of water

For the first case, the water side pressure near the feedwater inlet is about 2980 psi (20.5 MPa), and is opposed by 705 psi (4.86 MPa) on the helium side. Since a vapor pressure of 705 psi (4.86 MPa) corresponds to a temperature of 500°F (260°C), it may be presumed that water leaks below 500°F (260°C) will pass through the flaw as liquid water. A test calculation shows that pinhole water leaks will not be limited by sonic velocity.

Table 1.1. Reference reactor characteristics

	Common units	Metric units
Thermal power	2000 MW	
Coolant		
Inlet pressure	49.3 atm	5.00 MPa
Core pressure drop	11.3 psi	0.0779 MPa
Flow rate	7.3E6 lb_m/hr[a]	3.3E6 kg/hr
Inlet temperature	641°F	338°C
Exit temperature	1446°F	786°C
Core temperature distribution	b	-
Average velocity	130 ft/sec	39.6 m/sec
Helium inventory	15,000 lb_m	6700 kg
Volume	81,000 ft^3	2300 m^3
Coolant channels		
Diameter	0.827 in.	2.10 cm
Total surface area	103,000 ft^2	9,570 m^2
Length of active core	20.8 ft	6.34 m
Number per element	72	72
Purification rate	2070 lb_m/hr	939 kg/hr
Core posts		
Diameter	6 in.	15.2 cm
Length	7.1 ft	2.16 m
Number	255	255
Initial compressive strength	10,000 psi	68.9 MPa
Nominal temperature	1446°F	786°C
Estimated maximum sustained temperature	1608°F	876°C
Initial safety factor	10	10

[a]Notation 1.0E6 signifies 1.0×10^6.

[b]See Table 5.8.

We may approximate the flow through an assumed cylindrical pinhole of the diameter, d_j, by equating the driving pressure to the sum of the expansion-contraction pressure loss of approximately two velocity heads and the flow resistance with the flaw; that is,

$$\Delta p = (2 + \frac{L}{40\ d_j}) \frac{1}{2} \rho u_j^2 \quad , \tag{1}$$

where u_j is the velocity in the flaw, and L is the tubing wall thickness of about 0.13 in. (0.33 cm). The term $L/40\ d_j$ approximately equals the frictional resistance in the flaw in terms of velocity head-pressure loss. The leakage mass flow rate is given by:

$$w_s = \rho u_j \frac{\pi}{4} d_j^2 \quad . \tag{2}$$

Equation (2) may be substituted into Eq. (1) to yield the flaw size, d_j, which corresponds to an assumed value for the leakage rate.

The results for cases of interest are shown in Table 1.2. Rather small tubing flaws cause the range of inleakage flow rates assumed in this study. The inleakage flow of 0.01 g/sec, which corresponds approximately to a total oxygen level of 10 vpm at the nominal purification flow, is seen to result from pinhole flaw of about 0.6 mil in the water leakage regime.

Table 1.2. Flaw sizes for a range of inleakage flows in the water regime near the feedwater inlet, calculated by using Eqs. (1) and (2)

Leak rate (g/sec)	Flaw size, d_j (mil)	(μm)	Leakage velocity in flaw (ft/sec)	(m/sec)
0.001	0.22	5.6	160	49
0.01	0.59	15.0	240	73
0.1	1.6	41.0	330	100
1.0	4.5	110.0	400	120

The interesting experiments of C. Harper et al.[4] on the behavior of small water leaks in high-pressure mild-steel boiler tubing are worth noting here. The results of several runs at various initial manufactured flaw sizes are shown in Table 1.3. The wall thickness used was about one-half of the 0.13 in. (0.33 cm) assumed above, and the water temperature was sufficiently high (about 660°F or 349°C) so that the leakage probably flashed into the two-phase region; therefore, the results are not directly comparable.

Two important conclusions may be drawn from the test data summarized in Table 1.3:

(1) There appears to be a critical flaw size in these tests below which corrosion debris seals the leak and above which the leak increases with time. This critical size is bracketed between 2 mil (51 μm), which yielded leakage rates that increased from about 0.4 to about 3 g/sec, and 0.6 mil (15 μm) below which leaks quickly plugged.

(2) The second conclusion drawn from these experiments is that the mechanics of slow leaks driven by a high-pressure driving force is a rather complex phenomenon. In no case was it found possible to generate a time-steady, slow leak. Leakage flows which did not plug varied greatly with time, reflecting accumulation of corrosion debris or erosion due to high velocities. Occasionally, thermal cycling would break loose a plugged flaw.

It should be emphasized that the results of Harper et al.[4] pertain to the particular condition of this experiment, with respect to tubing material, wall thickness, water pressure, and temperature. Since the mechanics are not well understood, it is not possible to generalize these observations to other conditions, particularly to cases involving superheated steam instead of saturated water as the leaking material. Neither is it possible to assess vibration effects in sustaining small leakages.

Table 1.3. Behavior of small leaks in mild-steel boiler tubes subjected to water at 2500 psi (17.2 MPa) and 350°C[a]

Test	Flaw diameter (mil)	Flaw diameter (μm)	Water leakage rate Initial (g/sec)	Water leakage rate Final (g/sec)	Comments
9	4.0	102	-	70.8	Spark eroded hole
11	4.0	102	0.4	2.0	Spark eroded hole
12	0.6	15	0.003	0	Tapered,[b] laser-drilled hole; leak sealed
13	0.5	13	0	0	Tapered,[b] laser-drilled hole; sealed rapidly in water tests
14	2.0	51	0.53	2.3	Tapered,[b] laser-drilled hole
15	2.0	51	0.37	3.6	Tapered,[b] laser-drilled hole

[a]Data taken from ref. 4.

[b]The minimum diameter is given for the tapered holes.

1.4.2 Flaw sizes for leakage in the superheated-steam region

Preliminary calculations indicated that the leakage rate of superheated steam through a small flaw in a steam generator tube would be sonic velocity limited. The leakage flow rate through a presumed pinhole size can be approximated by assuming that the steam expands isenthalpically to the helium side pressure and exits at the sonic velocity corresponding to steam properties in the expanded state.

The Mollier diagram for steam indicates that isenthalpic expansion from about 2980 psi (20.5 MPa) down to about 705 psi (4.86 MPa) avoids the two-phase region for temperatures above 770°F (376°C). Expansion would drop the steam temperatures to about 540°F (282°C) at 705 psi (4.86 MPa); at these conditions the sonic velocity is estimated to be about 1900 ft/sec (580 m/sec). Assuming a pinhole location near the exit from the steam generator, where the steam conditions of 2500 psi (17.2 MPa) and 950°F (510°C) exist, would yield a temperature of 820°F (438°C) on isenthalpic expansion to 705 psi (4.86 MPa), and somewhat higher sonic velocity of 2100 ft/sec (640 m/sec). Since these values are fairly close, there should be little difference in the nature of a small superheated steam leak anywhere in the superheated zone above 780°F (416°C).

An assumed steam exit velocity of 1900 ft/sec (580 m/sec) yields the flaw sizes for the given leakage rates shown in Table 1.4. Note that the flaw size corresponding to 0.01 g/sec in the primary circuit, which yields about 10 vpm total oxygen, is about 1.2 mil (30 μm).

Table 1.4. Tubing flaw sizes in the superheated regime

Leakage rate (g/sec)	Flaw size (mil)	Flaw size (μm)
0.001	0.39	10
0.01	1.2	30
0.1	3.9	99
1.0	12.0	310

Flaw sizes calculated by the indicated method should yield lower results than those calculated with more rigorous methods outlined in texts on compressible flow. However, calculations performed using the more rigorous method for the 0.01 g/sec case yielded approximately the same result as shown.

No experimental data have been found on the nature of small superheated steam leaks from high pressure corresponding to the data of Harper[4] for saturated water.

1.5 References for Section 1

1. General Atomic Standard Safety Analysis Report (GASSAR-6), GA-A-13200.

2. Delmarva Power and Light Co., Summit Power Station, Preliminary Safety Analysis Report, Amendment 4 (November 1973).

3. A. W. Barsell and M. B. Peroomian, Consequences of Water Ingress into the HTGR Primary Coolant, GA-A-13171 (April 1975).

4. C. Harper et al., Behavior of Small Leaks in Mild Steel Boiler Tubes when Subjected to Water at 2500 psi and 350°C, D.P. Report 789 (July 1972).

2. CONCLUSIONS AND SUMMARY

2.1 Major Conclusions

(1) The core posts initially possess a safety factor of about 10 under normal operating conditions. Since a minimum safety factor of 5 has been set for the end of reactor life in GASSAR-6, a maximum allowable core-post strength loss of 50% has been assumed for this study.

(2) The burnoff causing 50% strength loss is estimated to be between 260 and 620 mg/cm^2 for the nominal core post.

(3) The range of burnoffs and strength reductions at the end of reactor life for the nominal core posts, assuming nominal purification flow, is estimated to be:

Ingress rate $\left(\frac{g}{sec}\right)$	Total oxygen level (vpm)	Burnoff range $\left(\frac{mg}{cm^2}\right)$	Strength loss range (%)	Probability for 50% strength loss (%)
0.001	0.85	12-60	1-20	0
0.01	8.5	110-240	12-42	0
0.1	85.0	230-300	19-56	2
1.0	850.0	250-340	20-61	8

Continuous ingress rates of 0.025 g/sec and below, corresponding to total oxygen levels below 21 vpm at nominal purification flow, cause 40-year burnoffs which show a zero probability of 50% strength loss.

(4) A semiquantitative examination indicates that the maximum sustained core post temperature is approximately 90 °C above nominal. The burnoff causing 50% strength loss is estimated to be between 520 and 760 g/cm^2 for the hot core post material. The higher burnoffs for 50% strength loss are due to the tendency of corrosion to be more concentrated at the surface with increasing temperature.

(5) The following end-of-life burnoffs and probabilities for 50% strength loss are predicted for the core post material at the estimated maximum sustained temperature:

Ingress rate $\left(\frac{g}{sec}\right)$	Total oxygen level (vpm)	Burnoff range $\left(\frac{mg}{cm^2}\right)$	Strength loss range (%)	Probability for 50% strength loss (%)
0.001	0.85	75-350	6-36	0
0.004	3.4	300-980	30-76	50
0.01	8.5	670-1300	49-94	97
0.1	85.0	1300-1900	76-100	100

These results indicate the need for a more exact definition of the location and size of the sustained hot zone in the bottom support structure.

(6) Increasing purification flows were tested as a means for mitigating strength loss of the hot post material. Modest changes in purification rate (about a factor of 2) were found to have little effect. Significant beneficial effect begins to appear for purification rates above about five times the nominal values.

2.2 Summary

(1) The following steam corrosion rate expression for ATJ graphite, the present leading candidate for the core post material, was determined from published data on 1-in. spherical specimens of 5% burnoff,

$$R\left(\frac{mol}{cm^2\text{-}hr}\right) = \frac{85.1 \times 10^6 \exp\left(-\frac{50,000}{RT}\right) P_{H_2O}}{1 + 3560\,(P_{H_2} + P_{CO}) + 6950\,P_{H_2O}} ,$$

where partial pressures are expressed in atmospheres. A major uncertainty in use of the above rate equation is that the data on which the correlation is based exhibited a variation of observed corrosion

rate with test flowrate of an imperfectly understood character. Hence, extrapolation to core post flow conditions is uncertain. However, the rates predicted for ATJ by the above correlation generally fall within the band for other rate equations.

(2) Corrosion rate predictions from five published studies were compared for a number of representative conditions. Most frequently, the predictions lie within a factor of 10, but differences of a factor of 30 appear for some conditions. Some of the variation is due to the fact that some comparisons are necessarily made beyond the experimental conditions. A reasonable value for the range of intrinsic graphite corrosion rates is about 10. A range of a factor of 2 to 3 may be expected for different samples from one graphite type; this is believed to be caused primarily by a variation in microstructure at different locations.

(3) Analysis of the variation of impurity levels with axial location within one coolant channel indicates that the impurity concentrations are effectively constant from the top to the bottom of the core. This allows a simplified treatment of the primary system as a well-mixed pot, thereby ignoring spatial dependence of concentrations.

(4) One method of predicting primary system impurity compositions employed in this study was based on an analysis of the steam ingress experiments performed at the Dragon Reactor. The data were interpreted in terms of a simple, first-order reaction model and extrapolated to HTGR conditions. These results indicate that about 65% of the steam ingress to the primary system exists as oxidant for long term, steady ingress at the nominal purification rate.

(5) A second method of predicting impurity compositions for a given steam ingress rate is based on a mixed-pot model of the primary system termed TIMOX. TIMOX employs three published rate equations for predicting the core reactivity to steam corrosion, the three calculations being carried along in parallel. These yield

a range of estimates which reflect the uncertainty in predicting the core reactivity under the various conditions. The impurity compositions predicted from TIMOX compare reasonably well with predictions using the Dragon steam ingress experiment for total oxygen levels up to about 80 vpm; predictions diverge at higher impurity levels because of the simple model employed for interpreting the Dragon data.

(6) The corrosion rate expressions used in TIMOX are based on data acquired at 1 atm. For extrapolation to 49 atm,* the representative pressure of the HTGR primary system, the corrosion rate was assumed to vary with $1/\sqrt{P_T}$, when P_T is the system pressure. While this assumption is surprisingly good, considering the simplified view on which it is based, it may be a source of significant error for so large an extrapolation in pressure. Comparison with one data set shows that the inverse square root assumption would lead to a 60% overestimate of the corrosion rate at 49 atm. However, since this pressure correction was applied to both core and core support-post graphite, errors produced by the extrapolation tend to cancel each other. That is, an overestimate of the core corrosion rate leads to a less oxidative atmosphere which tends to compensate for the corresponding overestimate for the core support-post corrosion rate.

(7) A necessary prerequisite for using TIMOX was a detailed examination of the core temperature distribution. The problem addressed was how to determine the appropriate average temperature of a relatively large region for a strongly temperature-dependent process like steam corrosion. The simple space-average temperature would tend to yield too low a rate, since the higher temperature zones are not given enough weight. The result of this examination shows that simple space averages are sufficiently accurate for regions as small as an OXIDE-3 region, but significant errors could result from use of the space average for larger regions, such as TIMOX regions, which are composed of about 100 smaller OXIDE-3 zones.

---

*4.97 MPa.

(8) An empirical fit of strength loss data for 4-mm-thick specimens was found in the form,

$$FSL = P(T) \cdot \frac{BO}{\rho_{bo} \cdot W} ,$$

where FSL is the fractional strength loss, BO is the burnoff in g/cm^2, ρ_{bo} is about 90% of the graphite density, and W is the specimen width. The multiplier, P(T), depends inversely on temperature with values ranging from 1.8 at 1140°C to 4.4 at 950°C. Extrapolating to core post conditions involves considerable uncertainty. The estimate for the parameter P(T) at the nominal core post temperature ranges from 6.0 to 14.0, and from 4.8 to 7.1 at the estimated maximum core post temperature.

(9) Strength loss predictions based on the above correlation compare reasonably well with data obtained on 1/2-in.-diam H-327 graphite specimens at 900°C and up to 15% burnoff, at which point 80% strength loss had occurred. The correlation was also tested against published data on 1/2-in. specimens of H-328 and TS-688 graphite at 1000°C. Again the comparison is reasonably good considering the scatter in the data. One graphite, S-9567, was found to lose strength with burnoff more slowly than predicted by the correlation.

(10) Comparison of results with core post loads under normal operating conditions generally agrees with GASSAR-6 results which state that an initial safety factor of about 10 exists. However, the reasoning which leads to this result differs somewhat. In each case (GASSAR-6 and this study) an additional load factor of about 2 is assumed somewhat arbitrarily for some core posts to account for nonideal load distribution due to varying post lengths.

(11) The degree of sustained temperature excess over and above the nominal post temperature is shown to be a critical parameter in the study. Judgments outlined in Sect. 6.3.2, which involve stated operating characteristics of coolant flow-distribution valves, hot-streaking results reported for the steam generator

inlet, and intraregional power tilts indicated by OXIDE-3 results, lead to the conclusion that 90°C is a reasonable estimate for the sustained temperature excess in the core post region.

(12) Since the reference reactor chosen for this study has somewhat different temperature levels from that reported in GASSAR-6, which appeared late in this study, the effect of modest changes in primary system temperature levels was investigated. These comparisons show that in some circumstances a general primary system temperature rise may benefit the core posts because the oxidant gettering ability of the core is enhanced; in addition, the corrosion tends to be more closely confined to the post surface zone, thereby causing less strength reduction for a given amount of burnoff. A more confident prediction of the effect of primary system temperature on core post strength loss would require more accurate graphite reactivities for both post and core material.

(13) A useful method has been developed, outlined in Appendix A, for predicting the probability that an estimated range of burnoffs would cause 50% strength loss. This problem needs formal treatment because the burnoffs that may cause 50% strength loss exist as estimates with a given range. Hence, we are comparing a predicted burnoff range which could overlap a target burnoff range for 50% strength loss in varying degrees. The formal procedure provides an estimate for the probability of 50% strength reduction based on the assumption of flat probability density distribution within each estimated burnoff range.

3. RECOMMENDATIONS

(1) It is essential to more accurately define the location and extent of the persistent hot zones in the bottom core support structure, including the core posts. These hot zones are caused by a combination of intraregional power tilting, nonideal coolant flow distribution at the core inlet plenum, and hot streaking at the core exit.

(2) Additional data are needed to develop an understanding of the problems that exist in the area of graphite strength loss due to corrosion by low levels of oxidants. Experiments are recommended on the selected reference structural graphites to determine the change in pertinent mechanical properties caused by corrosion. The effects of specimen size, temperature of burnoff, stress, and oxidant concentration need to be investigated. Preferably, data should be acquired at 50 atm,* or alternatively, at a number of lower pressures to allow extrapolation to 50 atm. Although a pragmatic and direct type of experiment is recommended, it is important to accompany these tests with sufficient before-and-after graphite characterization work to gain some understanding of the strength loss process. The burnoff experiments should be performed in a manner allowing verification or correction of the corrosion rate predictive equations for these structural graphites.

(3) A special effort should be made to obtain additional corrosion rate data for ATJ, the reference core post graphite, in view of its nontypical behavior in laboratory tests (i.e., the unexpected dependency of the observed rate on He flow, and the unusually large amount of CO_2 observed in the effluent).

(4) This study should be repeated, with special attention given to: (a) the projected revised core post diameters; (b) the revised estimate for maximum allowable core post strength loss dictated by upset conditions; (c) improved corrosion rate data for reference core graphite; (d) improved knowledge of the maximum sustained post temperature; and (e) improved strength loss data, if available.

---

*5.1 MPa.

(5) This study deals exclusively with projected consequences of a given range of steam ingress rates; thus, the total impurity level was treated as a parameter. A next logical step would be to devote some effort to predicting what these total impurity levels could be on a realistic basis. Consideration should be given to a study program directed to devising measures for reducing steam generator leakage based on understanding of the root causes.

(6) Additional basic work on the nature of graphite corrosion is recommended. Despite much existing work in this area, and the recognized difficulty in extrapolating basic data to engineering systems because of the complexity and variability of graphite, further basic work is recommended to fill the following specific safety-related needs.

   (a) Present computer programs used to predict the composition of impurities in the primary system employ an unreasonably simple model for the distribution of oxidant in the core graphite. Hence, the predicted oxidant level for a given inleakage rate (a fundamental quantity for assessing effect on the graphite structure) is uncertain, thereby contributing to the error band on predicted burnoffs.

   (b) Little information is available on the distribution of burnoffs within a graphite member under a variety of corrosion conditions. This type of data is fundamental to determining the degree of strength loss for a given amount of corrosion.

4.1.1 Properties of ATJ graphite

"Grade ATJ is an extremely fine-grain, essentially flaw free, high strength, premium quality graphite. It can be machined to very close limits and sharp detail with fine surface finish."[5] ATJ is not impregnated. Some properties of ATJ are listed in Table 4.1.[5]

The pore size distribution, as determined by mercury porosimeter measurements, is shown in Fig. 4.1. ATJ shows a characteristic bimodal

4. STEAM-GRAPHITE REACTION RATES

The first half of this section is devoted to a description of ATJ graphite (which is the presently selected core post material) and a derivation of a reaction rate expression for ATJ corrosion by low levels of steam from published data. The second half of the section summarizes three major graphite kinetics studies which have culminated in complete reaction rate expressions, and could therefore be incorporated in a systems study of the HTGR primary circuit. These three studies are thus used as stand-ins for the reactivity of reference core graphite for which a comparable rate expression is not now available. In each case, the rate equation is presented in its original form, and is then converted to a consistent set of units based on exposed graphite surface area for expendient comparison of predicted reaction rates.

4.1 Corrosion of ATJ Graphite by Low Levels of Steam in Helium

The oxidation of ATJ graphite by low concentrations of water vapor and carbon dioxide in helium has been studied by Blakely and Overholser.[1] A prior paper[2] by these authors on Speer Moderator-2 graphite contains the description of the experimental method as well as some interesting comparisons of ATJ vs Speer Moderator-2 corrosion. Additional data on ATJ corrosion appear in refs. 3 and 4; however, since pure steam at about 1 atm was used for these studies they will not be included in this description, though they may contain some potentially useful data – particularly regarding the change in BET area with burnoff for ATJ.

4.1.1 Properties of ATJ graphite

> "Grade ATJ is an extremely fine-grain, essentially flaw free, high strength, premium quality graphite. It can be machined to very close limits and sharp detail with fine surface finish."[5]

ATJ is not impregnated. Some properties of ATJ are listed in Table 4.1.[5]

The pore size distribution, as determined by mercury porosimeter measurements, is shown in Fig. 4.1. ATJ shows a characteristic bimodal

Table 4.1. Room temperature ATJ properties[a]

Forming method	Molded
Bulk density, g/cm^3	1.73
Maximum grain size, μm	150
Flexure strength, with grain, psi	4010
across grain, psi	3580
Tensile strength, with grain, psi	1790
across grain, psi	1420
Compressive strength, with grain, psi	8270
across grain, psi	8540
Young's modulus, with grain, psi	1.45×10^6
across grain, psi	1.15×10^6
Coefficient of thermal expansion, with grain, $°C^{-1}$	2.19×10^{-6}
across grain, $°C^{-1}$	3.42×10^{-6}
Thermal conductivity, with grain, cal/cm-sec-°C	0.281
across grain, cal/cm-sec-°C	0.241
Permeability, with grain, darcys	0.015
across grain, darcys	0.012
Ash content, percent	0.16 ± 0.038
Impurity levels, percent of graphite	
Fe	0.042
V	~ 0.004
S	~ 0.04
Ca	~ 0.01
Ti	~ 0.004
Al	~ 0.01
B	~ 0.00011
Li	< 0.0010
Cd	< 0.0010

[a]From the Industrial Graphite Engineering Handbook, Carbon Products Division, Union Carbide Corp.

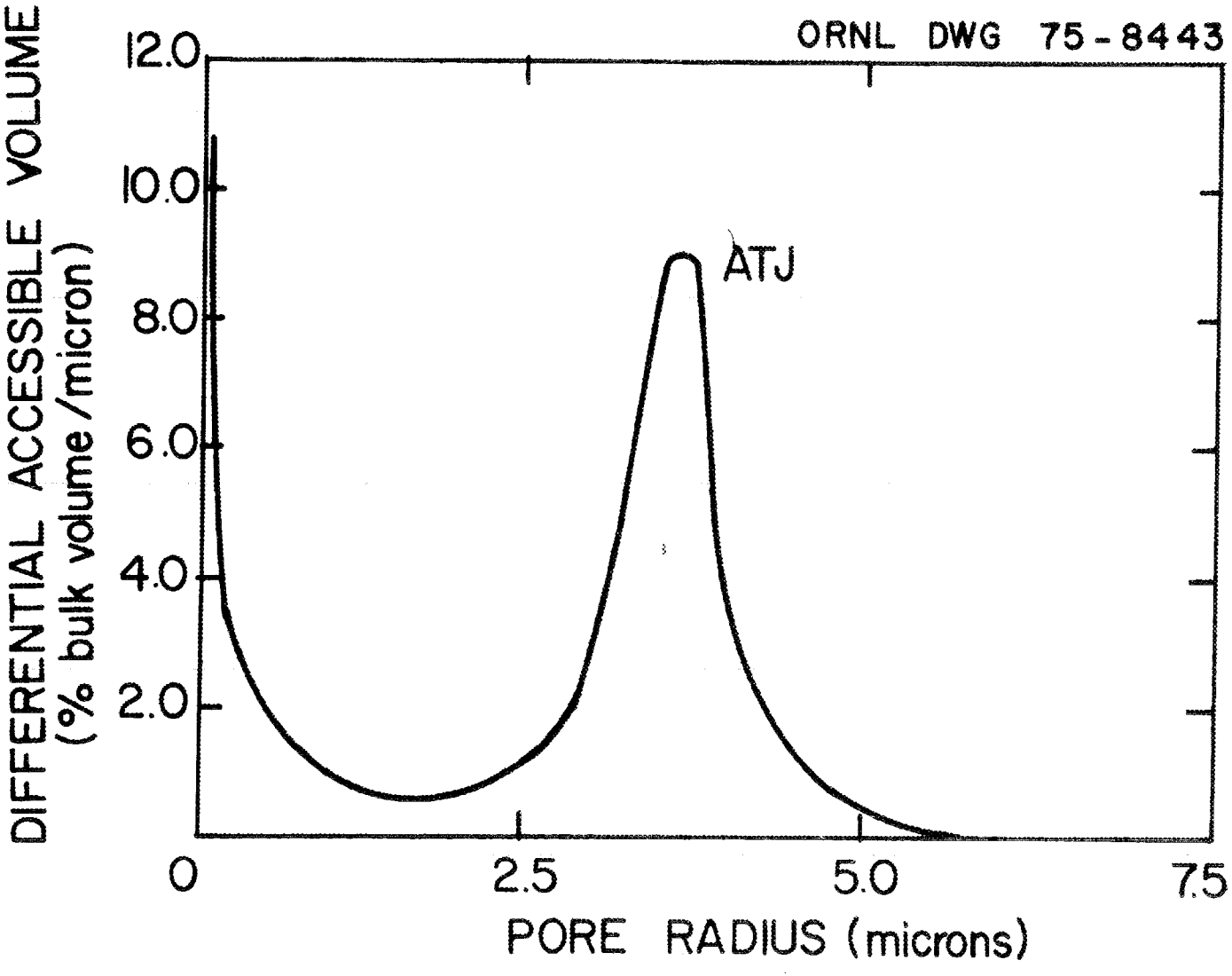

Fig. 4.1. Pore size distribution of ATJ graphite by mercury porosimetry.

pore size distribution with the larger pores in the 3 to 4 μm range, and micropores centering about ~ 0.1 μm.

Some selected ATJ thermomechanical properties measured by GAC[6] are listed in Table 4.2. Measurements were performed on specimens drawn from 8-in.-diam molded round bar stock, both parallel and perpendicular to the axis of the cylinder, and 8 x 18 x 50 in. molded rectangular bar stock. The designations 8, 18, and 50-in. direction shown in Table 4.2 denote measurements on samples of stock in the three coordinate directions of rectangular bar stock.

4.1.2 General features of ATJ corrosion by low concentrations of H_2O in helium – work of Blakely and Overholser[1]

In these experiments,[1] a single 1-in.-diam sphere of machined ATJ graphite, degassed under vacuum at 1025°C for 4 days, was suspended from the arm of a recording balance in a 2-in.-diam quartz tube. The flowing gas stream entered near the bottom of the quartz tube, passed upward, and departed through an opening near the top of the tube. Helium, which was used as a carrier at 1 atm, was purified by passage through a refrigerated charcoal trap. The desired concentrations of carbon dioxide were obtained by passing the helium through a bed of calcium carbonate held at various carefully controlled temperatures. The helium-water vapor mixtures were prepared by dividing the helium stream, saturating prescribed fractions of the gas over saturated calcium chloride (0°C), and combining the two streams. Additions of hydrogen or carbon monoxide to the helium-water vapor or helium-carbon dioxide mixtures were made by metering helium containing ~ 1.5% of hydrogen or carbon monoxide. The influent and effluent gas streams were analyzed by a gas chromatograph for all consitituents of interest except water vapor, which was determined by a CEC Moisture Monitor.

These experiments show a puzzling feature which render it difficult to make quantitative use of the results. The reaction rate was observed to markedly increase with increasing helium flowrate, as indicated in Fig. 4.2. A cross plot of the data shows an approximately linear increase

Table 4.2. ATJ graphite properties from GAC measurements[a]

Coefficient of thermal expansion, Ave. 22-1000°C, $°C^{-1} \times 10^6$	
50-in. direction	3.57 ± 0.19
18-in. direction	3.63 ± 0.15
8-in. direction	4.88 ± 0.05
Thermal conductivity at 800°C, cal/cm-sec-°C	
∥-direction	0.123 ± 0.004
⊥-direction	0.162 ± 0.009
Density at 25°C, gm/cm^3	
Molded round stock	1.784 ± 0.024
Molded rectangular bar stock	1.765 ± 0.114
Ultimate compressive strength at 25°C, psi	
∥-direction	10,420 ± 220
⊥-direction	10,560 ± 600
8-in. direction	10,060 ± 230
18-in. direction	9,420 ± 1,170
50-in. direction	10,820 ± 550
Ultimate tensile strength at 25°C, psi	
∥-direction	1,818 ± 573
⊥-direction	2,963 ± 217
8-in. direction	2,383 ± 247
18-in. direction	2,385 ± 443
50-in. direction	3,318 ± 358

[a]From C. Meyers and K. Koyama, Evaluation of Candidate Graphites for PSC Core Support Applications, GAMD-8371 (February 1968).

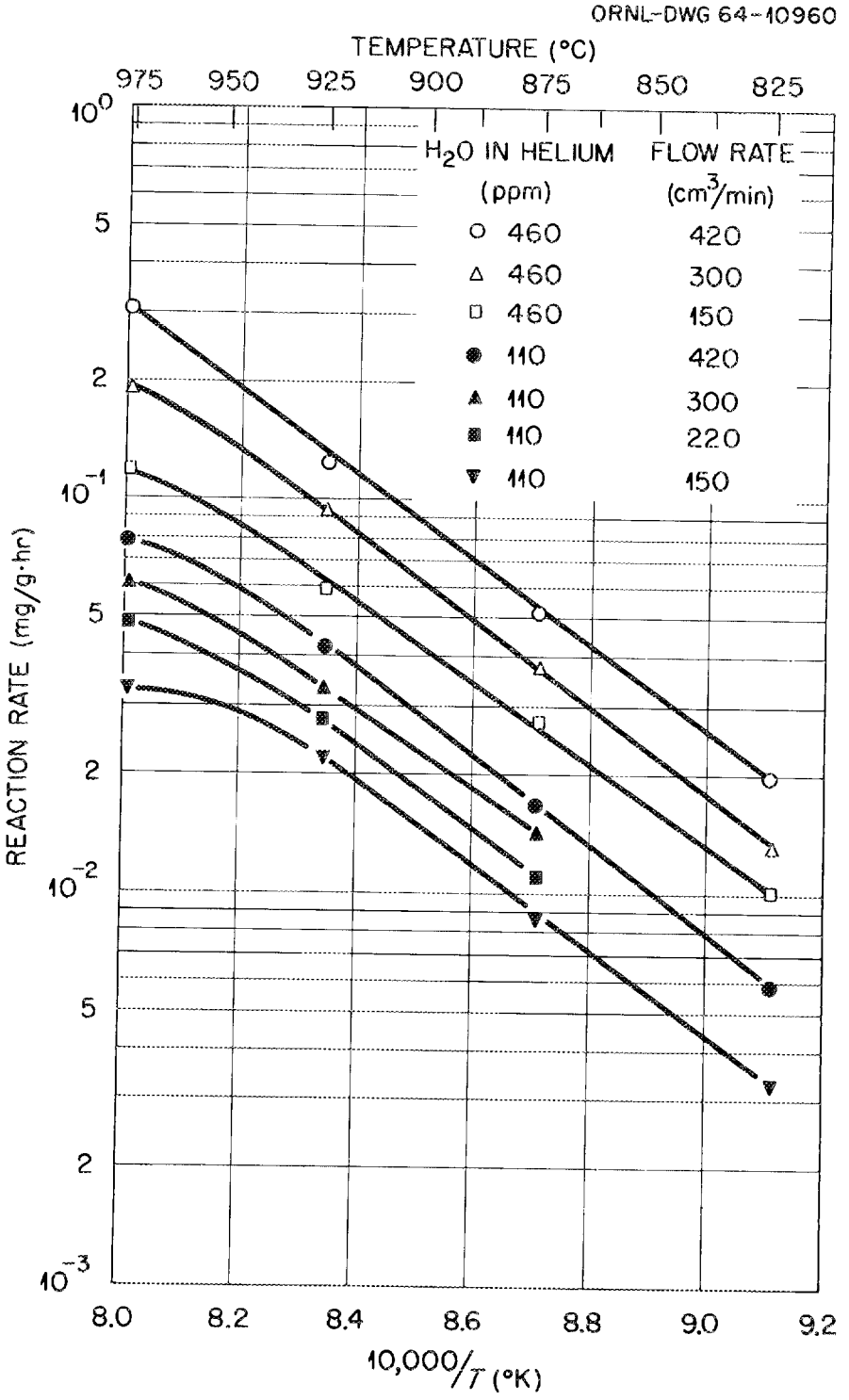

Fig. 4.2. Effect of temperature and flow rate on the H_2O-graphite reaction at inlet H_2O concentrations of 110 and 460 vpm (~ 5 wt % burnoff) for ATJ graphite.[1]

with flowrate, which implies a mass-transfer control mechanism through the surface film. However, the variation with temperature is such that the activation energy equals ~ 50 kcal/mol, which is not consistent with surface film control. Surface film control should show far less temperature dependence, whereas 50 kcal/mol is typical of in-pore diffusion control; however, it should not be so flow sensitive.

Surface drag effects due to the upward flow of helium, which could alter the specimen mass determination if sufficiently large, appear to be ruled out because this phenomenon was seen only slightly with Speer Moderator-2 graphite employing the same apparatus. Blakely and Overholser do not offer an explanation for this effect, but the most likely cause is some not well-understood manifestation of the diffusion process applicable to ATJ graphite. Extrapolating these data to core post conditions, where the velocities are much higher than in these experiments, introduces a large uncertainty, principally because the reason for this behavior is not known.

The variation of reaction rate with burnoff at 975 °C is shown in Fig. 4.3. The reaction rate increases rapidly at the outset of corrosion and up to approximately 0.05% burnoff, reflecting the corrosion of the more reactive portions of the ATJ specimen. The rate of increase following this initial rapid rate and up to about 1% burnoff appears to be fairly typical behavior. For example, the burnoff factor used in the OXIDE-3 code[7] increases about 70% between 0.1 and 1% burnoff, compared with a rise of about 115% for ATJ in the same range.

The rate of increase in the reaction rate beyond 1% burnoff is of vital interest. No specific data are given by Blakely and Overholser either in ref. 1 or the GCRP progress reports covering the work during this period; however, it is implied that at least for 875 °C the reaction rate continued to increase with burnoff up to 8% burnoff, but more slowly than the linear rise shown between 0.1 and 1%. It should be emphasized that this is surmised from the text, but is not stated specifically. However, this behavior appears to be at least qualitatively consistent with other graphites. For example, the OXIDE-3 burnoff factor shows a

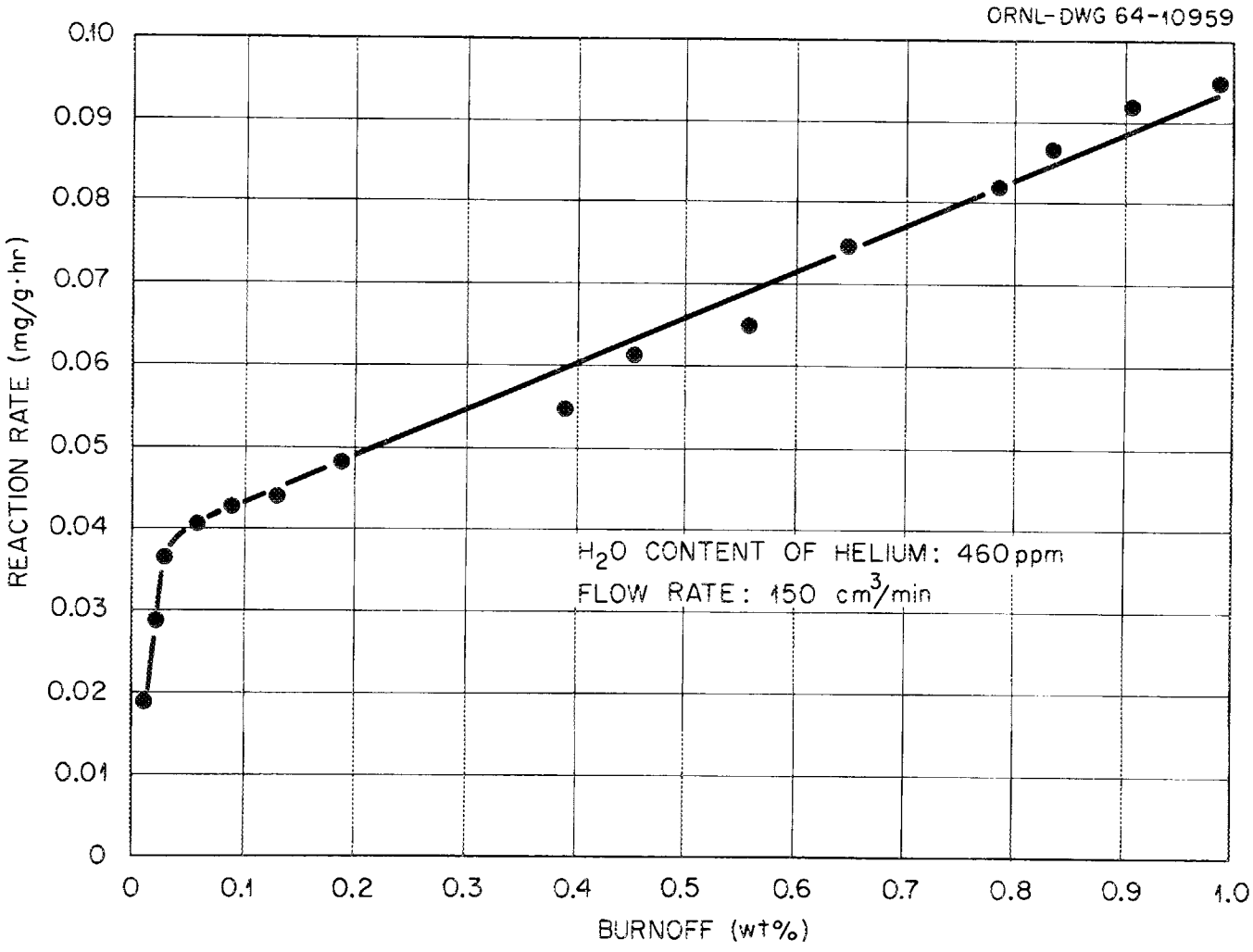

Fig. 4.3. Effect of burnoff on the H_2O-AEJ graphite reaction at 975°C (flow rate of 150 cm^3/min STP, inlet concentration of 460 vpm of H_2O).[1]

gradual rise of about 65% between 1 and 10% burnoff. No data are given by Blakely and Overholser on the distribution of burnoff within the 1-in.-diam specimen.

Another unique feature of the data is the large amount of CO_2 produced (see Table 4.3). Identical runs using Speer Moderator-2 graphite showed little or no CO_2 in the effluent gas. In-pile steam oxidation of graphite usually does form CO_2 via the photon-catalyzed shift reaction

$$H_2O + CO \xrightarrow{\gamma} CO_2 + H_2 \quad , \tag{1}$$

but CO_2 is normally not present to any significant extent in thermally activated corrosion studies. It is hypothesized by Blakely and Overholser that the large amounts of CO_2 observed in the ATJ steam corrosion experiments also result from the shift reaction, catalyzed by impurities in ATJ. (Production of some CO_2 is thermodynamically favored with excess steam at temperatures below about 1000°K.)

Figure 4.4 illustrates the dependence of reaction rate on the concentration of H_2O in the inlet gas, and also the relative rates of ATJ corrosion with H_2O and CO_2 at 875°C under identical conditions. The apparent reaction order of 0.67 for H_2O corrosion is consistent with a rate expression in the commonly accepted Hinshelwood form,

$$\text{Rate} = \frac{k_1 P_{H_2O}}{1 + k_2 (P_{H_2} + P_{CO}) + k_3 P_{H_2O}} \quad , \tag{2}$$

at least over modest ranges of H_2O concentration. Equation (2) presumes a retardation effect for H_2 and CO of about equal magnitude, as observed by Wicke et al.[8] for type "G-5" graphite. Blakely and Overholser show that CO does indeed have an intrinsic retardation effect in the steam oxidation of ATJ, other than the secondary effect of depleting H_2O via the shift reaction, but they do not specifically determine a relative value for H_2 and CO retardation.

Figure 4.4 also illustrates that for similar inlet concentrations, the thermally activated H_2O oxidation rate of ATJ is only about twice that

Table 4.3. Inlet and effluent gas compositions and reaction rates for H_2O corrosion of ATJ at 875°C.[1]
Flowrate = ~ 300 cc STP/min, burnoff = ~ 5%

Inlet concentrations (vpm)		Observed effluent concentrations (vpm)			Modified[a] effluent concentrations (vpm)			Reaction rate (μg/gm·hr)	
(1)	(2)	(3)	(4)	(5)	(6)	(7)	(8)	(9)	(10)
H_2O	H_2	CO_2	CO	H_2	H_2O	CO	H_2	Observed	Calculated Eq. (3)[b]
30	0	7	6	21	16.5	13	14	8	7.84
60	0	12	9	35	38	21	23	13	14.1
110	0	25	13	60	73.5	38	35	22	21.2
250	0	50	15	100	193	65	50	37	32.9
110	0	21	15	65	70.5	36	44	22	20.8
110	120	14	14	170	77.5	28	156	16.5	17.3
110	280	11	14	325	85.5	25	314	14.5	14.3
110	530	6	11	570	84.5	17	564	10.5	10.9
110	1050	3	8	1080	89	11	1077	7.5	7.38

[a]See Sect. 4.1.

[b]See p. 33.

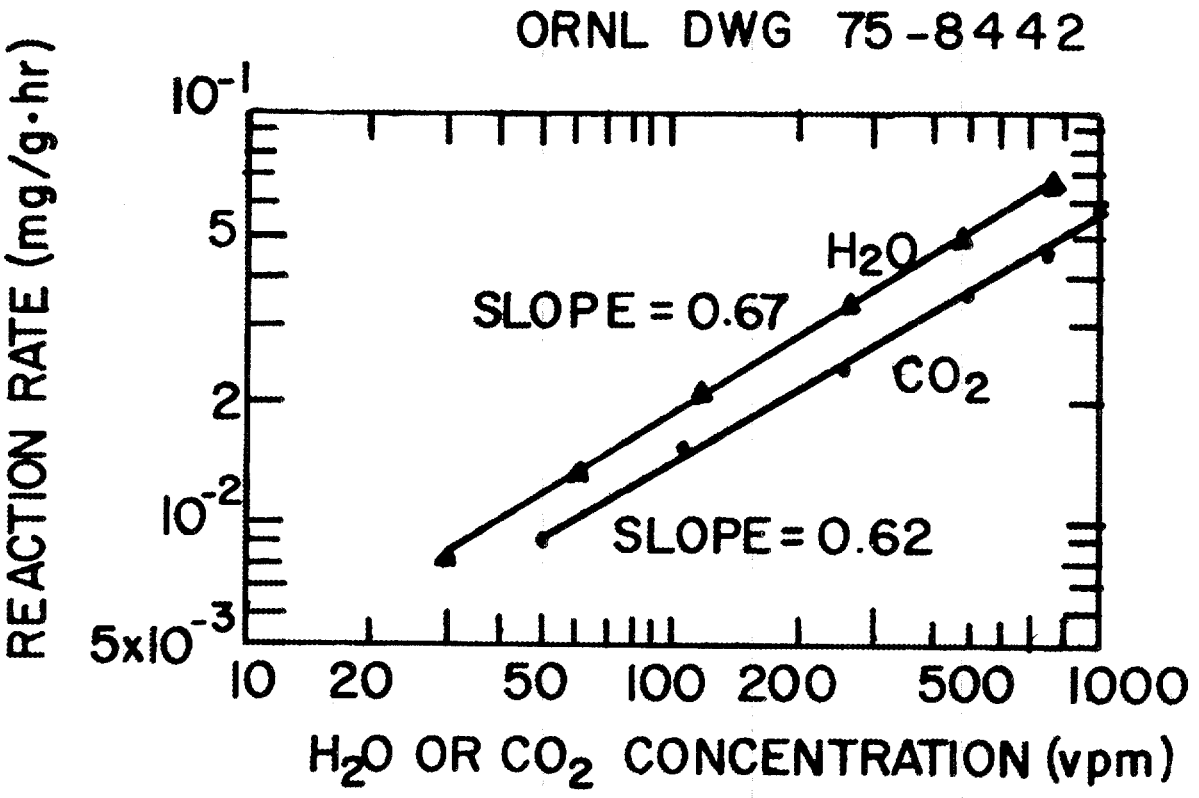

Fig. 4.4. Apparent order of the H_2O and CO_2 reactions with ATJ graphite at 875 °C (flow rate of 300 cm^3/min STP, ~ 5 wt % burnoff, inlet concentrations given).[1]

of CO_2. Identical runs using Speer Moderator-2 graphite[2] indicated about a factor of 8 higher corrosion rate with H_2O relative to CO_2. Again, it is hypothesized that the difference may be attributed to the different impurity contents of the two materials.

4.1.3 Corrosion rate expression for ATJ from the data of Blakely and Overholser[1]

In this section, an empirical corrosion rate expression for ATJ will be developed in the form given in Eq. (2), based on tabular data presented by Blakely and Overholser.[1] Table 4.3 lists the observed inlet and effluent compositions in columns 1 through 5 for a series of runs at 875 °C. The observed reaction rates, given in column 9, are the average of that measured directly by the beam balance and the computed value using the total carbon in the effluent stream. These two rates were always within 10% of each other; hence, the reaction rate is known with some confidence.

Though not explicitly stated in ref. 1, the presented data apparently pertain to a specimen of about 5% burnoff. The observed rates at this degree of burnoff are surmised to be about a factor of 3 higher than the rates observed at 0.1% burnoff, assuming that ATJ behaves as a typical graphite above 1% burnoff.

In Table 4.3, a comparison of columns 3 to 5 with columns 1 and 2, taken directly from ref. 1, shows less total hydrogen and oxygen in the effluent than in the inlet flow. Although not stated in the reference, this is evidently due to H_2O in the effluent which was not measured. The concentrations of H_2O shown in column 6 are computed from the average of a hydrogen and oxygen mass balance, and bring the inlet and outlet hydrogen and oxygen flows in agreement to within an average of about 10%.

An additional problem in the data analysis is the treatment of the CO_2 observed in the effluent within the framework of the proposed form of rate expression, Eq. (2), in which CO_2 concentration does not appear. We will handle this as follows: Since the appearance of CO_2 is evidently not due to corrosion, but rather to a reaction between H_2O and CO, and since the products of this reaction, CO_2 and H_2, each have approximately

the same effect on ATJ as the reactants, we will modify the observed effluent concentrations to what they would have been had this shift reaction not occurred.

Thus, the modified effluent concentrations shown in columns 6-8 of Table 4.3 were obtained – by reversing the shift reaction by which CO_2 is produced and by adding H_2O to the effluent to balance the hydrogen and oxygen.

A least squares fit of the data in Table 4.3 yields the following corrosion rate expression:

$$R\left(\frac{\mu m}{g\text{-}hr}\right) = \frac{0.408\ \mu_{H_2O}}{1 + 0.00356\ (\mu_{H_2} + \mu_{CO}) + 0.00695\ \mu_{H_2O}} \quad . \tag{3}$$

The constants in Eq. (3) are based on the assumption that the graphite specimen in the tests experienced an effective impurity composition given by the average of the measured inlet composition and the effluent compositions modified in the manner indicated above. The comparison between the rates observed and those calculated by using Eq. (3) are listed in columns 9 and 10 of Table 4.3. The average deviation between observed and calculated values is ± 10.3%.

A temperature dependence is introduced into Eq. (3) by noting that the reaction was observed to vary linearly on an Arrhenius plot with an effective activation energy of 50 kcal/mol (see Fig. 4.2). Applying this variability solely to the coefficient in the numerator, and noting that the data presented in Table 4.3 refer to 875°C, yields,

$$R\left(\frac{g}{g\text{-}hr}\right) = \frac{1.34 \times 10^9 \exp\left(-\frac{50{,}000}{RT}\right) P_{H_2O}}{1 + 3560\ (P_{H_2} + P_{CO}) + 6950\ P_{H_2O}} \quad , \tag{4}$$

with compositions now expressed in atmospheres partial pressures, and the rate given in terms of grams reacted per hour per gram of specimen.

4.1.4. Conversion of ATJ corrosion rate equation [Eq. (4)] to surface units (mol/cm^2-hr)

In most graphite corrosion studies and literature publications on the subject of graphite corrosion including the work of Blakely and Overholser,[1] but with the notable exception of recent Dragon Project work, the reaction rate is expressed in units of [g/g-hr], or some equivalent thereof. This is inappropriate for large graphite members at high temperature where the active corrosion zone of perhaps 1 to 3-mm depth (see Sect. 4.2.2) represents a small fraction of the total mass. In these cases, the reaction rate is proportional to the exposed surface area rather than the total mass of graphite; hence, an expression of the reaction rate in terms of (g/cm^2.hr), or some equivalent, is more appropriate. It is therefore necessary to obtain a relationship between these two means for expressing the reaction rate in order to convert to the surface based units.

It will be shown in Sect. 4.2.2 that the depth of the active corrosion zone is approximately 2 mm at 874°C, the temperature representative of the data in Table 4.3. Since the tests were made with 1-in. diam spheres, we will term the reported reaction rates, R_{app} (g/g-hr), where the subscript refers to "apparent"; this signifies that the active zone of the reaction is much less than the total specimen mass, m_T.

The rate in terms of the actual amount of mass involved in the reaction, m, is related to R_{app} by:

$$R_{act}\left(\frac{g}{g\text{-}hr}\right) = R_{app}\left(\frac{g}{g\text{-}hr}\right)\frac{m_T}{m} \quad . \tag{5}$$

The ratio m_T/m is given by $R/3\cdot\Delta h$, for a large spherical specimen in which $R \gg \Delta h$, where Δh is the active reaction depth. Hence, Eq. (5) may be written

$$R_{act}\left(\frac{g}{g\text{-}hr}\right) = R_{app}\left(\frac{g}{g\text{-}hr}\right)\frac{R}{3\Delta h} \quad . \tag{6}$$

The rate based on exposed surface area, R_s, is related to R_{act} by

$$R_s \left(\frac{\text{mol}}{\text{cm}^2\text{-hr}} \right) = R_{act} \left(\frac{\text{g}}{\text{g-hr}} \right) \frac{\Delta h \rho}{M_w} , \tag{7}$$

where M_w is the molecular weight. Combining Eqs. (6) and (7) yields the desired conversion,

$$R_s \left(\frac{\text{mol}}{\text{cm}^2\text{-hr}} \right) = R_{app} \left(\frac{\text{g}}{\text{g-hr}} \right) \frac{R \rho}{3 M_w} . \tag{8}$$

A similar discussion for a cylindrical specimen with radius R yields

$$R_s \left(\frac{\text{mol}}{\text{cm}^2\text{-hr}} \right) = R_{app} \left(\frac{\text{g}}{\text{g-hr}} \right) \frac{R \rho}{2 M_w} . \tag{9}$$

Applying the conversion indicated by Eq. (8) to Eq. (4) using a graphite density of 1.8 g/cm^3 yields

$$R_s \left(\frac{\text{mol}}{\text{cm}^2\text{-hr}} \right) = \frac{85.1 \times 10^6 \exp\left(- \frac{50,000}{RT} \right) P_{H_2O}}{1 + 3560 \left(P_{H_2} + P_{CO} \right) + 6950 P_{H_2O}} \tag{10}$$

for the corrosion rate of ATJ based on exposed surface area.

Equation (10) is compared with other published kinetics equations in Sect. 4.2.5. In general, the rates predicted by Eq. (10) for ATJ are within the band of predictions of the other kinetics equation which refer to a number of other types of graphite.

4.2 Summary and Comparison of Steam-Graphite Corrosion Studies

4.2.1 Work of Wicke et al.[8] at the University of Münster

Perhaps the most extensive study of graphite corrosion at high temperatures by low concentrations of oxidant was conducted at the Institute for Physical Chemistry of the University of Münster under contract by the Dragon Project. The work extended over a 4 year period beginning in 1961, and is summarized in a final report.[8] Much additional information is

given in a major review article by Everett, Kinsey, and Romberg[9] which incorporated much of the work of the Münster group. The major objectives and findings of this study are given below.

Graphite characterization and classification results from the Münster study. The first objective of the study was the classification of a variety of graphites from different origins and preparation processes with respect to their susceptibility to corrosion. Two standarized tests employing pure CO_2 as the oxidant were used to screen and grade graphites according to corrosion rate.

All data and descriptive material for this phase of the work appear in internal progress reports, and hence are unavailable. The following conclusions, appearing in the summary report,[8] are based on a total of about 100 reactivity tests involving 11 graphite types.

(1) All nonimpregnated graphites behaved in a qualitatively similar fashion. Corrosion susceptibility was found to increase continuously with burnoff from 0 to 15% burnoff. Also, the degree of reactivity increase was quite similar for the nonimpregnated graphites under similar oxidizing conditions. In all cases the reactivity increase with burnoff was greatest when the oxidation rate was slowest.

(2) Intrinsic reactivities of all nonimpregnated graphites varied through a range of about one order of magnitude at the selected reference condition of 1100°C and 10% burnoff. Differences in impurity level are given as the major cause of reactivity differences at this reference condition.

(3) The range in observed reactivity of samples drawn from different locations on the same bar were about a factor of 2 to 3. These were attributed to microstructural differences.

(4) Impregnated graphites behaved quite differently from the nonimpregnated graphites.* The initial reactivity was

*There is some question as to whether these comments pertain only to furfural alcohol-impregnated graphite but exclude pitch impregnations.

high, and dropped to a minimum at 5% burnoff, reflecting the burnoff of the impregnant which is the most reactive component.

(5) Impregnated specimens were also more reactive than non-impregnated specimens at higher burnoffs for not well-understood reasons. It is speculated that impregnation adds impurities which increase graphite reactivity.

(6) Impregnation caused nonuniform reactivity throughout the bars.

Detailed investigation of H_2O and CO_2 induced graphite corrosion by the Münster group. The least reactive graphite from phase 1 of the Münster study was selected for detailed examination of its reaction kinetics with H_2O and CO_2. The graphite chosen was designated as Péchiney G5 with properties given in Table 4.4. The graphite was preburned to 20% burnoff, at which point its reactivity remained fairly constant over a wide range of burnoffs. The graphite was crushed to a size range of 0.4 to 1.0 mm to assure uniform corrosion throughout each particle.

Table 4.4. Properties of Péchiney G5 graphite used in the Münster study

Density, g/cm^3	1.82
Total porosity, %	19.1
Characteristic pore radius, μm	1.5
Initial BET surface area, m^2/g	~ 0.5
Permeability, cm^2/sec	$\sim 10^{-2}$
Impurities, ppm	
Total ash	50-750
Fe	2-20
Al	1-10
Ca	15-200
Ni	< 3
Si	50-150
Ti	4-75
V	4-60

The kinetics experiments were conducted at 1-atm total pressure and through a temperature range of 940° to 1030°C. The H_2O level ranged from 350 to 1040 vpm, with helium as the carrier gas. CO and H_2 levels were varied from 130 to 1050 vpm.

The major result of this portion of the study is embodied in the derived kinetics equation, given in final form in ref. 9, as

$$R\left(\frac{\text{mol}}{\text{g-sec}}\right) = \frac{k_1 C_{H_2O}}{1 + k_2 C_{H_2} + k_3 C_{CO}} , \qquad (11)$$

where

C = concentration, mol/cm^3,

$k_1 = 5.0 \times 10^{12} \exp\left(-\frac{68,000}{RT}\right)$, $\text{cm}^3/\text{g-sec}$,

$k_2 = 3.7 \times 10^{5} \exp\left(\frac{14,500}{RT}\right)$, cm^3/mol,

$k_3 = 3.0 \times 10^{5} \exp\left(\frac{14,500}{RT}\right)$, cm^3/mol.

Equation (11) shows the following features compared with the ATJ corrosion discussed in Sect. 4.1 and other graphite corrosion work to be described below.

(1) The dependence of reactivity with temperature was the highest of all the studies which were reviewed. Activation energies in the range of 30 to 50 kcal/mol are more typical than the value of 68 derived in this study. The probable reason for this behavior was that this was the only work employing crushed particles. The gaseous diffusion process internal to the graphite is known to decrease observed temperature dependence of chemical reactions. Thus, the value of 68 kcal/mol may be close to the inherent graphite activation energy, while the commonly observed range of from 30 to 50 kcal/mol represents the effect of in-pore diffusion.

(2) A second significant observation is that the reaction products, H_2 and CO, were found to inhibit the reaction

to approximately the same degree, as reflected by the approximately equal values of the constants k_2 and k_3. There is by no means agreement on this feature; but these results were obtained from an extensive series of tests in which the H_2 and CO levels were independently varied in the feed gas, and hence are rather convincing.

(3) Another point of departure between Eq. (11) and other studies is the absence of a H_2O-dependent inhibition factor in the denominator. As a result, Eq. (11) invariably yields high predicted reactivities at high assumed H_2O concentrations.

(4) In contrast with the ATJ corrosion studies, but consistent with all other thermally activated graphite corrosion work, only small amounts of CO_2 were observed in the effluent gas.

4.2.2 Conversion of the Wicke rate equation to surface units

Equation (11) was based on data using small particles of graphite in the range of 0.4 to 1 mm, so chosen to assure uniform corrosion throughout the particle. Therefore, conversion of the rate, given in units of (g/g-sec), to a per unit area of exposed surface basis requires knowledge of the mass of graphite contained in the actively reacting corrosion zone.

Variation of corrosion depth with temperature – work of Helsby and Everett.[10] Figure 4.5 illustrates the variation in degree of corrosion observed with depth from the original graphite surface for two burnoffs and three temperatures.[10] The graphite type was identified by the designation "No. 1," and described as a triply pitch-impregnated, Gilsonite-based, isotropic graphite. The specimen thickness was initially 4 mm, and the corrosive atmosphere was set at 250-μatm H_2O and 3000-μatm CO plus H_2.

The curves show graphite in different stages of corrosion. At 1140°C and 186 mg/cm^2 burnoff, the density profile may be termed as fully established. The active reaction zone extends from a depth of approximately 0.5 mm to 1.5 mm, while a slowly reacting residue of density 0.17 to 0.2

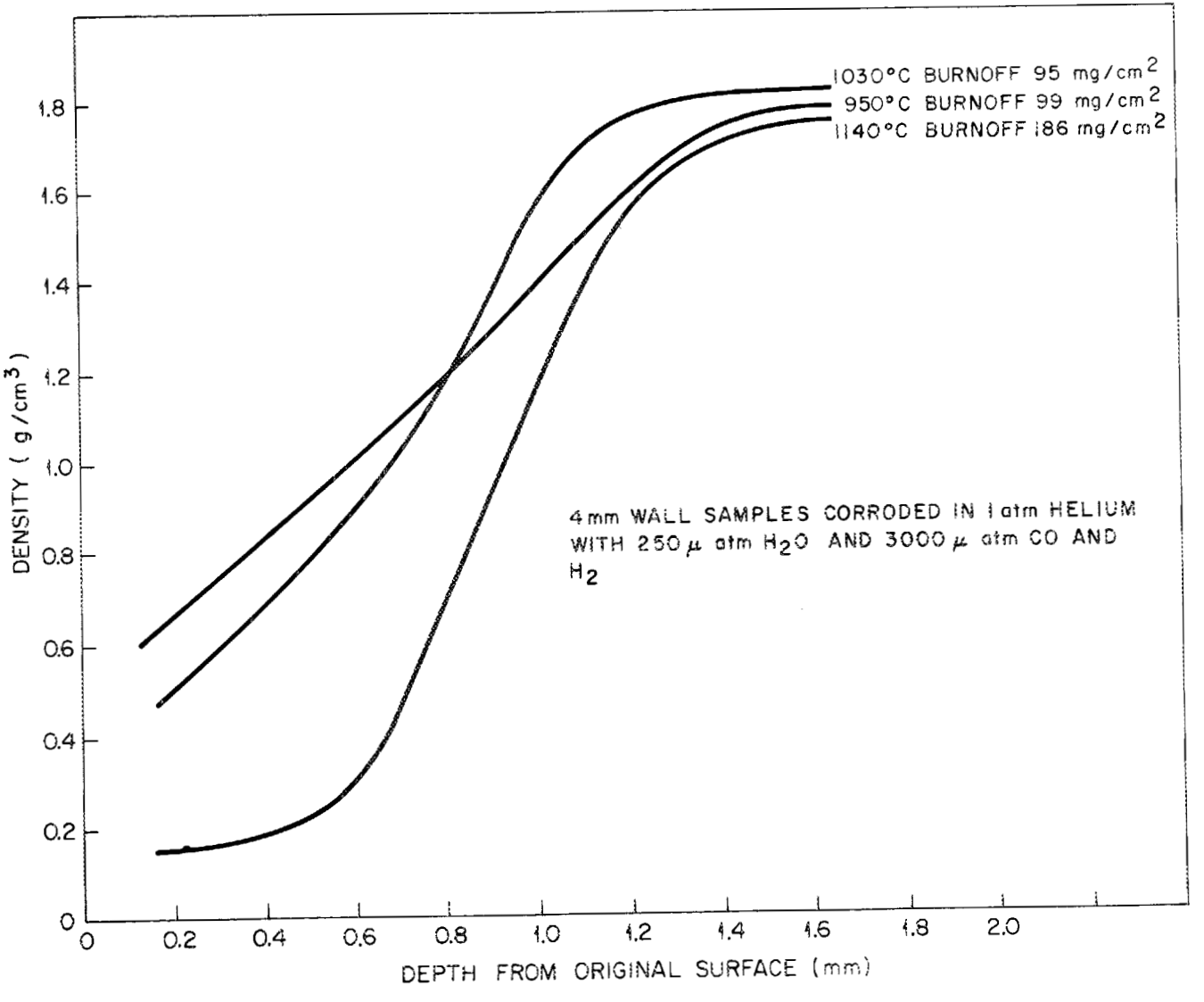

Fig. 4.5. Density profiles for graphite corrosion at various burnoffs.[10]

g/cm^3 remains on the outer 0.5 mm. The other two corrosion profiles, at 95 and 99 mg/cm^2 burnoff, have not yet achieved full establishment; however, the curve at the higher temperature appears to be closer to it.

While the evidence is rather skimpy, the burnoff profiles shown in Fig. 4.5 are consistent with the following picture of graphite corrosion under these conditions:

(1) When graphite first comes in contact with low concentrations of H_2O at high temperatures, the active reaction zone gradually moves inward from the exposed face to some equilibrium depth.

(2) The depth of the reaction zone at equilibrium, or full establishment, diminishes with increasing temperature.

(3) Following establishment of the fully developed corrosion profiles, corrosion proceeds by an inward movement of the reaction zone, leaving behind a slowly reacting residue of density 0.17 to 0.20 g/cm^3.

Depths of the fully established reaction zone as a function of temperature, estimated from the density profiles shown in Fig. 4.5, are listed in Table 4.5. The values given for the temperatures 1030 and 950°C were obtained by extending the curves shown to the left to the density range of approximately 0.2 g/cm^3. The values listed for 1200, and 900 to 700°C were obtained by linear extrapolation. The data on which this view of graphite corrosion is based are small, and should be extended to more relevant types of graphites (i.e., the HTGR reference core and structural graphites) and a broader range of corrosive atmospheres. However, no additional burnoff profile data, other than that cited from Helsby and Everett,[10] were found.

A comparison of the corrosion reaction depths given in Table 4.5 with the core-post temperature range of 786°C to 876°C in the reference design selected for this study (see Sect. 6.3), indicates the anticipated range of active corrosion depths for the core posts to be about 2 to 3 mm. Since the core posts are 6-in. in diameter, we therefore conclude that it is

Table 4.5. Estimated depth of fully established reaction zone in graphite corroded by low concentrations of steam[a]

Temperature (°C)	Reaction zone (mm)
1200	0.6[b]
1140	0.9
1030	1.4
950	1.9
900	2.1[b]
800	2.6[b]
700	3.1[b]

[a]See ref. 10.

[b]Obtained by linear extrapolation.

appropriate to view the corrosion process as a surface corrosion process. In such cases, the reaction rate is proportional to the exposed superficial area of the graphite. This also appears to be true for the portion of the core graphite with surface temperatures above approximately 750°C. This includes most of the core below the midplane where calculations outlined in Sect. 5.3 show that about 90% of the reaction of core graphite with steam occurs.

The Wicke equation [Eq. (11)] in surface units. The amount of actively corroding graphite per unit area of exposed surface of a specimen or graphite member which is large compared with the active corrosion depth, is equal to $\rho\ \Delta h$. Therefore, the appropriate conversion of units for this case is

$$R_1\left(\frac{g}{g\text{-sec}}\right)\cdot \rho\ \Delta h\left(\frac{g}{cm^2}\right) = R_2\left(\frac{g}{cm^2\text{-sec}}\right), \qquad (12)$$

where R_1 is based on specimen sizes which are smaller than the reaction depth, Δh. Thus, the conversion to surface units is temperature dependent, since Δh varies with temperature, as shown in Table 4.5. We will avoid this additional complication by selecting a value of Δh appropriate for

graphite at the average surface temperature in the lower half of the core. In Sect. 5.3, it is shown that this temperature is about 820°C for the reference design selected for this study; by interpolation in Table 4.5, this yields a value for Δh of about 0.25 cm. Hence, the desired conversion factor is

$$R_1 \left(\frac{g}{g\text{-sec}}\right) \times 0.45 = R_2 \left(\frac{g}{cm^2\text{-sec}}\right). \tag{13}$$

It is also desirable for consistancy to convert Eq. (11) to the use of partial pressures as an expression of concentration rather than mol/cm^3. The conversion is given by

$$\mu atm = C \left(\frac{mol}{cm^3}\right) \times 82.06 \times 10^6 \times T(°K), \tag{14}$$

using the ideal gas law; once again, the conversion is temperature dependent. However, it can be shown that only a small error is introduced if a representative, average temperature is selected. The exponential temperature dependency of the multiplicative rate constant is much higher and tends to mask the linear variation in Eq. (14). Thus, selecting $T = 1100°K$ yields

$$R_s \left(\frac{mol}{cm^2\text{-sec}}\right) = \frac{k_1 \mu_{H_2O}}{1 + k_2 \mu_{H_2} + k_3 \mu_{CO}} \tag{15}$$

for the modified Wicke equation, Eq. (11), where

$$k_1 = 21.4 \exp\left(-\frac{68,000}{RT}\right),$$

$$k_2 = 3.5 \times 10^{-6} \exp\left(\frac{14,500}{RT}\right),$$

$$k_3 = 2.9 \times 10^{-6} \exp\left(\frac{14,500}{RT}\right),$$

$$\mu = \mu atm.$$

4.2.3 The OXIDE-3 rate equation

The steam-graphite kinetics equation used on the OXIDE-3 program[11] is given as

$$R_v\left(\frac{\%}{hr}\right) = \frac{k_1 P_{H_2O} F_b F_c}{1 + k_2 P_{H_2}^n + k_3 P_{H_2O}}, \qquad (16)$$

where

$k_1 = 1.067 \times 10^{10} \exp\left(-\frac{40,900}{RT}\right)$, %/hr-atm,

$k_2 = 0.0166 \exp\left(\frac{28,600}{RT}\right)$, $atm^{-0.75}$,

$k_3 = 0.0531 \exp\left(\frac{27,500}{RT}\right)$, atm^{-1},

$n = 0.75$

P = atm,

F_b, F_c = burnoff and catalyst factors.

The burnoff factor is expressed as a polynominal function of the percent burnoff which varies from 0.5 at 0 burnoff to 1.7 at 10% burnoff. F_b is set to unity at 1% burnoff. The catalyst factor, F_c, is given as a temperature dependent function of the sum of the barium and strontium concentrations in the graphite, normalized to a value of unity for noncatalyzed graphite. The concentrations of barium and strontium, which are the major fission product catalysts for the steam graphite reaction, are computed by OXIDE-3 from the fission yields and diffusion from the fuel. The initial concentration of these catalytic materials is assumed to be zero. No indication of the maximum anticipated value for F_c is given in ref. 11. In the present study, the factors F_b and F_c are assumed to be unity.

Since Eq. (16) was developed from a compilation of data from a variety of sources, there is no completely rational way to convert it to units based on exposed surface area. As seen above, such conversion depends on the particular geometry of each experiment. However, an approximation can be made by noting that most of the studies on which Eq. (16) was based employed specimen sizes of about 1 to 2 cm. Hence, we will use a rough conversion

of the OXIDE-3 equation to surface units by assuming that it is based on data taken on 1-cm-diam cylinders. Thus, using Eq. (9) yields the following modified OXIDE-3 equation,

$$R_s \left(\frac{\text{mol}}{\text{cm}^2\text{-hr}} \right) = \frac{k_1 \, P_{H_2O}}{1 + k_2 \, P_{N_2}^{n} + k_3 \, P_{H_2O}} , \tag{17}$$

where

$$k_1 = 4.00 \times 10^6 \exp\left(- \frac{40,900}{RT} \right) ,$$

k_2, k_3, n = unchanged.

4.2.4 The Giberson rate equation[12]

This study was performed in support of the operation of the Hanford reactors which often have measurable CO_2 and H_2O levels in the helium coolant. Therefore, a so-called KC-graphite was selected as being the typical core graphite of one of the Hanford reactors.

Type KC graphite is made from Kendall coke and Chicago Pitch by the National Carbon Company. It is a purified, anisotropic graphite with an initial density of 1.70 g/cm^3 and an initial BET area of 0.55 m^2/g. The test samples were cylinders of 1.1 cm diam and 5 cm length. Each was preoxidized in air to 5% burnoff.

The experiments were conducted at 1 atm pressure through a temperature range of 800 to 1000°C. Steam concentrations in helium ranged from 500 to 10,000 ppm. Hydrogen levels ranged from 0 to 5000 ppm, and CO was not introduced independently. The reported data were correlated by

$$R_v \left(\frac{g}{g\text{-hr}} \right) \frac{k_1 \, P_{H_2O}}{1 + k_2 \sqrt{P_{H_2}} + k_3 \, P_{H_2O}} , \tag{18}$$

where

$$k_1 = 127 \exp\left(-\frac{32,700}{RT}\right), \text{ g/g-hr-mm},$$

$$k_2 = 1.24 \times 10^{-11} \exp\left(\frac{60,800}{RT}\right), \text{ mm}^{-1/2},$$

$$k_3 = 6.51 \times 10^{-19} \exp\left(\frac{79,300}{RT}\right), \text{ mm}^{-1},$$

$$P = \text{mm Hg}.$$

Converting the rate to a surface area basis as specified by use of Eq. (9), and converting the partial pressure values from mm-Hg to atmospheres, yields the following values for the constants,

$$P = \text{atm},$$

$$k_1 = 3990 \exp\left(-\frac{32,700}{RT}\right), \text{ mol/cm}^2\text{-hr-atm},$$

$$k_2 = 3.10 \times 10^{-10} \exp\left(\frac{60,800}{RT}\right), \text{ atm}^{-1/2},$$

$$k_3 = 4.95 \times 10^{-16} \exp\left(\frac{79,300}{RT}\right), \text{ atm}^{-1}.$$

Use of the above values in Eq. (18) yields the rate expressed as mol/cm^2-hr.

4.2.5 Comparison of corrosion rate predictions

The ATJ corrosion equation derived in Sect. 4.1 and the Wicke, OXIDE-3, and Giberson equations given in this section have been put on a common basis, expressing the predicted rates in terms of mole/cm^2-hr, and are compared here with each other for a number of representative conditions.

In addition to these four kinetics equations, two others will be included in the comparisons which are the result of less complete studies. The first of these is reported by Giberson and Walker,[13] whose data are limited to the case of no H_2 or CO in the oxidizing gas. The TSX graphite used in these studies was manufactured by the National Carbon Co. from Continental Lake Charles No. 1 coke and Allied Chemical Co. No. 30 medium coal tar pitch. The graphite was baked as bars and pitch-impregnated once. Test samples were cut from the bars to 5-cm length and 1.1 cm diameter.

The test variables ranged from 130 to 33,000 μatm P_{H_2O} and from 750° to 900°C. The results were correlated by

$$R_v \left(\frac{g}{g\text{-hr}} \right) = 4.78 \times 10^9 \exp\left(- \frac{70,200}{RT} \right) \sqrt{P_{H_2O}} , \qquad (19)$$

with P given in millimeters of mercury.

The second additional set of data included in this comparison are given by Helsby and Everett[10] for three graphites designated as "reference graphite," "graphite No. 1," and "graphite No. 96." The latter two are molded, isotropic Gilsocarbon graphites, while the first is not otherwise identified. These tests were limited to P_{H_2O} = 250 μatm, $P_{H_2} + P_{CO}$ = 3000 μatm, while the temperature was varied from 950 to 1150°C.

Figure 4.6 compares predicted reaction rates at P_{H_2} = 1000 μatm and $P_{H_2} + P_{CO}$ = 3000 μatm as a function of temperature. The actually observed temperature range inclusive for each study is indicated in the figure by the heavy band. Note that at 800°C about a factor of 10 range exists from the ATJ to the lowest value predicted by Giberson. At 900°C the span between ATJ, OXIDE-3, Wicke, and Giberson predictions narrows to about a factor of 3. At 1000°C, the range predicted by these four rate equations widens to about a factor of 4.

Figure 4.7 illustrates the comparison for no H_2 or CO added to the oxidizing gas. In this case, the predictions range through a factor of 6, 2, 5, and 20 at 700, 800, 900, and 1000°C, respectively.

The variation of predicted corrosion rates as a function of P_{H_2O} at T = 900°C and 3000 μatm of CO + H_2 is shown in Fig. 4.8. The span of predictions ranges through a factor of 5 for P_{H_2O} values less than about 500 μatm, excluding the high values of Helsby and Everett. From 500 μatm and up to about 3000 μatm H_2O, the predictions converge to within a factor of about 2.

Figure 4.9 shows the same comparison with no H_2 or CO added to the oxidizing gas, a condition which permits comparison with data of Giberson and Walker.[13] The predictions diverge much more than is shown in Fig. 4.8. The range is a factor of about 30 at 10 μatm H_2O and converges to a factor of 5 at 1000 μatm H_2O.

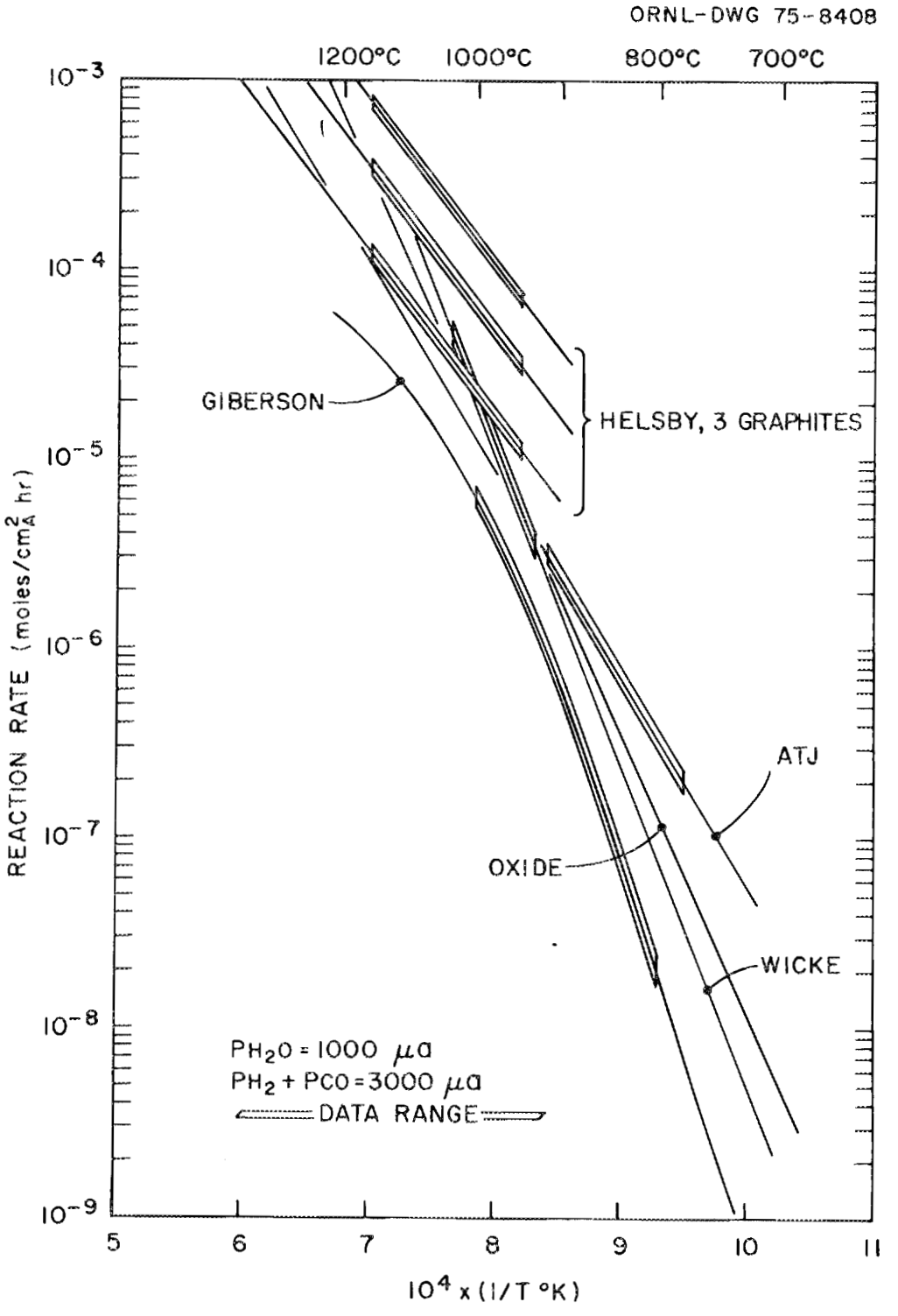

Fig. 4.6. Reaction rate vs 1/temperature at P_{H_2O} = 1000 μatm, P_{H_2} + P_{CO} = 3000 μa.

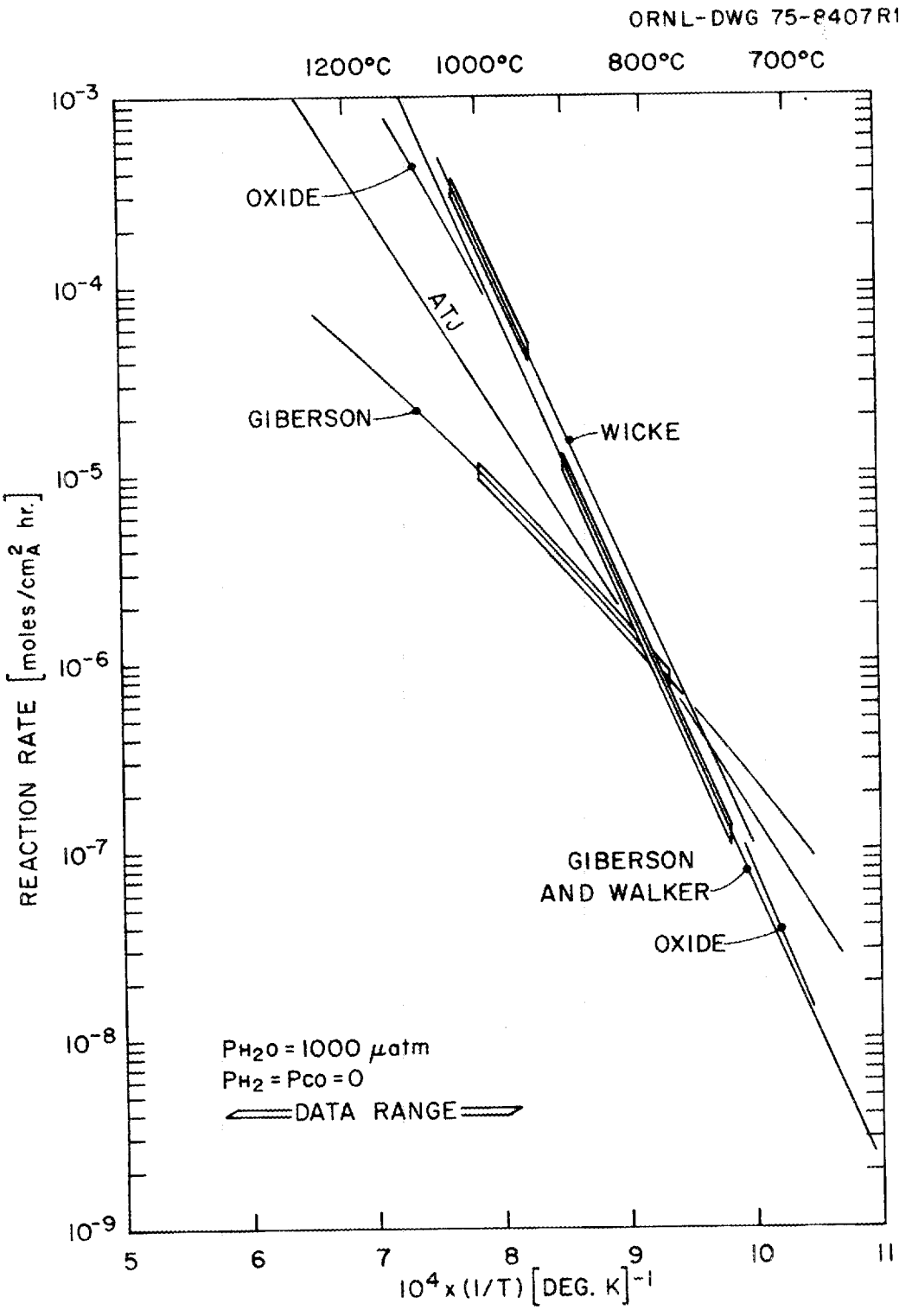

Fig. 4.7. Reaction rate vs 1/temperature at P_{H_2O} = 1000 μatm, $P_{CO} + P_{H_2} = 0$.

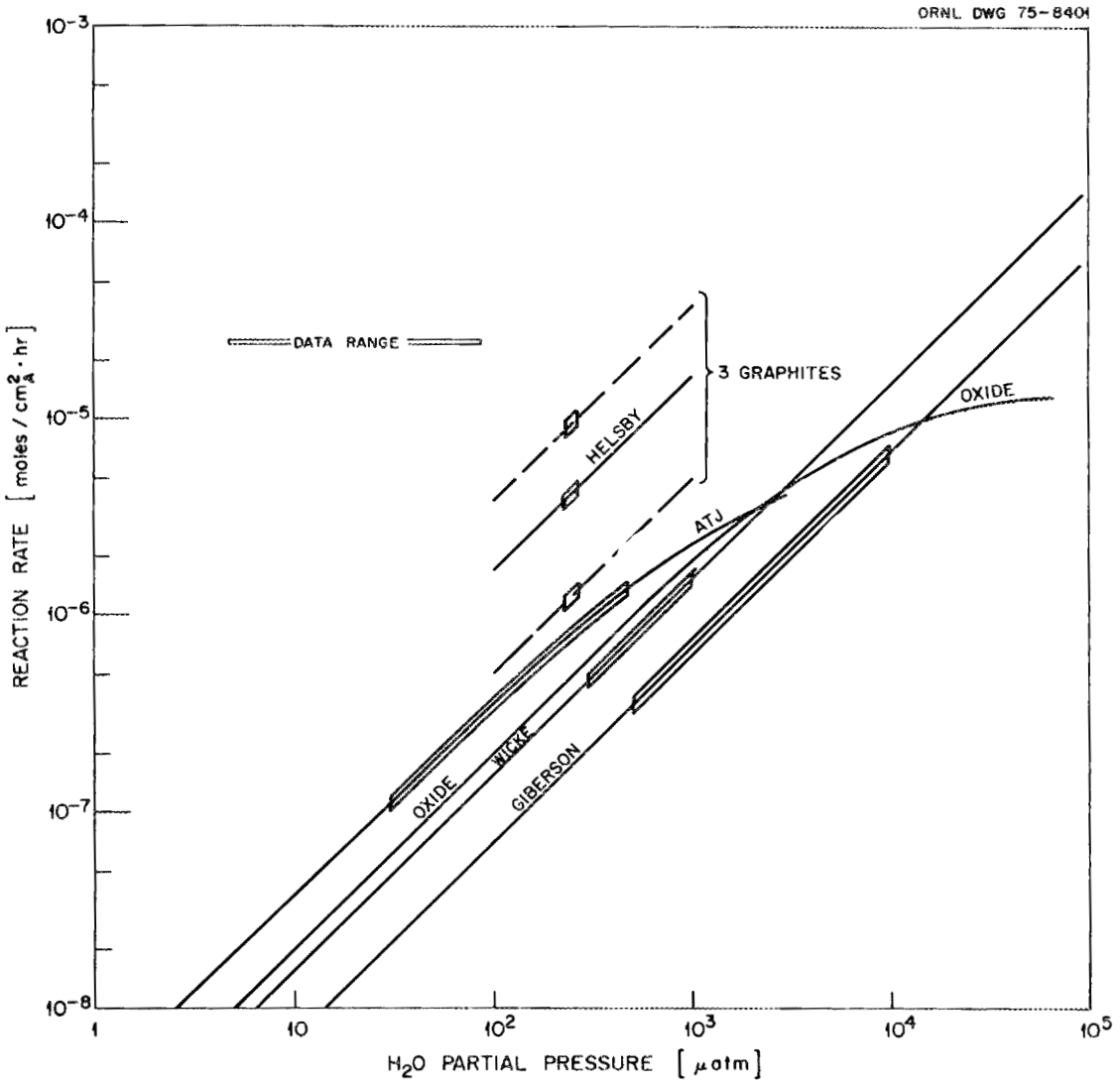

Fig. 4.8. Variation of reaction rate with P_{H_2O} at 900°C; $P_{H_2} + P_{CO} = 3000$ μatm.

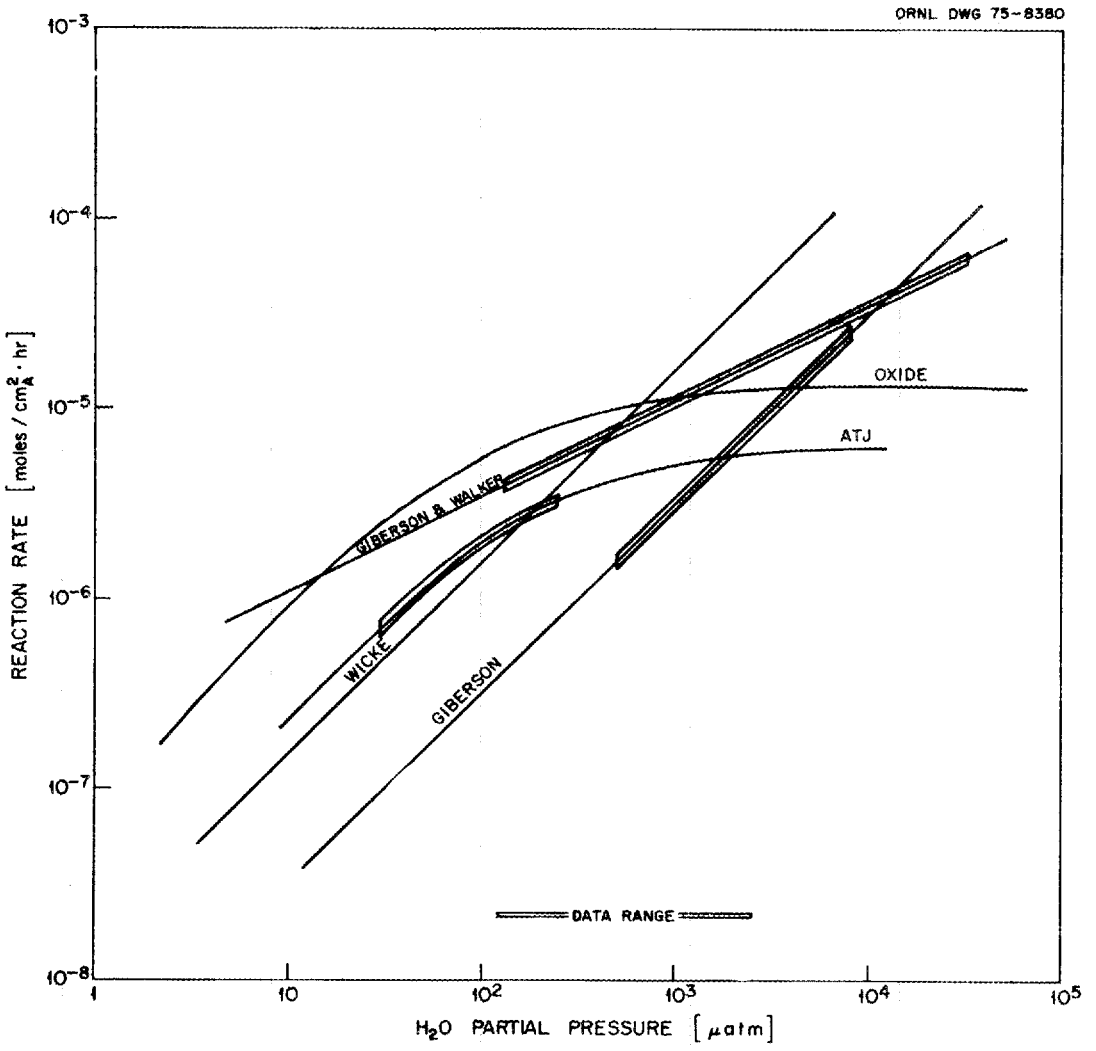

Fig. 4.9. Variation of reaction rate with P_{H_2O} at 900°C; $P_{H_2} = P_{CO} = 0$.

4.3 References for Section 4

1. J. P. Blakely and L. G. Overholser, "Oxidation of ATJ Graphite by Low Concentrations of H_2O and CO_2 in Helium," Carbon 3, 269-75 (1965).

2. L. G. Overholser and J. P. Blakely, "Oxidation of Graphite by Low Concentrations of H_2O and CO_2 in Helium," Carbon 2, 385-94 (1965).

3. J. L. Rutherford et al., Oxidation of Fueled and Unfueled Graphite Spheres by Steam, ORNL-3947 (May 1966).

4. Nuclear Safety Program Annual Progress Report for Period Ending 12/31/66, W. B. Cottrell, Prog. Div., ORNL-4071 (March 1967), pp. 104-106.

5. The Industrial Graphite Engineering Handbook, National Carbon Company, 1964.

6. C. Meyers and K. Koyama, Evaluation of Candidate Graphites for PSC Core Support Applications, GAMD-8371 (February 1968).

7. M. B. Peroomian, A. W. Barsell, and J. C. Saeger, OXIDE-3: A Computer Code for Analysis of HTGR Steam or Air Ingress Accidents, GA-A12493 (GA LTR-7) (January 1974), Fig. 3-9.

8. E. Wicke et al., Corrosion Rate of Graphites by CO_2 and H_2O, D.P. Rep. 391 (January 1966).

9. M. R. Everett, D. V. Kinsey, and E. Römberg, "Carbon Transport Studies for Helium Cooled High Temperature Reactors," in Chemistry and Physics of Carbon, vol. 3, ed. by P. L. Walker, Marcel Dekker, New York, 1967.

10. G. H. Helsby and M. R. Everett, Some Graphite Corrosion Problems Related to Helium-Cooled HTR's, D.P. Rep. 566 (August 1968).

11. M. B. Peroomian, A. W. Barsell, and J. C. Saeger, OXIDE-3: A Computer Code for Analysis of HTGR Steam or Air Ingress Accidents, GA-A12493 (LTR-7) (January 1974).

12. R. C. Giberson, Rate Constants for the Reaction of CO_2 and H_2O with KC Graphite, BNWL-CC-1381 (August 1974).

13. R. C. Giberson and J. P. Walker, Reaction of TSX Graphite with Water Vapor, HW-SA-3439 (April 1964).

5. ESTIMATED IMPURITY LEVELS IN THE PRIMARY SYSTEM

The first step in assessing the degree of core post damage caused by the corrosive effect of impurities in the primary system is to estimate their level and composition. Since the total steady-state impurity concentration depends solely on the relative rates of ingress and purification flow, the problem becomes that of distributing the total level between oxidizing species and the products of corrosion which act as inhibitors.

A considerable simplification is achieved if we may neglect the spatial dependence of impurity level within the primary system. That this is in fact the case is shown in the next section.

5.1 Variation of Impurity Level with Axial Location in the Coolant Channel

Since the circuit time of coolant in the primary system is quite short (i.e., somewhere between 3.7 and 7.1 sec, as discussed below) one may suspect that a valid approximation would be to treat the primary coolant as a mixed pot for the purpose of defining the corrosive atmosphere around the core support posts.

Section 5 of the Delmarva Power and Light Preliminary Safety Analysis Report gives the circuit time of coolant in the primary system as 3.7 sec.[1] A somewhat higher value is obtained from the given total coolant flow[1] of 7.48×10^6 lb_m/hr (3.39×10^6 kg/hr) and helium inventory[2] of 14,700 lb_m (6670 kg), which yields a circuit time of 7.1 sec. A further intuitive judgment that primary system concentrations are more or less uniform is obtained by noting that the coolant transit time through the core is approximately 0.2 sec (core height = 26 ft divided by an average velocity of about 150 ft/sec).

A simple program termed TUBOX has been used to estimate the degree to which concentrations vary axially in the core. TUBOX divides a single coolant channel into ten axial sections, eight sections of 80 cm each for the active core, plus two sections for the top and bottom reflector. The graphite and coolant temperatures are specified for each of the ten zones as input data. Each of the ten zones are further subdivided into ten

smaller subdivisions through which the impurity level change is computed from

$$[H_2O]_{i+1} = [H_2O]_i - R_i \, \pi d \, \Delta z/Q_i \quad , \tag{1}$$

$$[H_2O]_{i+1} = [H_2]_i + R_i \, \pi d \, \Delta z/Q_i \quad , \tag{2}$$

where

R_i (mol/cm^2-sec) = the reaction rate at the temperature specified for the zone,

d = the coolant channel diameter,

Δz = the incremental length, usually taken as 8 cm,

Q_i = the volumetric flow computed for each zone from the specified coolant temperature and the mass flow rate.

Finally, the impurity levels at the inlet are needed, which are also specified as input.

Some typical TUBOX results are shown in Fig. 5.1. The graphite surface temperatures for each of the ten axial zones are shown for an average channel from a region with approximately unity radial power factor. The mass coolant flow for such an average channel is 37.8 g/sec. The reaction rate, as computed using the Wicke rate equation [Eq. (15), in Sect. 4] is seen to vary greatly in the coolant channel under the influence of the temperature variation. However, the partial pressure of H_2O, assumed here to be 10^{-3} atm at the inlet, changes very little. For this calculation, the reaction rate computed from Eq. (15) of the previous chapter has been reduced by the factor $1/\sqrt{P_T}$, where P_T is the total pressure in the coolant channel of 49 atm. This correction is required because the original equation pertains to conditions at 1 atm, at which rates are higher. The theoretical basis for the correction, which is given in a number of reviews (e.g., Walker et al.[3]) rests on the idealized assumption that gas-phase diffusion within the graphite pores controls the total reaction rate. This results in the prediction that the observed reaction rate is proportional to the square root of the effective diffusivity of H_2O in helium. The final form of the corrective factor is obtained by noting that gas

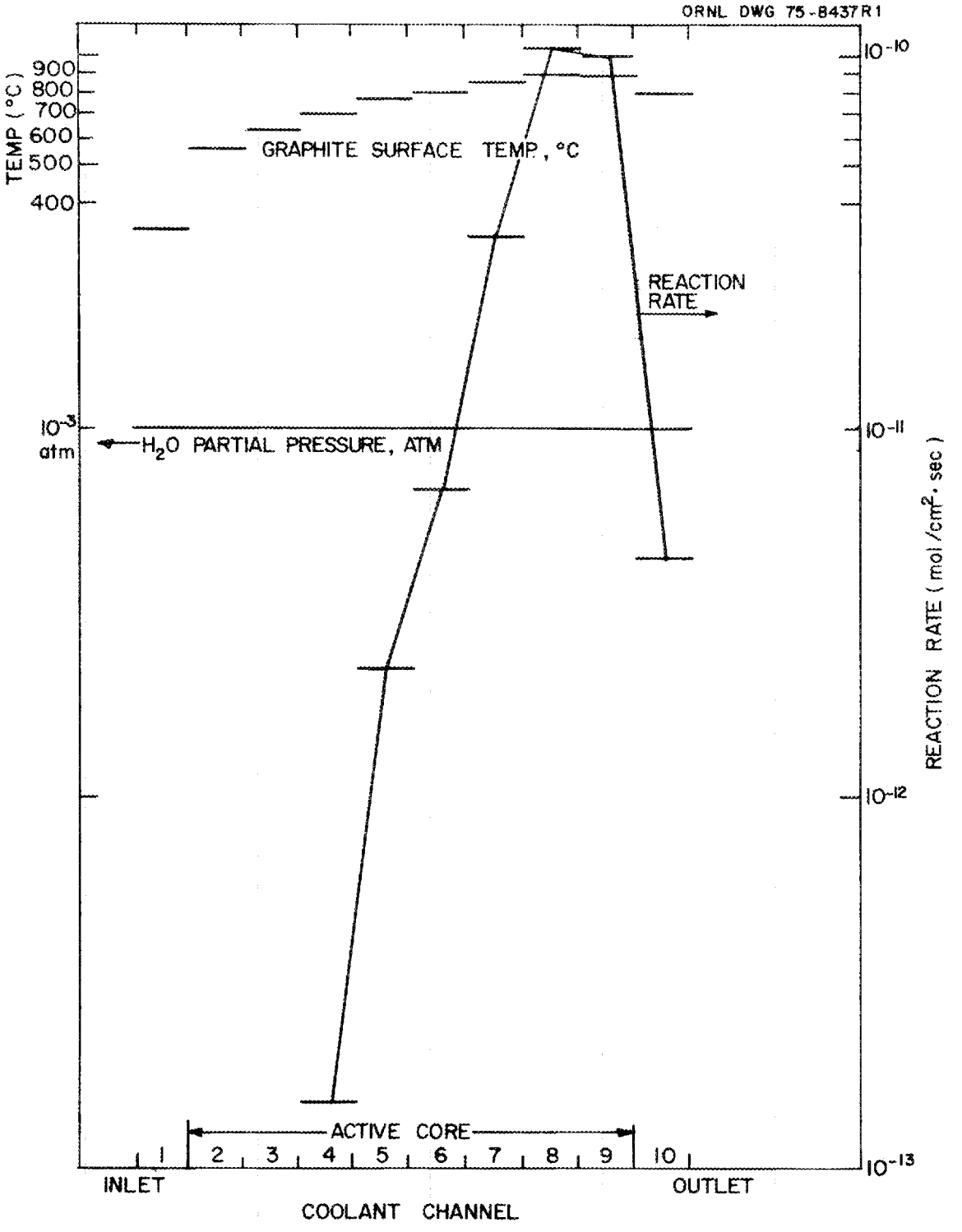

Fig. 5.1. Typical variation of H_2O partial pressure and reaction rate in a coolant channel computed from TUBOX.

phase diffusion coefficients vary approximately inversely with total pressure.

Results similar to those shown in Fig. 5.1 were obtained for a high power factor channel, where both the graphite temperatures and mass flows are higher, and also for the lowest radial power factors channels, where mass flows drop to 15.1 g/sec. We therefore conclude that the calculational simplification afforded by treating the primary system as a mixed pot for the purpose of determining the corrosive environment in the vicinity of the core support posts is valid.

5.2 Impurity Concentrations Using Core Reactivity to Steam Corrosion Derived from Dragon Steam Ingress Data

In the years 1966 through 1968, a series of impurity addition experiments, described by Carlyle and Kinsey,[4] was conducted at the Dragon Reactor. The first of these was a series of four H_2O additions at a rate of 2 to 3 g/hr, each extending for approximately 30 hr. Experimental conditions varied somewhat during the course of the experiments; however, the concentrations of H_2O and reaction products began to level out about 12 hrs after initiation of the experiment. Though the impurity levels did not appear to be completely equilibrated in the 30-hr test duration, we will use the reported concentrations at the end of injection as an indicator of core reactivity to the steam corrosion reaction. Subsequently, by comparing Dragon and HTGR primary loop conditions, we can obtain a corresponding reactivity of an HTGR core from which HTGR impurity levels will be estimated.

5.2.1 Results of Dragon steam ingress experiments

The results of four Dragon steam ingress runs are shown in Table 5.1 together with normal impurity levels experienced with no steam addition.[4] With no deliberate steam addition, the H_2O concentration is measurable, but small; the H_2 level is $\sim$ 1.4 vpm, somewhat higher than the normal CO level of $\sim$ 0.75 vpm. With H_2O added deliberately, the sum of hydrogen content of the hydrogen bearing species,

$$\Sigma[H] = 2[H_2O] + 2[H_2] + 4[CH_4], \qquad (2)$$

Table 5.1. Steady-state impurity levels established during Dragon steam ingress experiments, and normal impurity levels with zero ingress

	Injection rate $\left(\frac{mol}{hr}\right)$	Purification flow $\left(\frac{g}{sec}\right)$	Equilibrium concentrations (vpm)					$\Sigma[H]$ (vpm)	$\Sigma[O]$ (vpm)
			H_2O	H_2	CO	CO_2	CH_4		
1	0.153	9.0	6.0	6.3	2.37	0.91	0.38	26.1	8.19
2	0.172	11.0	3.2	7.6	3.5	1.3	0.21	22.1	9.30
3	0.172	7.5	4.2	13.1	7.0	2.1	0.45	36.4	15.4
4	0.122	7.0	3.6	7.3	5.7	1.5	0.35	23.2	12.3
-	0	(nominal)	~ 0.075	~ 1.4	~ 0.75	~ 0.02	~ 0.15		

shown in the next to last column, is approximately twice the sum of oxygen in the oxygen bearing species, $\Sigma[O]$. This is as it should be since H and O are added in this ratio. This feature lends some confidence in the reported results.

5.2.2 Interpretation of Dragon steam ingress results

In order to interpret the Dragon steam ingress data in terms of an effective core reactivity, we will assume that a first order reaction occurs between the core graphite and steam, forming CO and H_2 as primary products. The data of Table 5.1, however, show significant CO_2 formation which necessitates some interpretation in order to arrive at a single effective core reactivity. The smaller quantity of CH_4 produced will be neglected.

The rate of the steam/graphite reaction is assumed to be represented by the first order expression

$$R = K_c\,[H_2O] \quad , \tag{3}$$

where

R = reaction rate, mol/sec,
K_c = core reactivity, cm^3/sec,
$[H_2O]$ = H_2O concentration in the primary system, mol/cm^3.

Thus, since W mol/sec of H_2O enter the primary system and $Q_p \cdot [H_2O]$ leave, where Q_p is the purification flow as cm^3/sec, we obtain the equilibrium H_2O level by a mass balance,

$$[H_2O] = \frac{W}{K_c + Q_p} \quad . \tag{4}$$

The concentration of any consitituent not altered by its residence in the core may be obtained from Eq. (4) with K_c set equal to zero; for example,

$$\Sigma[O] = \frac{W}{Q_p} \quad , \text{ and} \tag{4a}$$

$$\Sigma[H] = \frac{2W}{Q_p} \quad . \tag{4b}$$

Rearranging Eq. (4) to solve for the core reactivity yields

$$K_c = \frac{W - Q_p [H_2O]}{[H_2O]} \cdot \tag{5}$$

Similarly, a mass balance for H_2 yields the following, assuming H_2 formation only from the reaction of steam with graphite,

$$[H_2] = \frac{K_c}{Q_p} \frac{W}{K_c + Q_p} \cdot \tag{6}$$

Again, rearranging Eq. (6) to solve for the core reactivity yields

$$K_c = \frac{Q_p^2 [H_2]}{W - Q_p [H_2]} \cdot \tag{7}$$

We have assumed a highly simplified model in order to interpret the Dragon steam ingress data in terms of a single value for the core reactivity. However, the corrosion reaction is not first order as assumed here, and at least three constants are needed to specify the reaction rate. Additionally, the significant amounts of CO_2 which show up indicate that reactions other then the assumed steam/graphite corrosion reaction takes place. Nevertheless, the small number and the uncertain precision of the data do not warrant the inclusion of these secondary considerations.

Effective inleakage rate. Table 5.2 illustrates one of the uncertainties in the interpretation of the Dragon steam inleakage data. Columns 1 and 2 record inleakage and purification flows given in Table 5.2 in new units, the volumetric purification flow being calculated from the mass flows of Table 5.1, assuming a mixed-mean primary loop temperature of 593 °C. [Dragon primary loop characteristics pertinent to this section are given in Table 5.5.] The third and fourth columns of Table 5.2 list the anticipated levels of the total oxygen and hydrogen-bearing species corresponding to the given values for W and Q_p calculated using Eqs. (4a) and (4b). Columns 5 and 6 record the corresponding measured values from Table 5.1, while the last two columns list the ratios of measured to expected values.

Note that for all cases, the measured value is less than the anticipated value for both oxygen and hydrogen bearing species. Several possible explanations for this observation follow:

Table 5.2. Comparison of measured to anticipated impurity levels in the Dragon steam ingress experiment

W ($\frac{mol}{sec}$)	Q_p ($\frac{cm^3}{sec}$)	Anticipated $\Sigma[O]$ (vpm)	Anticipated $\Sigma[H]$ (vpm)	Measured $\Sigma[O]$ (vpm)	Measured $\Sigma[H]$ (vpm)	Ratio Measured/anticipated $\Sigma[O]$	Ratio Measured/anticipated $\Sigma[H]$
4.25 E-5	8000	18.9	37.8	8.19	26.1	0.433	0.690
4.78 E-5	9740	17.9	35.8	9.30	22.1	0.520	0.617
4.78 E-5	6660	25.5	51.0	15.4	36.4	0.604	0.714
3.39 E-5	6220	19.4	38.7	12.3	23.2	0.634	0.599
					Av	0.548	0.655

(1) A higher purification flow than recorded by Carlyle and Kinsey[4] could account for the observed discrepancy. For example, if the normal fuel element purge flow[2] of 7 g/sec were occurring and not included as a part of the effective stated purification flow as it should have been, the correction for this hypothesized oversight would bring the anticipated and measured impurity levels into closer agreement.

(2) A large portion of the injected H_2O may have been adsorbed in various locations in the primary system and, hence, contributed nothing to the impurity atmosphere. Indeed this is judged to be likely for a large scale experiment such as this; in fact, this is the explanation of the discrepancy put forth by Carlyle and Kinsey.

(3) Carlyle and Kinsey discuss other conceivable sources of error which may result from the analytical methods employed, such as errors in the reported concentrations obtained by gas chromatograph. Errors of this type may account for some scatter but cannot account for the generally low values of impurity levels while maintaining the proper H/O ratio.

Thus, the second explanation is regarded as most likely. If we presume the lost portion of the injected water to be permanently adsorbed, we may simply subtract this portion from the stated ingress flow for the production of the observed gaseous corrosion products. Thus, the effective ingress flows listed below in Table 5.3 are 60.2% of those listed in Tables 5.1 and 5.2 (average of 54.8 and 65.5%).

Table 5.3. Revised Dragon steam ingress data

H_2O ingress rate $\left(\frac{mol}{sec}\right)$	Purification flow $\left(\frac{cm^3}{sec}\right)$	Revised impurity levels		
		H_2O (vpm)	H_2 (vpm)	CO (vpm)
2.57 E-5[a]	8000	6.91	5.39	3.28
2.89 E-5	9740	4.3	6.3	4.8
2.89 E-5	6660	6.3	11.0	9.1
2.05 E-5	6220	5.1	5.8	7.2

[a]This notation signifies 2.57×10^{-5}.

Method of accounting for the CO_2 production. The question arises on how to incorporate CO_2 production into this simple framework which presumes a single value for the core reactivity for the reaction of graphite with H_2O to form CO and H_2. As seen in Table 5.1, significant amounts of CO_2 were produced in the Dragon Experiments, evidently from the radiation-catalyzed shift reaction taking place in the gas phase, probably in the cooler portions of the primary loop.

$$H_2O + CO \rightarrow CO_2 + H_2 \ . \qquad (8)$$

Carbon dioxide is unstable at low partial pressures above ~ 500°C; hence, we expect the reverse of Eq. (8) to occur in hot zones. The net effect of the forward shift reaction is to replace H_2O and CO with an equal amount of CO_2 and H_2.

It is generally accepted that the thermally activated corrosive effect of CO_2 on graphite via

$$CO_2 + C \rightarrow 2\ CO \qquad (9)$$

is slower than the corresponding reaction of H_2O. Clark et al.[5] state that the steam-graphite reaction is about three times more rapid than the corresponding reaction with CO_2. Wicke et al.[6] report that for crushed, type G4 graphite, the corrosion rate with H_2O was 6.4 times that for CO_2 at 1000°C and 20 atm total pressure, with an impurity composition of 30 vpm CO_2, 20 vpm H_2O, 300 vpm CO, and 200 vpm H_2. Wicke also observed that the rate of the H_2O-graphite reaction is not markedly effected by the presence of CO_2.

While the CO_2-graphite thermal reaction is inherently slower than the H_2O-graphite reaction by approximately a factor of 5, there is evidence that radiation enhances the corrosive effect of CO_2 to a far greater degree then H_2O. Giberson and Tingey[7] assume a G-value for the reaction of CO_2 with graphite which is about four times the value for the H_2O reaction: 1.35 molecules/100 ev for the CO_2 + C reaction, compared with 0.35 for H_2O.

In an HTGR coolant environment, radioactive energy is absorbed directly, primarily by the preponderant helium atoms which are thus driven into a variety of excited states.[7,8] These excited helium atoms then transmit their excitation energy either to impurity atoms, nonexcited helium atoms, or adjacent solid material. Evidently, radiolytic decomposition of CO_2 to CO and highly reactive oxygen occurs at a significant rate, whereas the corresponding radiolysis of H_2O occurs to a much lesser degree.[8] Therefore, there is good reason to anticipate radiolytic enhancement for the CO_2 + C reactions to a much greater degree than for H_2O + C.

This is indicated to be the case for data reported by Everett et al.,[8] who show an enormous enhancement by radiation for CO_2 corrosion — a factor of 100 at 800°C and a factor of 10 at 900°C — compared with more modest enhancements for H_2O. Thus, it appears that at least approximately irradiative enhancement tends to equalize the corrosive effect of CO_2 and H_2O on core graphite.

The shift reaction also substitutes H_2 for an equal amount of CO. Both of these are corrosion products which therefore may be expected to inhibit the corrosion reaction; however, there is some disagreement on this point. Of the four kinetics studies summarized in Sect. 4.2 that were extensive enough to allow development of a kinetics equation, only one explicitly incorporates CO as an inhibitor. That one study, reported by Wicke et al.,[9] seems to be the most extensive and careful H_2O-graphite experiment undertaken. In this study, the subject of CO inhibition was explored explicitly in a series of runs at 1030°C and 1000-vpm H_2O in which the CO and H_2 inlet concentrations were varied separately. The conclusion was that both CO and H_2 are intrinsically inhibitory to approximately the same degree. M. R. Everett et al.[10] concurred with this conclusion after examining the same data.

Summarizing then, the effect of the gas phase shift reaction is to substitute CO_2 for an equal amount of H_2O, both of which have approximately equivalent corrosive effect on graphite in a radiation field. Additionally, H_2 is produced by the shift reaction, taking the place of an equal amount of CO, and both species have an approximately equal inhibitory effect. Further, the shift reaction is most likely reversible, forming H_2O and CO from CO_2 and H_2 in higher temperature areas where CO_2 is not a thermodynamically stable species. Thus, since the shift reaction takes place in the gas phase and not with the graphite itself, and since its products have approximately equal corrosive and inhibition effects, we conclude that the most appropriate way to incorporate the shift reaction into our present simple framework is to computationally restore the products of this reaction by the original reactants.

5.2.3 Estimated Dragon core reactivity

Based on the discussion of the previous section, the data of Table 5.1 have been modified as indicated and presented in Table 5.3. Steam ingress rates are 60.2% of the originally reported values, reflecting the estimated permanent loss of 39.8% of the injected moisture. The reported CO_2 concentrations, presumed to arise from the gas phase shift reaction, plus an equal amount of H_2 have been subtracted from the reported

concentrations, and were redistributed as H_2O and CO. Thus, Table 5.3 reflects the situation if the shift reaction had not occurred. The smaller amounts of methane have been neglected.

Table 5.4 lists the effective Dragon core reactivities to H_2O corrosion based on these modified data. The values in column 2 are calculated from the H_2O concentrations using Eq. (5). Values listed in the last column are calculated from Eq. (7) using the average of the H_2 and CO concentrations. The average reactivity calculated by each method is sufficiently close, so the eight values have been combined to yield an average core reactivity of 8610 $\pm$ 2100 cm^3/sec.

Table 5.4. Dragon core reactivity to H_2O corrosion

H_2O concentration $\left(\frac{mol}{cm^3}\right)$	Core reactivity Eq. (5) K_c $\left(\frac{cm^3}{sec}\right)$	Average H_2 and CO concentration $\left(\frac{mol}{cm^3}\right)$	Core reactivity Eq. (7) K_c $\left(\frac{cm^3}{sec}\right)$
1.94 E-9	5250	1.22 E-9	4900
1.21 E-9	9740	1.56 E-9	10800
1.77 E-9	9670	2.84 E-9	12600
1.43 E-9	8120	1.83 E-9	7770
Average =	8190 $\pm$ 1530		9020 $\pm$ 2680
Average of 8 values: K_c = 8610 $\pm$ 2100			

5.2.4 HTGR core reactivity

Since the 2000 MW(t) HTGR core has about a factor of 100 larger surface area than Dragon, we expect a substantially larger core reactivity for the HTGR core. Partially tending to compensate for the larger core area is the higher coolant pressure and somewhat lower core average temperature of the HTGR, both of which tend to lower reactivity.

We have defined the core reactivity, K_c, so that

$$R\left(\frac{\text{mol}}{\text{sec}}\right) = K_c[H_2O], \tag{10}$$

where R is the total core corrosion rate. On the other hand, kinetics equations based on tests conducted at 1 atm are written in the form,

$$R\left(\frac{\text{mol}}{\text{cm}^2 \cdot \text{sec}}\right) = \frac{k_1 \cdot \exp\left(-\frac{\Delta H}{RT}\right) \cdot [H_2O]}{1 + \Sigma\, k_i [I]_i} \tag{11}$$

where k_1 is an intrinsic property of the graphite, and k_i and $[I]_i$ represent the various possible inhibition terms which are also temperature dependent, but to a lesser degree.

If the reaction rate were diffusion controlled, as virtually the entire core is expected to be, the factor $1/\sqrt{P_T}$ is conventionally applied to allow for the variation of reaction rate with the total primary loop pressure, P_T. Thus from Eq. (11) and the definition of K_c, we obtain the following relationship between HTGR and Dragon core reactivities:

$$\frac{K_c(\text{HTGR})}{K_c(\text{Dragon})} = \frac{\left[\frac{A_c \cdot \exp\left(-\frac{\Delta H}{RT_c}\right)}{\sqrt{P_T}}\right]_{\text{HTGR}}}{\left[\frac{A_c \cdot \exp\left(-\frac{\Delta H}{RT_c}\right)}{\sqrt{P_T}}\right]_{\text{Dragon}}} \tag{12}$$

where approximately equivalent impurity levels resulting in approximately equal inhibition factors have been assumed, as well as approximately equal values for the intrinsic graphite reactivities, k_1. If the ratio of the intrinsic graphite reactivities were known, they should be used as a factor in Eq. (12). A_c is the core surface area, and T_c the average core surface temperature.

Table 5.5 lists the pertinent comparative characteristics of the Dragon and HTGR reactors needed to relate the estimated Dragon reactivity to the larger reactor. The HTGR data pertain to the 2000 MW(t) reference

reactor used for this study, and described in Sect. 1.3. The Dragon data are taken from ref. 11, and pertain to the core containing 37 elements designated as Mark VII.

Table 5.5. Comparison of Dragon and HTGR characteristics relating to core reactivities

	HTGR [2000 MW(t)]	Dragon
Core surface area, cm^2	9.57 E7	8.33 E5
Coolant temperatures, °C		
Inlet	338	385
Outlet	785	800
Coolant pressure, atm	49	20
Average core heat flux, W/cm^2	19.6	24
Coolant Reynolds No.	59,000	~ 20,000
Average heat transfer coefficient, $BTU/hr\text{-}ft^2\text{-}°F$	285	211
Average surface temperature, °C	689	793

The average core surface temperature given in the last line is computed from the average coolant temperature plus the surface temperature rise

$$T_c = \frac{1}{2}\,(T_{inlet} + T_{outlet}) + \frac{q_w}{h}\,, \tag{13}$$

where q_w is the average surface heat flux and h the average heat transfer coefficient; T_c for the HTGR is 103 °C less than for Dragon.

Substituting the appropriate values into Eq. (12), and assuming ΔH = 50,000 cal/mol yields,

$$\frac{K_c(\text{HTGR})}{K_c(\text{Dragon})} = 115.\ \text{x}\ 0.0799\ \text{x}\ 0.639 = 5.87, \tag{14}$$

where the first factor, 115, is the area ratio, the second factor results

from the HTGR's cooler core, and the last factor results from the higher pressure of the HTGR. Therefore, using K_c(Dragon) = 8610 ± 2100 cm^3/sec, as derived in Sect. 5.2.3, yields for the HTGR,

$$K_c(\text{HTGR}) = 50{,}600 \pm 12{,}300 \text{ cm}^3/\text{sec}. \tag{15}$$

5.2.5 Estimated HTGR impurity levels derived from Dragon steam ingress data

A value for the HTGR core reactivity of 50,600 ± 12,300 cm^3/sec was estimated in Sect. 5.2.4 corresponding to a range between $K_{c,max}$ = 62,900 and $K_{c,min}$ = 38,300, roughly a factor of 2. The uncertainties of this estimate are probably larger than indicated by this range, which is a result solely of scatter from the four experiments involving eight determinations. For example, there is uncertainty as to the relative intrinsic graphite reactivities that involve relative values of the constants k_1 in Eq. (11) between HTGR and Dragon graphite. Another source of uncertainty relates to the 40% of added moisture which was presumed "lost" in the steam ingress experiment (i.e., did not produce detectable gaseous corrosion products).

We will express the impurity levels dependent on purification and assumed steam ingress as follows: The concentration of total oxygen-bearing species, $[O_T]$ may be obtained from Eq. (4a),

$$\left[O_T\right]_{vpm} = 10^6 \cdot \frac{RT}{P_T} \cdot \frac{W}{Q_p} \quad . \tag{16}$$

The fraction of total oxygen-bearing species which exists as oxidant, H_2O, is obtained by dividing Eq. (4a) by Eq. (4),

$$\frac{\left[H_2O\right]}{\left[O_T\right]} = \frac{Q_p}{K_c + Q_p} \quad . \tag{17}$$

Calculated levels of total oxygen, H_2O, CO, and H_2 concentration for the reference HTGR are listed in Table 5.6 using the upper and lower estimates of core reactivity of 62,900 and 38,300 cm^3/sec. Cases 1 through 4 show the effect of varying ingress rate at the nominal purification flow, whereas in cases 5 through 8 the purification flow is varied from on-half to ten times the nominal value at a constant ingress of 0.01 g/sec of

Table 5.6. HTGR impurity levels at various assumed ingress flows and purification rates estimated from Dragon steam ingress data

	Steam ingress rate $\left(\frac{g}{sec}\right)$	Purification rate $\left(\frac{cm^3}{sec}\right)$	Purification rate assumed nominal	Total oxygen concentration (vpm)	Impurity concentration ratios $K_c = 62,900\ cm^3/sec$ $\frac{[H_2O]}{[O_T]}$	$K_c = 62,900\ cm^3/sec$ $\frac{[H_2]}{[O_T]}$	$K_c = 38,300\ cm^3/sec$ $\frac{[H_2O]}{[O_T]}$	$K_c = 38,300\ cm^3/sec$ $\frac{[H_2]}{[O_T]}$
1	0.001	91,300	1	0.85	0.592	0.408	0.704	0.296
2	0.01	↓	↓	8.5	↓	↓	↓	↓
3	0.1	↓	↓	85.0	↓	↓	↓	↓
4	1.0	↓	↓	850.0	↓	↓	↓	↓
5	0.01	45,600	1/2	17.0	0.420	0.580	0.544	0.456
6	↓	91,300	1	8.5	0.592	0.408	0.704	0.296
7	↓	365,200	4	2.1	0.853	0.147	0.905	0.095
8	↓	913,000	10	0.85	0.936	0.064	0.960	0.040

moisture. These values are plotted in Figs. 5.2 and 5.3. Figure 5.2 and Table 5.6 show that at the nominal purification flow, about 65% of the incoming moisture remains as H_2O at equilibrium. A feature of the simple, first-order model assumed in this section is that this percentage remains comstant with varying assumed rates of ingress, which is not the case in the following section.

Figure 5.2 shows the effect of changing purification flow at a constant ingress rate of 0.01 g/sec. Note that inhibitors, H_2 and CO, diminish in level as well as oxidant with increasing purification rate. Hence, it is not possible to categorically state that modest increases in purification flow will always tend to protect the core posts from steam corrosion.

5.3 Impurity Concentrations Using TIMOX

TIMOX is a program used to compute transient and steady state values of H_2O, H_2, and CO concentrations which result from assumed, steady rates of steam ingress into the primary system. The general features of the program are illustrated in Fig. 5.4. Initially, concentrations of H_2O, H_2, and CO are set to zero, at which time a steady steam ingress rate of W (mol/sec) is assumed to begin. The incoming steam mixes thoroughly with the primary system coolant and reacts with the core graphite in each zone at a rate specified by the assumed kinetics equation, the exposed surface area of the zone, and its characteristic temperature. The products of corrosion are also assumed to be well mixed and removed with H_2O in the purification flow, Q_p. The new concentrations of H_2O and H_2 or CO at the lapse of a time increment δt are determined from

$$[H_2O]_{i+1} = [H_2O]_i + \left(\frac{W-R-Q_p[H_2O]_i}{V}\right)\delta t \ , \tag{18}$$

$$[H_2]_{i+1} = [H_2]_i + \left(\frac{R-Q_p[H_2]_i}{V}\right)\delta t \ , \tag{19}$$

where R is the total reaction rate computed for the four zones, and V is the primary system volume. Concentration changes of H_2O, H_2, and CO are influenced by the steam ingress flow, varying reaction rate with the

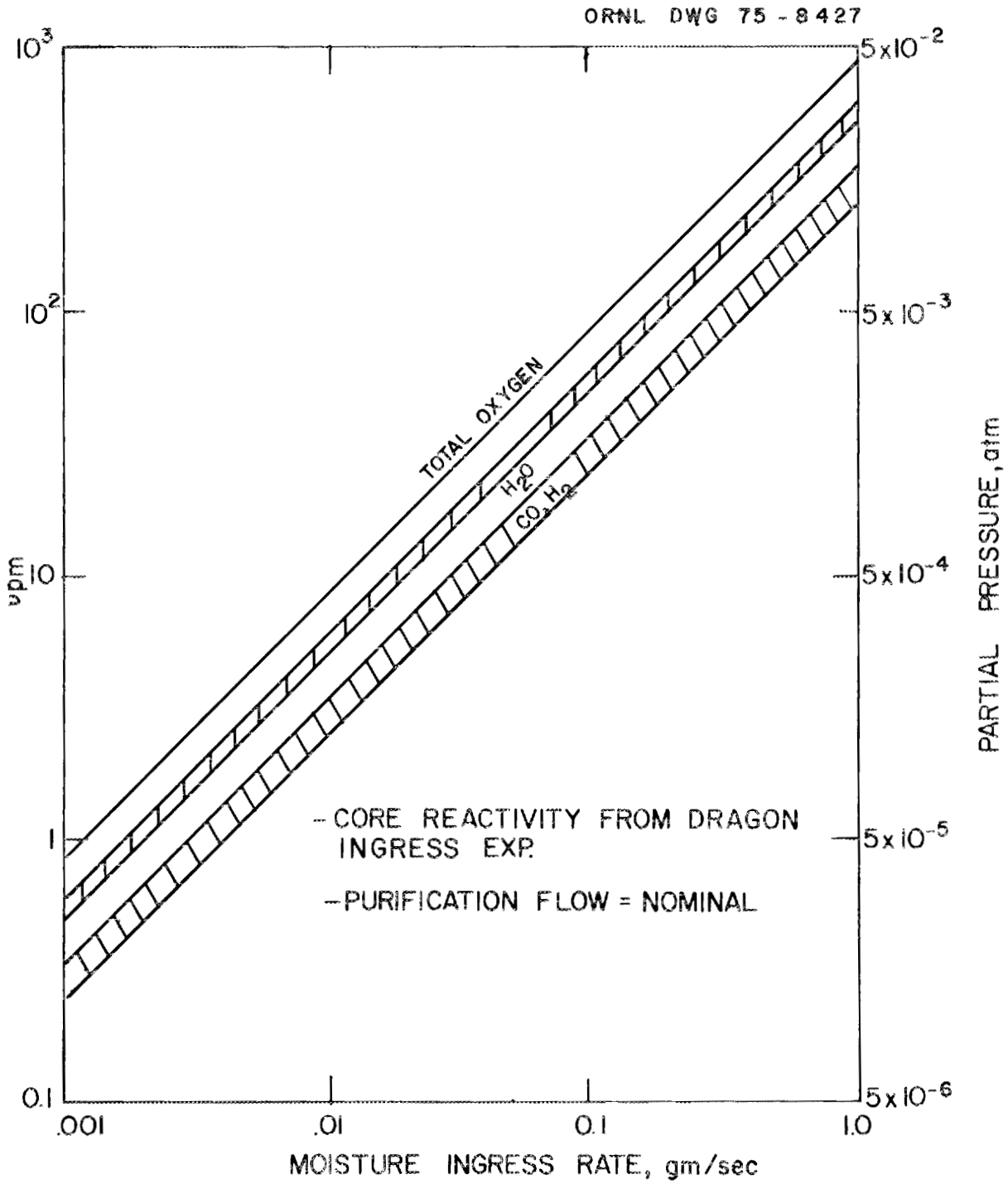

Fig. 5.2. Impurity levels vs H_2O ingress rate.

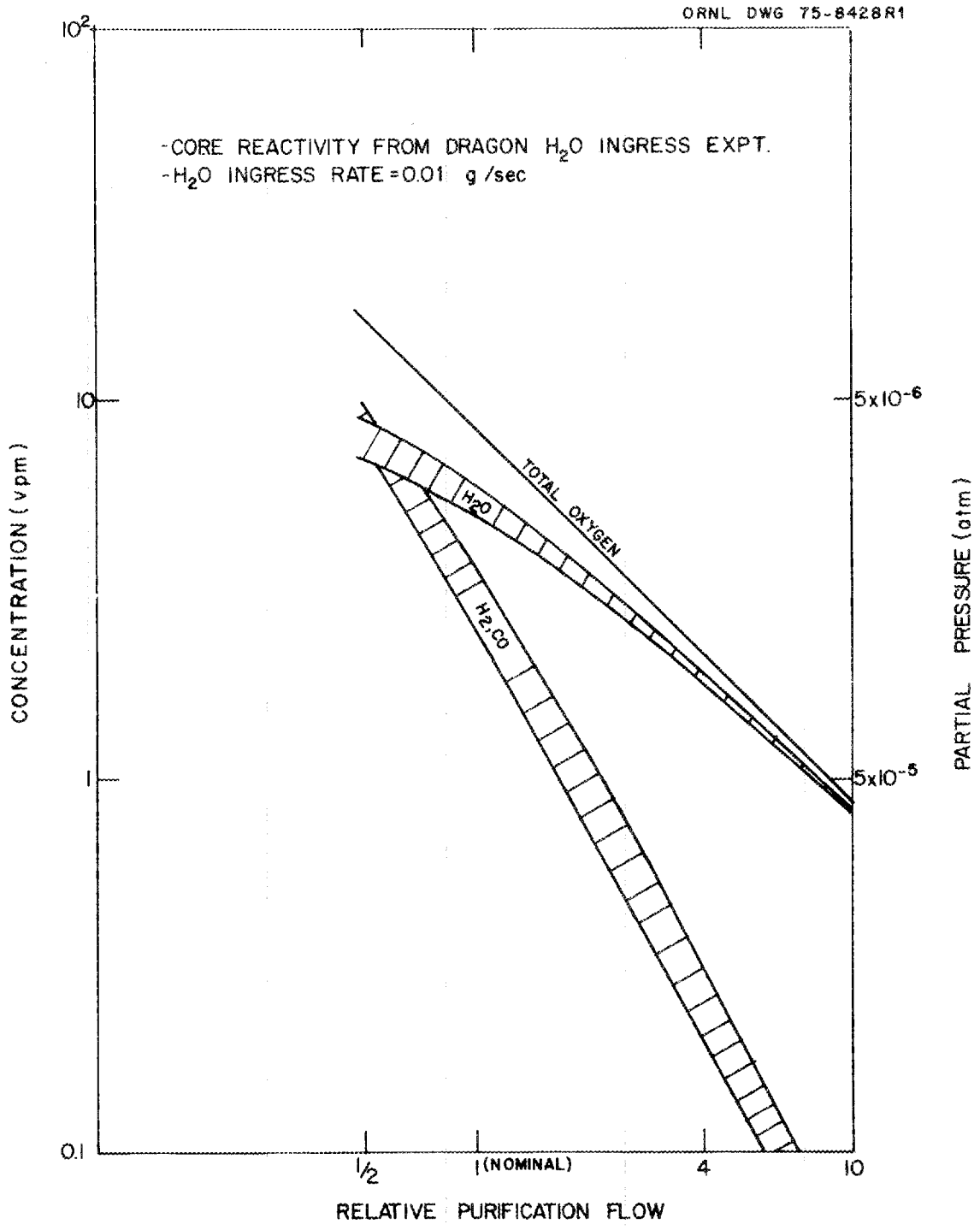

Fig. 5.3. Impurity level vs purification flow.

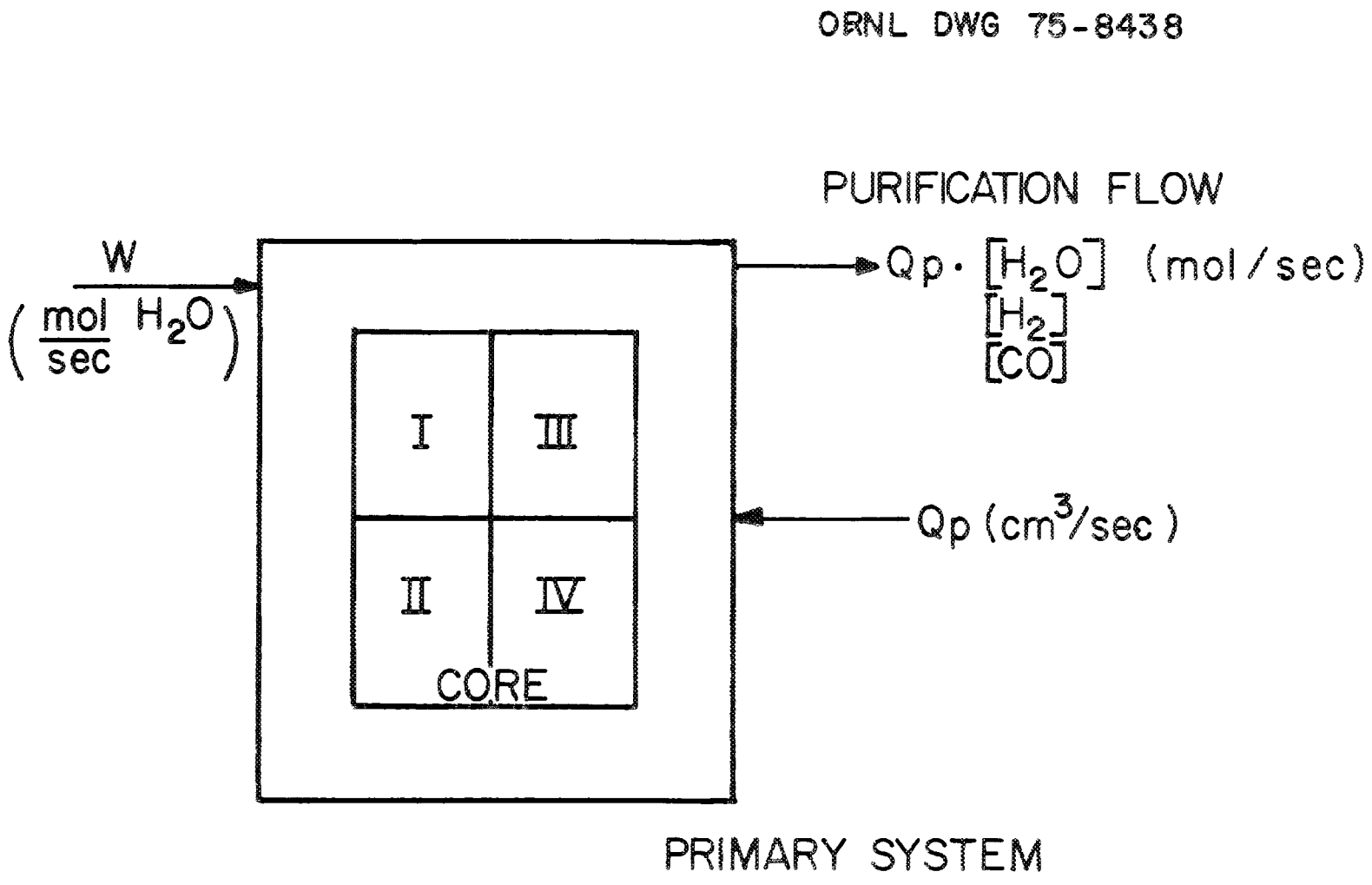

Fig. 5.4. Schematic diagram of TIMOX.

graphite, and varying removal rate with the purification flow. When both the H_2O and total oxygen gains and losses differ by less than 0.1%, the program is terminated and the steady state values are printed.

The transient concentrations, reaction rates, and removal rates with the purification flow of H_2O, CO, and H_2 are stored and may be plotted as time if desired.

5.3.1 Primary system parameters used in TIMOX

Primary system parameters used are those given in Table 1.1 describing the reference reactor assumed for this study.

Pressure correction for the corrosion rate expressions. The program may be run with any presumed corrosion rate equation modified to yield a rate in terms of moles per exposed surface area per unit time. There may be simultaneous input for three such expressions, and the three cases are carried along in parallel. Present results are based on the Wicke, OXIDE-3, and Giberson rate expressions, given in Eqs. (15), (17), and (18), in Sect. 4.2, each adjusted to account for the high pressure HTGR environment relative to the 1 atm conditions on which these expressions are based. The commonly accepted form of this pressure correction is an inverse dependence on the square root of the total pressure; that is, HTGR primary system corrosion rates are expected to be about a factor of 7 lower than predicted by correlations based on 1 atm.

A number of review articles (e.g., ref. 3) describe the highly idealized model of graphite corrosion which leads to an inverse square root dependency on pressure. To arrive at this result, it is assumed that the distribution of H_2O within the graphite is governed by an effective diffusion coefficient for H_2O, and a volumetric loss rate to the corrosion reaction proportional to the H_2O concentration. These two assumptions lead to

$$R_s\left(\frac{\text{mol}}{\text{cm}^2\text{-hr}}\right) = \sim \sqrt{D_{\text{eff}}} \quad . \tag{20}$$

One then further assumes that the oxidant is transported via diffusion in the graphite void spaces, and employs the theoretical prediction that gas

phase diffusivity varies inversely with total pressure. This leads to the stated result,

$$R_s\left(\frac{\text{mol}}{\text{cm}^2\text{-hr}}\right) = \sim \frac{1}{\sqrt{P_T}} \quad . \tag{21}$$

In view of this simplified picture, perhaps it is surprising that observed corrosion rates do vary with total pressure almost as indicated above. This treatment not only drastically simplifies the observed non-linear dependency of rate with oxidant concentration, but also ignores inhibition effects of CO and H_2, transport of CO and H_2, and adsorptivity effects of reactant and products on graphite. Nevertheless, data exist which conform closely to the inverse square-root relationship; for example, Ashworth et al.[12] state that results of one particular series of experiments conducted at 900°C were correlated by

$$R_s = \sim P_T^{-0.62} \quad . \tag{22}$$

This result is quite close to the highly theoretical Eq. (21); nevertheless, significant errors are introduced when attempting to extrapolate predictions from 1 atm test data. For example, using Eq. (21) to extrapolate from 1 atm to 49 atm leads to a corrosion rate which is 59% higher than an extrapolation based on Eq. (22).

Thus, TIMOX employs a pressure correction which probably tends to overestimate corrosion rates when extrapolating upward in pressure. However, since this correction was also applied to the estimated core support-post rate of corrosion, errors thereby introduced would tend to concel each other. That is, a high estimate for the core graphite corrosion rate would yield a low-side value for the oxidant level, which in turn tends to be compensated by the corresponding high estimated core post corrosion rate.

The next sections describe the method of arriving at the characteristic temperatures for each of the four core zones.

Core graphite and coolant temperatures. The core temperatures used in this study were computed using the OXIDE-3 program for the 2000 MW(t) case. OXIDE-3 divides the core into 20 temperature regions, each of

which are made up of 10 fuel element rows. Thus a total of 200 temperatures specify the core temperature distribution. These 200 OXIDE-3 core zones are combined in TIMOX into four zones. The relationships between the TIMOX, OXIDE-3, and HTGR fueling zones are summarized in Table 5.7.

Three representative temperatures for each of the 200 OXIDE-3 locations are listed in Table 5.8. The top temperature of each group refers to the coolant, and the bottom value refers to the average temperature of the combined graphite and fuel stick material. These two values were taken from Barsell.[13] The middle temperature of each set of three values in Table 5.7 represents the average graphite surface temperature at each indicated location, computed by using intraregion temperature distributions.[14] Graphite surface temperature is here defined as the temperature representative of the radial sections 2 and 3, referring to Fig. 5.5, which shows the cross-sectional detail used within OXIDE-3 to compute region average temperatures.[13] Sections 2-13 represent the graphite moderator between the fuel (shown as sections 14-17) and the coolant channel, represented by section 1.

From temperature distributions computed in ref. 14, it can be shown that the difference between the graphite surface temperature and the coolant temperature at that location is approximately 0.662 times the difference between the average graphite plus fuel stick temperature and the coolant; that is,

$$T_{surf} - T_{cool} = 0.662\ (T_{av\ "graph"} - T_{cool}) \quad . \tag{23}$$

Since the OXIDE-3 program listings include $T_{av\ "graph"}$ and T_{cool}, the graphite surface temperature may be calculated from Eq. (23).

Reaction-average region temperatures. Since the steam-graphite reaction is strongly temperature dependent — a 30°C temperature change alters the reaction rate by about a factor of 2 at 800°C — the question arises as to how to determine the appropriate characteristic temperature for each of the four TIMOX zones. A flat, space average will yield too low a value since the higher temperature regions, where a disproportionate part of the total reaction takes place, must be given added weight.

Table 5.7. Relation between TIMOX and OXIDE-3 regions and 2000 MW(t) HTGR refueling zones

TIMOX region	OXIDE-3 region	2000 MW(t) HTGR refueling zones
	1	3, 6 (without hottest column)
I	2	3, 6 (hottest column)
(Rows 1-5)	3	25, 34
	4	13, 19
II	5	21, 30
(Rows 6-10)	6	23, 32
	7	42, 48
	8	50, 53
	9	4, 7, 9, 15
	10	11, 17
	11	2, 5
III	12	1, 43, 49
(Rows 1-5)	13	26, 28, 35, 37
	14	24, 33
IV	15	20, 29
(Rows 6-10)	16	22, 27, 31, 36
	17	10, 16, 39, 41, 45, 47
	18	8, 12, 14, 18
	19	40, 46, 52, 55
	20	38, 44, 51, 54

Table 5.8. Core coolant, graphite surface, and graphite average temperature (top, middle, and bottom numbers, respectively) for the 20 OXIDE-3 regions and 10 fuel elements rows

OXIDE-3 region	OXIDE-3 region temps (°C)									
1	338.0	367.8	425.7	486.2	548.2	606.0	658.9	708.8	749.5	764.9
1	338.0	525.4	592.6	655.9	719.5	752.3	799.0	837.5	840.8	764.6
1	338.0	605.9	677.9	742.5	807.0	836.9	870.5	903.3	887.4	764.4
2	338.0	373.9	444.3	518.9	595.9	668.4	735.0	798.2	850.2	872.2
2	338.0	569.6	652.5	731.1	810.5	852.3	911.2	960.3	966.1	874.4
2	338.0	669.4	758.8	839.4	920.0	946.2	1001.2	1043.0	1025.3	875.5
3	338.0	369.0	429.3	492.7	557.5	618.3	673.8	726.3	769.2	786.0
3	338.0	532.3	602.5	668.7	735.4	770.2	819.4	860.1	864.2	786.0
3	338.0	615.7	690.9	758.6	826.3	847.8	893.7	928.4	912.8	786.0
4	338.0	369.0	429.3	492.5	557.4	618.2	673.7	726.2	769.0	785.5
4	338.0	531.7	601.8	668.0	734.7	769.5	818.7	859.4	863.7	785.5
4	338.0	614.8	689.9	757.5	825.2	846.8	892.7	927.4	912.0	785.5
5	338.0	369.1	429.5	492.9	557.9	618.7	674.4	726.9	769.9	786.6
5	338.0	531.5	601.7	668.0	734.8	769.8	819.1	859.9	864.4	786.6
5	338.0	614.4	689.6	757.4	825.1	846.9	892.9	927.8	912.7	786.6
6	338.0	369.0	429.3	492.6	557.5	618.3	673.8	726.3	769.2	786.0
6	338.0	528.1	598.0	664.1	730.8	766.3	815.5	856.5	861.7	786.0
6	338.0	609.4	684.2	751.7	819.3	841.8	887.9	923.0	909.0	786.0
7	338.0	369.0	429.3	492.5	557.3	618.0	673.4	725.9	768.7	785.5
7	338.0	520.9	590.3	656.2	722,7	759.2	808.7	850.2	857.0	785.5
7	338.0	598.5	672.5	739.8	807.2	831.3	877.8	913.6	902.1	785.5
8	338.0	369.0	429.3	492.5	557.3	617.9	673.4	725.8	768.5	784.9
8	338.0	517.1	586.3	652.1	718.5	755.6	805.2	846.9	854.6	784.9
8	338.0	592.7	666.4	733.5	800.8	825.8	872.5	908.7	898.5	784.9
9	338.0	369.3	429.7	493.0	558.0	618.8	674.4	727.0	769.9	786.6
9	338.0	495.2	563.1	628.6	694.9	735.7	786.3	829.7	842.9	786.6
9	338.0	559.4	631.2	697.8	764.8	795.3	843.4	882.2	880.2	786.6
10	338.0	369.3	429.5	492.8	557.8	618.4	674.0	726.5	769.3	786.0
10	338.0	495.7	563.5	629.0	695.2	735.8	786.3	829.7	842.6	786.0
10	338.0	560.2	631.9	698.5	765.4	795.7	843.7	882.3	880.0	786.0
11	338.0	369.2	429.4	492.6	557.4	618.0	673.4	725.8	768.5	784.9
11	338.0	494.3	561.9	627.2	693.3	734.0	784.5	827.8	841.0	784.9
11	338.0	558.1	629.6	696.0	762.8	793.3	841.2	879.9	878.0	784.9
12	338.0	369.3	429.5	492.8	557.7	618.3	673.8	726.2	768.9	785.2
12	338.0	486.9	554.2	619.4	685.5	727.4	778.2	822.1	837.1	785.3
12	338.0	547.0	617.8	684.0	750.7	783.0	831.5	871.0	871.9	785.4
13	338.0	369.3	429.7	493.0	557.9	618.7	674.2	726.7	769.5	786.0
13	338.0	488.6	556.1	621.4	687.6	729.3	780.1	824.0	838.7	786.0
13	338.0	549.5	620.6	687.0	753.8	785.8	834.2	873.7	874.0	786.0
14	338.0	369.2	429.4	492.6	557.4	618.0	673.4	725.8	768.5	784.9
14	338.0	490.5	558.0	623.2	689.2	730.5	781.1	824.7	838.8	784.9
14	338.0	552.4	623.6	689.9	756.5	787.9	836.1	875.2	874.7	784.9
15	338.0	369.2	429.4	492.5	557.3	617.8	673.2	725.4	768.1	784.5
15	338.0	486.2	553.3	618.4	684.3	726.2	776.9	820.8	835.8	784.5
15	338.0	545.9	616.5	682.7	749.2	781.5	829.9	869.4	870.4	784.5
16	338.0	369.2	429.4	492.5	557.2	617.7	673.0	725.4	768.0	784.4
16	338.0	489.8	557.1	622.3	688.3	729.6	780.1	823.7	837.9	784.4
16	338.0	551.4	622.4	688.6	755.2	786.7	834.8	873.9	873.6	784.4
17	338.0	369.2	429.3	492.4	557.0	617.5	672.8	725.0	767.7	784.0
17	338.0	483.7	550.6	615.5	681.4	723.6	774.3	818.3	833.9	784.0
17	338.0	542.1	612.5	678.4	744.8	777.8	826.2	865.9	867.7	784.0
18	338.0	369.3	429.6	492.8	557.7	618.3	673.8	726.2	768.9	785.3
18	338.0	483.0	550.0	615.2	681.2	723.7	774.6	818.8	834.7	785.3
18	338.0	541.1	611.5	677.7	744.2	777.5	826.1	866.1	868.3	785.3
19	338.0	369.3	429.6	492.8	557.7	618.3	673.8	726.2	768.9	785.3
19	338.0	483.2	550.2	615.3	681.3	723.8	774.7	818.9	834.8	785.3
19	338.0	541.3	611.8	677.9	744.4	777.7	826.3	866.3	868.4	785.3
20	338.0	369.3	429.5	492.7	557.5	618.0	673.5	725.9	768.5	784.9
20	338.0	482.4	549.3	614.4	680.3	722.9	773.8	818.0	834.0	784.9
20	338.0	540.1	610.5	676.5	743.0	776.4	825.0	865.0	867.4	784.9

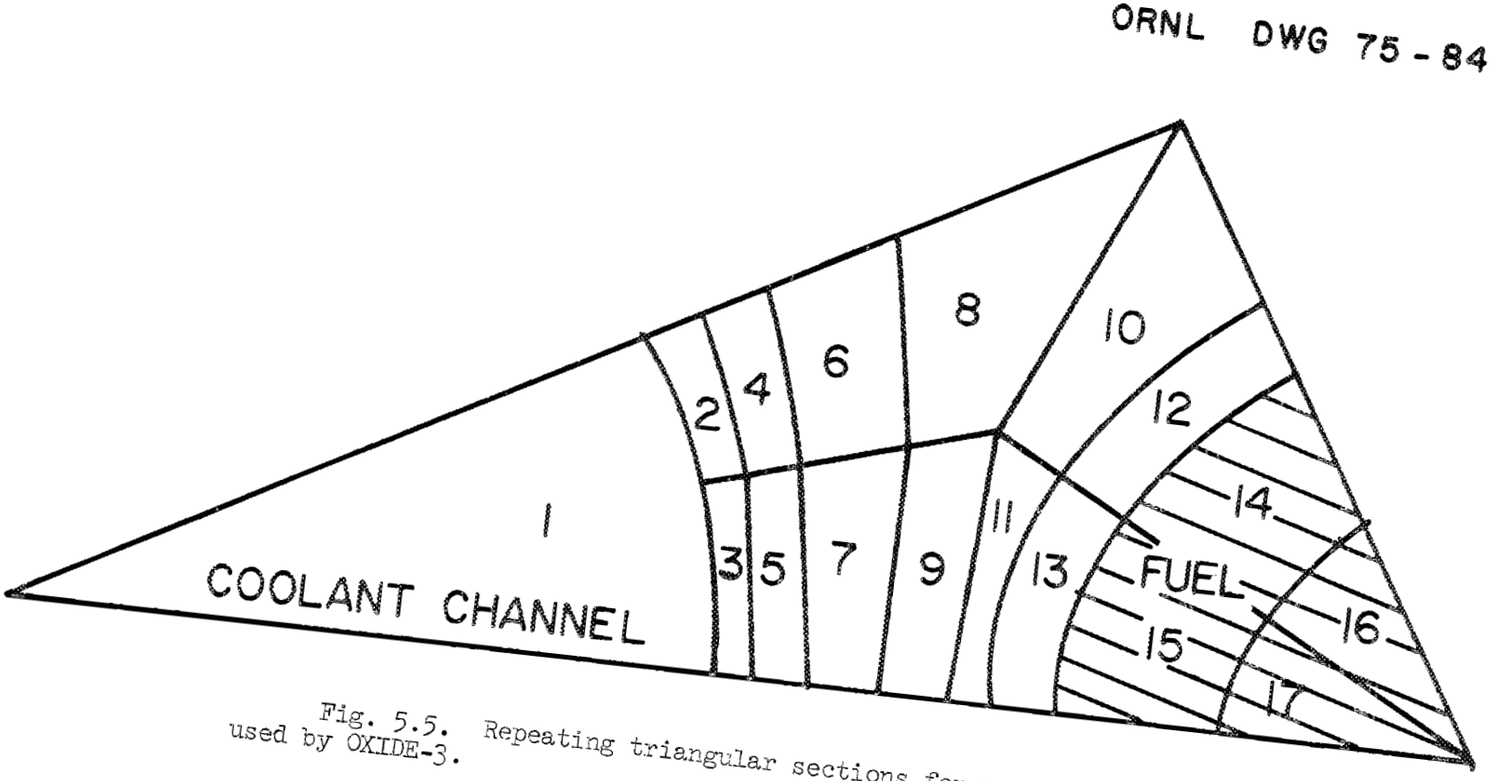

Fig. 5.5. Repeating triangular sections for numerical analysis used by OXIDE-3.

Another problem is whether the OXIDE-3 region temperatures given in Table 5.8 appropriately characterize the smaller OXIDE-3 regions when considering a highly temperature-dependent process (i.e., a thermally activated corrosion rate). The given temperatures are flat averages over regions ranging in size from ~ 1 to ~ 3 m^3 (except region 2, which is much smaller) within which substantial temperature variation may exist.

The appropriate region-average temperature, $\bar{T}_A$, of a total region, A_T, in which the average corrosion rate is $R_T(\bar{T}_A)$ mol/cm^2-sec, may be determined by noting

$$A_T \, R_T(\bar{T}_A) = \sum_i R_i(T_i) \cdot A_i \quad , \tag{24}$$

where the subscript i refers to the subregions comprising A_T, each of which are sufficiently small (or sufficiently uniform in temperature) to be characterized by a single temperature, T_i. Since

$$R(T_i) = \sim \exp\left(-\frac{\Delta H}{RT_i}\right) \tag{25}$$

appropriately describes the variation of reaction rate with temperature throughout regions where H_2O, H_2, and CO levels are approximately equal, substituting Eq. (25) into Eq. (24) and solving for $\bar{T}_A$ gives

$$\bar{T}_A = \frac{-\left(\frac{\Delta H}{R}\right)}{\ln\left[\sum_{i=1}^{N} \exp\left(\frac{-\Delta H}{RT_i}\right)\left(\frac{A_i}{A_T}\right)\right]} \, . \tag{26}$$

Equation (26) shows that the reaction-average temperature of a region comprised of N subregions of more-or-less uniform temperature, T_i, depends on the activation energy for the reaction, ΔH.

The validity of using the region-average temperature specified by OXIDE-3 to characterize the corrosion rate within that region was tested using detailed intraregional temperature distributions available for the Fort St. Vrain Reactor (FSV).[15] The detail of these data is such that 56 temperature values are given within each fueling zone; hence, a minimum of 112 values for each OXIDE-3 region are available. The results for six

selected locations within the FSV reactor and times after startup are shown in Table 5.9. Note that the reaction-rate average temperature exceeds the flat space-average by an average of 3.7°C when the activation energy is assumed to be 40,000 cal/mol, and 6.4 when $\Delta H = 67,000$. Since a temperature increment of 10°C represents about a 25% change in reaction rate, use of flat, region-average temperatures given by OXIDE-3 should be correct for specifying the corrosion rate in the region to within 25% of the true value.

TIMOX region-average temperatures. The reaction-rate average temperature for each of the four TIMOX zones were computed by applying Eq. (26) to the surface temperatures within the region given in Table 5.8. The fractional areas, A_i/A_T, of each OXIDE-3 zone are listed in Table 5.10. The results showing the comparison of the reaction-rate average temperature with the flat average for each of the four TIMOX zones are given in Table 5.11. In the next section, calculations for primary loop impurity levels were based on the higher average region temperatures where the activation energy of 68,000 cal/mol was assumed.

5.3.2 Impurity levels in the primary system for steady steam ingress using TIMOX

Equilibrium impurity levels. Predicted concentrations of H_2O, H_2, and CO under various assumed steady-steam ingress conditions are listed in Tables 5.12-5.14, and are plotted in Figs. 5.6-5.10. Three sequences of runs are presented. Table 5.12 and Figs. 5.6 and 5.7 illustrate the effect of varying steam ingress rates at the nominal purification flow. Ingress rates of 0.001 to 1.0 g/sec are assumed in steps of a factor of 10. It should be noted that an ingress rate of 0.0116 g/sec (0.09 lb_m/hr) is the maximum acceptable steady rate of steam ingress presumed in the Delmarva PSAR.[16]

At the lowest assumed inleakage rate of 0.001 g/sec, the range of predicted H_2O concentration is 0.14 to 0.63 vpm, about a factor of 5, depending on whether the Wicke, OXIDE-3, or Giberson kinetic equation is used to determine the core reactivity. At higher inleakage rates, differences

Table 5.9. Comparison of region-average and reaction-rate average temperatures, Eq. (25), for OXIDE-3 specified regions, using FSV reactor temperature distributions

Location in FSV reactor, and time after startup	Region-average surface temperature (°C)	Reaction-rate average temperature; increment over region-average ΔH (cal/mole) 40,000 (°C)	68,000 (°C)
1. Region 1; cols. 1, 3; Z[a] = 28-34 m, T[b] = 0 days	889.4	+ 6.2	+ 10.6
2. Region 1; cols. 1, 3; Z = 28-34 m, T = 310 days	850.8	+ 2.2	+ 3.8
3. Region 1; cols. 1, 3; Z = 35-41 m, T = 0 days	907.1	+ 5.9	+ 10.1
4. Region 1; cols. 1, 3; Z = 35-41 m, T = 310 days	888.4	+ 0.8	+ 1.5
5. Region 7; cols. 1-7; Z = 24-31 m, T = 310 days	764.1	+ 5.0	+ 8.6
6. Region 7; cols. 1-7; Z = 41-48 m, T = 310 days	856.3	+ 2.3	+ 4.0
	Average	+ 3.7	+ 6.4

[a]Distance from top of active core.

[b]Time after startup of new core.

Table 5.10. Fractional areas, A_i/A_T, for computing reaction-average temperature from Eq. (26)

OXIDE 3 region number	Fuel element rows 1 . 2 . 3 . 4 . 5	6 . 7 . 8 . 9 . 10 .
1	0.01714	0.01714
2	0.00286	0.00286
3	0.02	0.02
4	↓	↓
5	TIMOX region I	TIMOX region III
6		
7		
8		
9	0.04	0.04
10	0.02	0.02
11	0.01143	0.01143
12	0.01714	0.01714
13	0.02286	0.02286
14	0.01143 – TIMOX	0.01143 – TIMOX
15	0.01143 – region II	0.01143 – region IV
16	0.02229	0.02229
17	0.03429	0.03429
18	0.02286	0.02286
19	↓	↓
20		

Table 5.11. Reaction-rate average temperature for each TIMOX region

TIMOX region	Flat, area-average temperature (°C)	Reaction-rate average temperature	
		$\Delta H = 68,000$ (°C)	$\Delta H = 40,000$ (°C)
1	563.1	685.2	660.7
2	810.2	833.1	822.9
3	537.5	645.2	625.4
4	791.2	805.8	799.7

Table 5.12. Impurity levels in the primary system for steady steam ingress rates computed using TIMOX. Steam leak series, nominal purification flow

Case		Steam inleakage (g/sec)	Purification rate	Impurity levels P_{H_2O} (atm)	P_{H_2O} (vpm)	P_{H_2}, P_{CO} (atm)	P_{H_2}, P_{CO} (vpm)	Fraction H_2O to purification	Total reaction rate $\left(\frac{mol}{sec}\right)$
1.	W[a]	0.001	nominal	1.4 E-5	0.29	3.4 E-5	0.29	0.30	3.9 E-5
	O[b]	↓	↓	6.7 E-6	0.14	4.1 E-5	0.84	0.14	4.8 E-5
	G[c]	↓	↓	3.1 E-5	0.63	1.7 E-5	0.35	0.65	1.9 E-5
2.	W	0.0114	nominal	2.6 E-4	5.3	2.9 E-4	5.9	0.47	3.3 E-4
	O	↓	↓	2.4 E-4	4.9	3.1 E-4	6.3	0.43	3.6 E-4
	G	↓	↓	4.4 E-4	9.0	1.1 E-4	2.2	0.80	1.3 E-4
3.	W	0.1	nominal	3.5 E-3	71.0	1.3 E-3	27.0	0.73	1.5 E-3
	O	↓	↓	3.7 E-3	76.0	1.1 E-3	22.0	0.78	1.2 E-3
	G	↓	↓	4.3 E-3	88.0	5.3 E-4	11.0	0.89	6.2 E-4
4.	W	1.0	nominal	4.3 E-2	880.0	4.8 E-3	98.0	0.90	5.6 E-3
	O	↓	↓	4.6 E-2	940.0	1.7 E-3	35.0	0.94	2.0 E-3
	G	↓	↓	4.5 E-2	920.0	2.6 E-3	53.0	0.94	3.1 E-3

[a]Assuming Wicke equation, Eq. (15), Sect. 4.2.

[b]Assuming OXIDE-3 rate equation, Eq. (17), Sect. 4.2.

[c]Assuming Giberson rate equation, Eq. (18), Sect. 4.2.

Table 5.13. Impurity levels in the primary system for steady steam ingress rates computed using TIMOX. Purification flow series

Case	Steam ingress rate (g/sec)	Purification rate	Impurity levels P_{H_2O} (atm)	P_{H_2O} (vpm)	P_{H_2}, P_{CO} (atm)	P_{H_2}, P_{CO} (vpm)	Fraction H_2O to purification	Total reaction rates $\left(\frac{mol}{sec}\right)$
1. W[a]	0.0114	1/2 x nominal	4.6 E-4	9.4	6.2 E-4	13.0	0.43	3.6 E-4
O[b]	↓	↓	4.3 E-4	8.8	6.6 E-4	14.0	0.40	3.8 E-4
G[c]	↓	↓	8.1 E-4	17.0	2.7 E-4	5.5	0.75	1.6 E-4
2. W	0.0114	nominal	2.6 E-4	5.3	2.9 E-4	5.9	0.47	3.3 E-4
O	↓	↓	2.4 E-4	4.9	3.1 E-4	6.3	0.43	3.6 E-4
G	↓	↓	4.4 E-4	9.0	1.1 E-4	2.2	0.80	1.3 E-4
3. W	0.0114	4 x nominal	8.8 E-5	1.8	4.8 E-5	1.0	0.65	2.2 E-4
O	↓	↓	6.9 E-5	1.4	6.7 E-5	1.4	0.50	3.1 E-4
G	↓	↓	1.2 E-4	2.4	1.6 E-5	0.33	0.88	7.4 E-5

[a]Assuming Wicke rate equation, Eq. (15), Sect. 4.2.

[b]Assuming OXIDE-3 rate equation, Eq. (17), Sect. 4.2.

[c]Assuming Giberson rate equation, Eq. (18), Sect. 4.2.

Table 5.14. Impurity levels in the primary system for steady steam ingress rates using TIMOX. Temperature level series; steam ingress rate = 0.0114 g/sec, purification flow = nominal

Case		General primary system temperature level	Impurity levels P_{H_2O} (atm)	P_{H_2O} (vpm)	P_{H_2}, P_{CO} (atm)	P_{H_2}, P_{CO} (vpm)	Fraction H_2O to purification flow	Total reaction rate (mol/sec)
1.	W[a]	nominal	2.6 E-4	5.3	2.9 E-4	5.9	0.47	3.3 E-4
	O[b]	↓	2.4 E-4	4.9	3.1 E-4	6.3	0.43	3.6 E-4
	G[c]	↓	4.4 E-4	9.0	1.1 E-4	2.2	0.80	1.3 E-4
2.	W	+ 50°C	1.0 E-4	2.0	4.4 E-4	9.0	0.19	5.1 E-4
	O	↓	9.5 E-5	1.9	4.5 E-4	9.0	0.18	5.2 E-4
	G	↓	2.8 E-4	5.7	2.6 E-4	5.5	0.51	3.1 E-4
3.	W	+ 100°C	2.2 E-5	0.45	5.2 E-4	11.0	0.040	6.0 E-4
	O	↓	2.4 E-5	0.49	5.1 E-4	10.0	0.044	6.0 E-4
	G	↓	1.1 E-4	2.2	4.3 E-4	8.8	0.2	5.0 E-4

[a]Assuming Wicke rate equation, Eq. (15), Sect. 4.2.

[b]Assuming OXIDE-3 rate equation, Eq. (17), Sect. 4.2.

[c]Assuming Giberson rate equation, Eq. (18), Sect. 4.2.

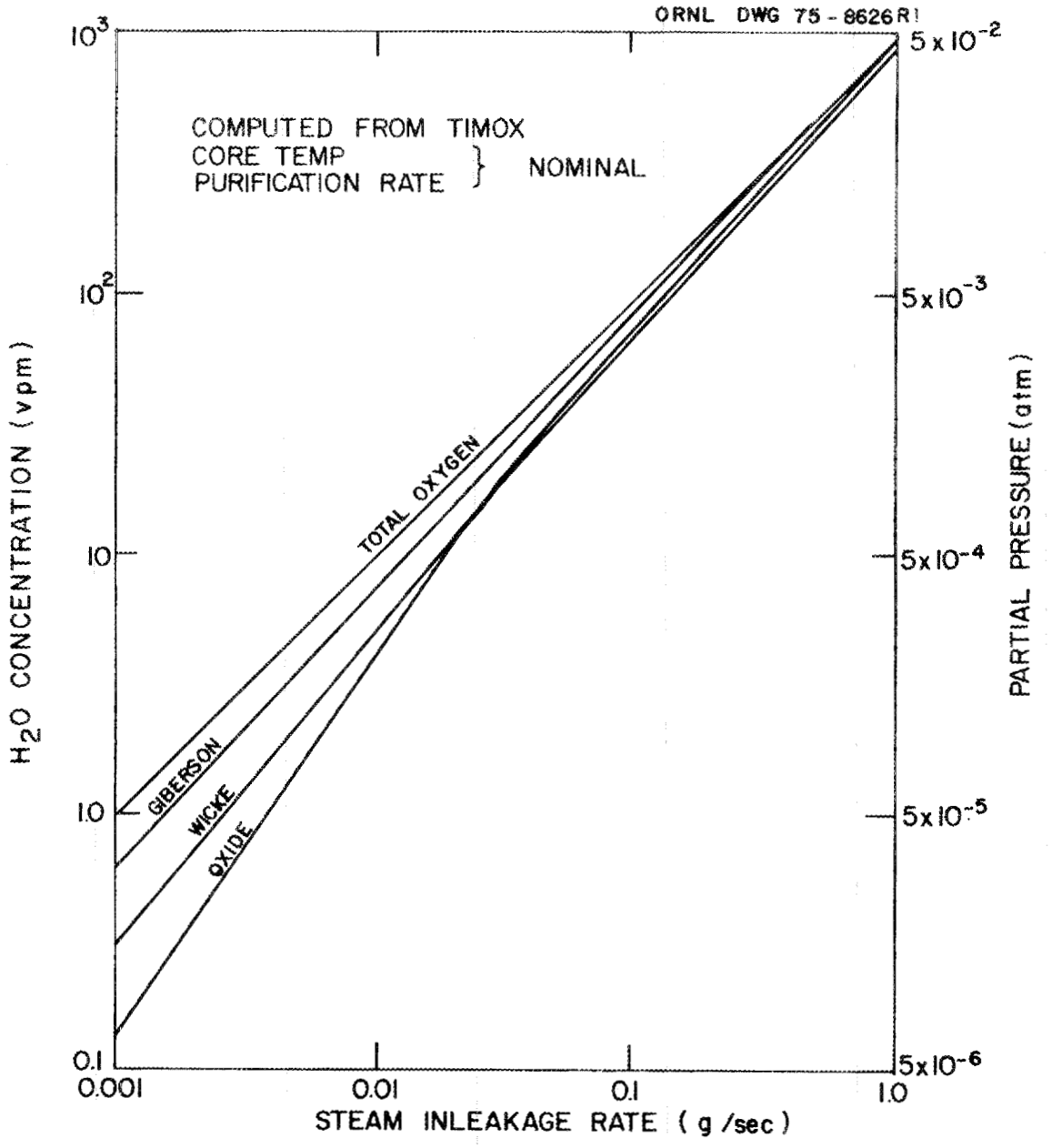

Fig. 5.6. Equilibrium H_2O concentration vs steam inleakage rate computed using TIMOX.

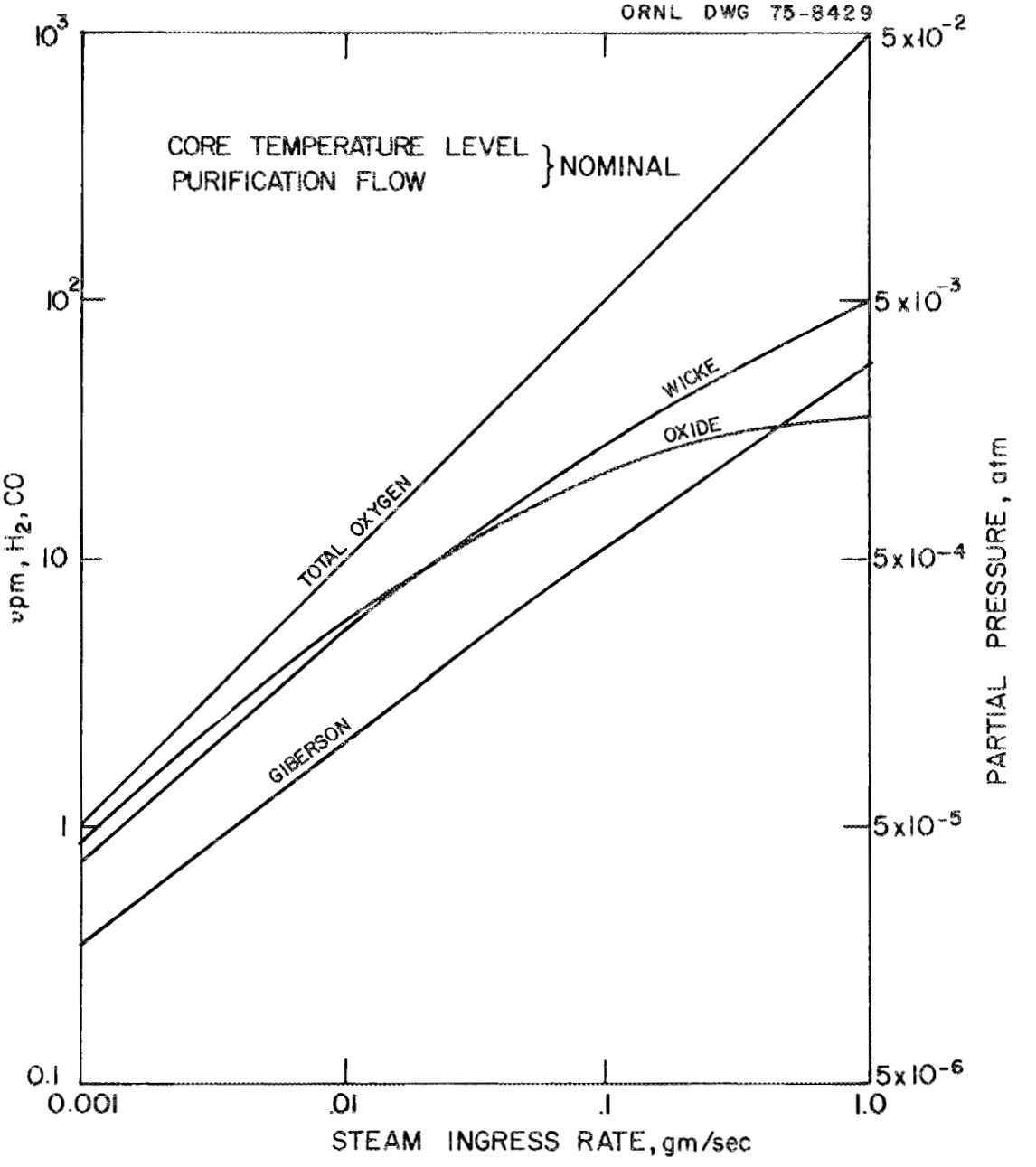

Fig. 5.7. Equilibrium H_2 and CO concentration vs steam inleakage rate computed using TIMOX.

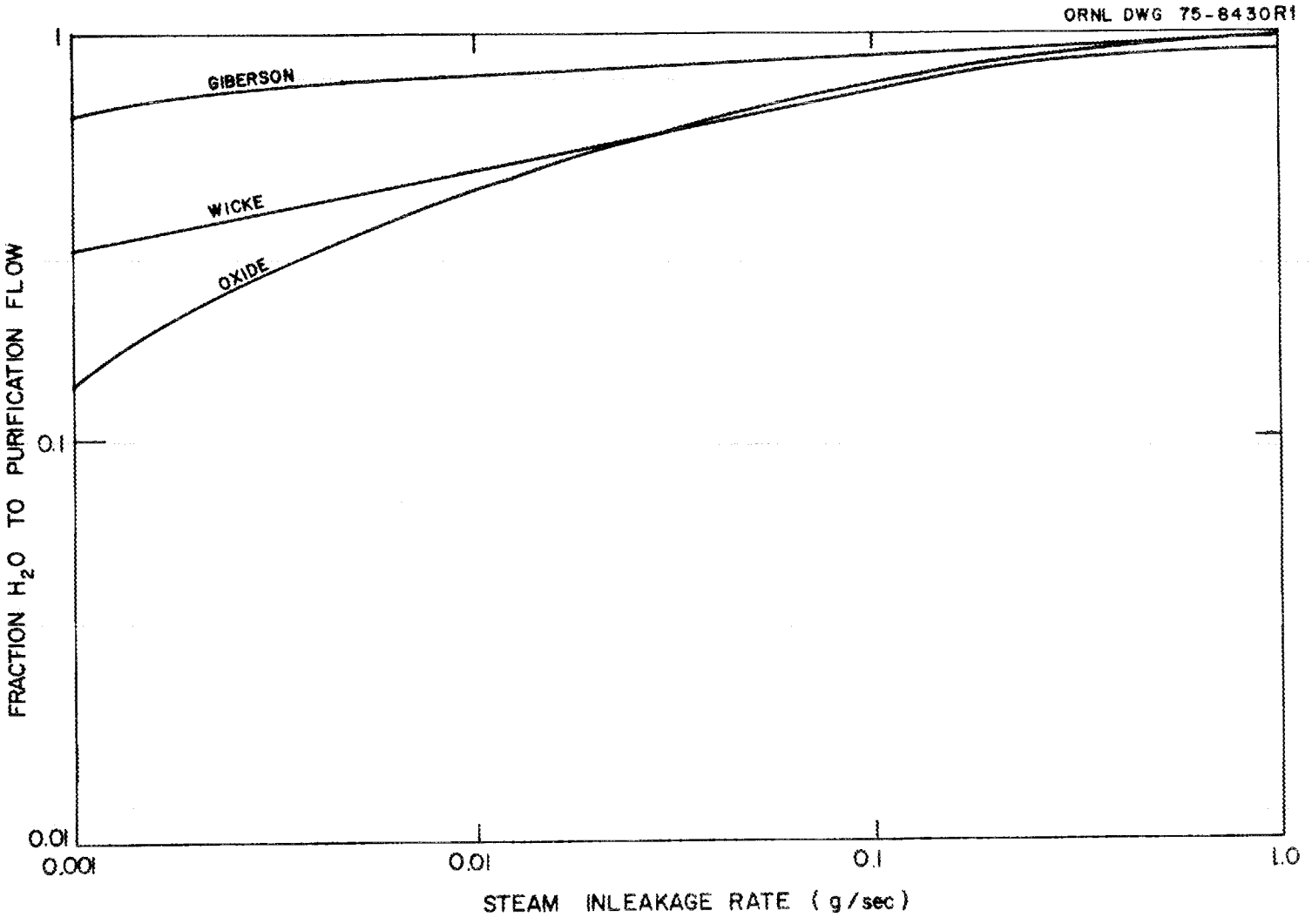

Fig. 5.8. Fraction H_2O to purification flow vs steam inleakage rate computed using TIMOX.[2]

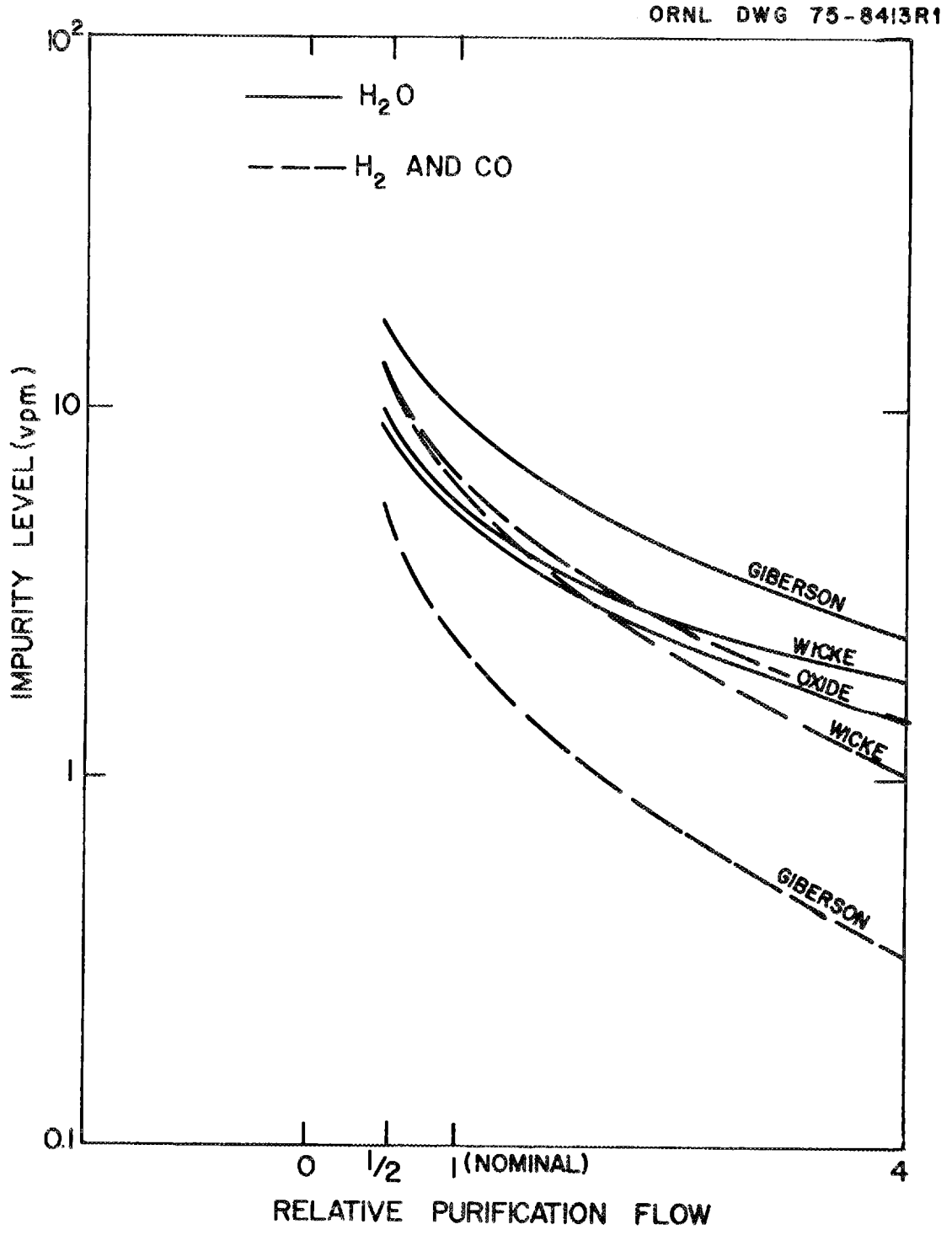

Fig. 5.9. Effect of purification rate on impurity levels. Steam inleakage rate = 0.001 g/sec, computed using TIMOX.

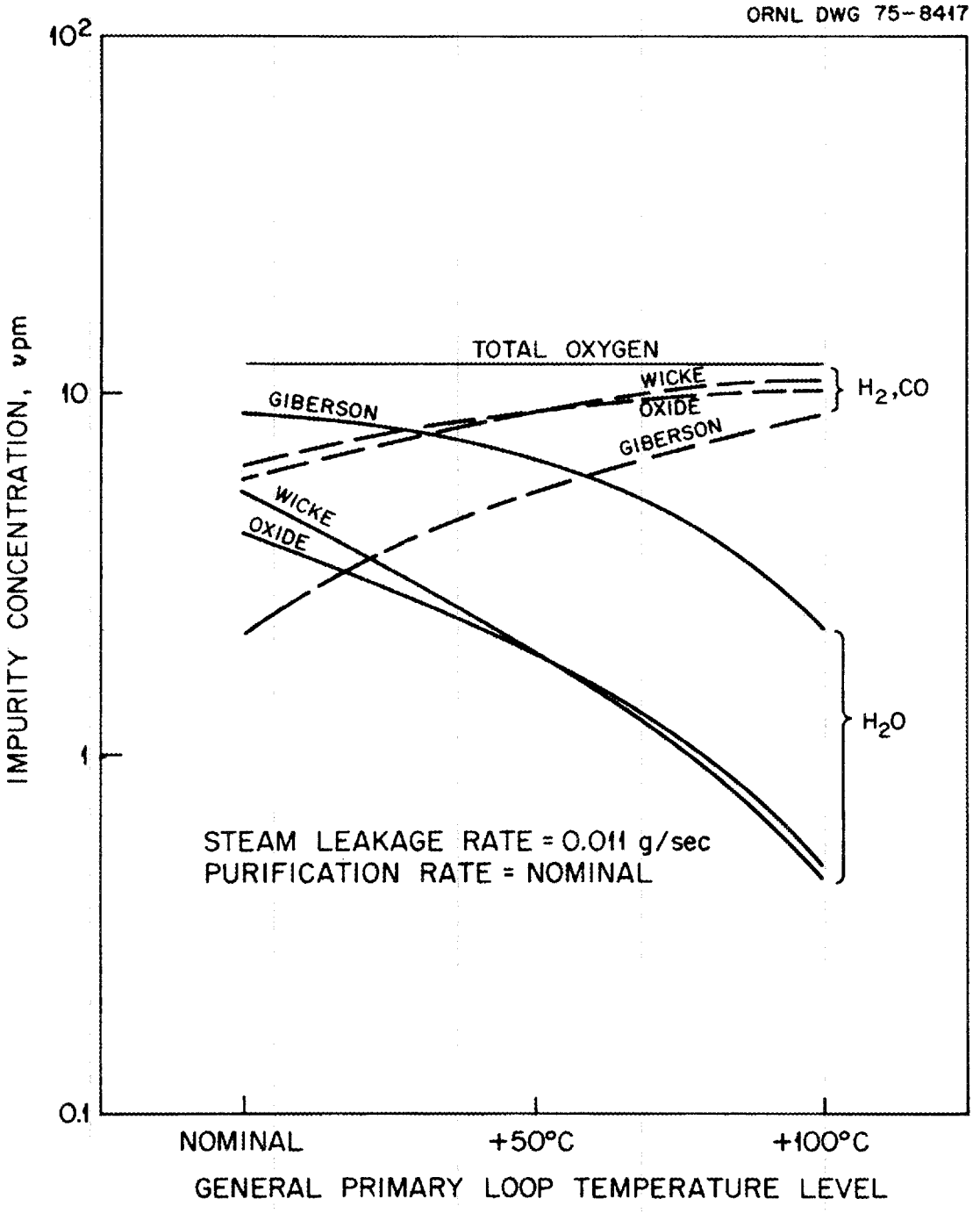

Fig. 5.10. Effect of general temperature level on impurity concentrations. Steam inleakage rate = 0.011 g/sec.

between predicted levels using the three rate equations diminishes as the fraction of H_2O captured by the purification flow increases.

In comparing impurity levels predicted using Dragon core reactivity data (shown in Fig. 5.2 and Table 5.5) with the TIMOX predictions, note that Dragon-derived reactivities predict about 65% of the total oxygen-bearing species in the primary system to be H_2O, independent of the assumed ingress rate. The TIMOX results show a variation of the $H_2O/\Sigma O$ ratio with steam ingress rate due to the nonlinearity of the kinetics equations used in TIMOX as opposed to the simple first-order kinetics used in interpretating the Dragon data. For an ingress rate of 0.001 g/sec, TIMOX predicts a range of 14 to 64% of the total oxygen to be H_2O. At an ingress rate of 0.0114 g/sec, the ratio rises to a range of 44 to 80%; at the higher ingress rate of 0.1 g/sec, from 72 to 90% of the oxygen exists as H_2O. Apparently, there is a reasonable agreement between the Dragon-based and TIMOX predictions in this regard.

Table 5.13 and Fig. 5.9 illustrate the effect of changing the purification rate from one-half to four times the nominal value for an assumed ingress rate of 0.0114 g/sec. These results are used in Sect. 6 to determine the effect of varying purification flow on the rate post corrosion. At this point, it is not obvious that a modest increase in purification flow is beneficial to core post corrosion, since reaction inhibitors as well as oxidant are reduced in concentration.

Table 5.14 and Fig. 5.10 show the effect of the general temperature level in the primary system on the impurity atmosphere. Cases 2 and 3 in Table 5.14 assume all core and coolant temperatures to be 50 and 100°C higher than the reference design, while assuming a nominal purification flow and an inleakage rate of 0.0114 g/sec. As expected, the H_2O levels drop with increasing primary loop temperature; that is, the core becomes a superior oxidant getter and, hence, more protective of the core posts. Counterbalancing this improved protection are the inherent increased core post corrosion rates for these higher temperatures. In Sect. 6, these opposing tendencies are weighed, and it is found that modest increases in primary system temperature level may have a net beneficial effect on core post corrosion in some cases.

Transient impurity levels computed using TIMOX. TIMOX computes the equilibrium impurity levels presented in the previous section by assuming an initially clean primary system and following the transient levels after the initiation of a steam leak to their steady state values. For the slow leak cases considered in this report, these transients are only of secondary interest, and are discussed briefly. Table 5.15 lists the durations involved following leak initiation until equilibrium levels are established. The times required to establish equilibrium are relatively independent of assumed kinetics equation and steam ingress rates, and run about 37 hr at the nominal purification flow. Equilibrium time is defined as the time to reach 99% of the ultimate concentration, a point conveniently noted by following the relative oxygen ingress and purification rates. The purification flow effects the equilibration time, and the general temperature level has less of an effect.

Table 5.15. Time to reach equilibrium[a] impurity levels following initiation of a slow steam leak. Computed from TIMOX

Steam ingress rate (g/sec)	Purification rate	Primary system temperature level	Equilibrium time (hr)
0.001	nominal	nominal	35
0.0114	↓	↓	37
0.1	↓	↓	37
1.0	↓	↓	37
0.0114	1/2 x nominal	nominal	74
↓	nominal	↓	37
↓	4 x nominal	↓	15
0.0114	nominal	nominal	37
↓	↓	+ 50°C	63
↓	↓	+ 100°C	63

[a]Defined as time to reach 99% of ultimate concentration.

An option of TIMOX is the capability to plot transient impurity levels and flows to the purification plant. Figures 5.11 and 5.12 illustrate one such optional plot for the case 0.0114 g/sec ingress flow, nominal purification rate, and assumed Wicke kinetics equations.

5.4 References for Section 5

1. Delmarva Power and Light Preliminary Safety Analysis Report, Table 5.3.1-1.
2. Delmarva Power and Light Preliminary Safety Analysis Report, Table 1.3-2.
3. P. L. Walker et al., "Gas Reactions of Carbon," in Advances in Catalysis, XI, Section V, Part C, Academic, 1959.
4. M. Carlyle and D. V. Kinsey, Results of the Injection of Impurities Into the Dragon Reactor Primary Coolant, D.P. Rep. 544 (June 1969).
5. T. J. Clark, R. E. Woodley, and D. R. Halas, "Gas-Graphite Systems," p. 149, in Nuclear Graphite, ed. by E. R. Nightingale, Academic, 1962.
6. E. Wicke et al., Corrosion Rate of Graphites by CO_2 and H_2O Vapor Taking Into Account In-Pore Diffusion and Temperature Gradients, D.P. Rep. 391, pp. 23-24 (January 1966).
7. R. C. Giberson and G. L. Tingey, Reaction of Gaseous Impurities in an HTGR, BNWL-974, pp. 6-7 (December 1968).
8. M. R. Everett, D. V. Kinsey, and E. Römberg, Carbon Transport Studies for HTGR's, D.P. Rep. 491, pp. 46-59 (November 1966).
9. E. Wicke et al., Corrosion Rate of Graphites by CO_2 and H_2O Vapor Taking Into Account In-Pore Diffusion and Temperature Gradients, D.P. Rep. 391, p. 21 (January 1966).
10. M. R. Everett, D. V. Kinsey, and E. Römberg, Carbon Transport Studies for HTGR's, D.P. Rep. 491, pp. 19-20 (November 1966).
11. Dragon High Temperature Reactor Project, First Annual Report 1959-1960 (July 1960). Appendix VI, Table II, pertaining to core with 37 Mark VII fuel elements.

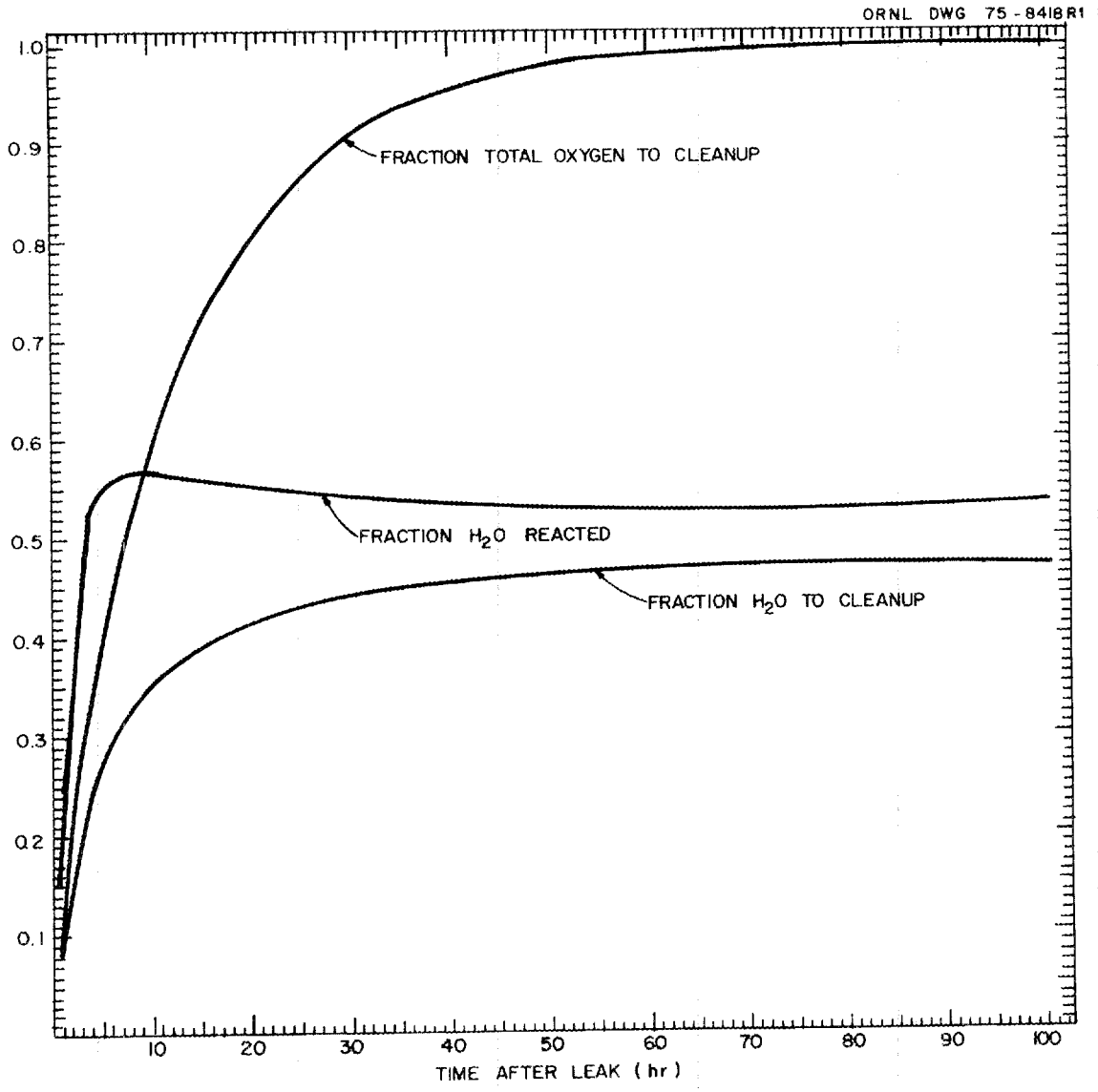

Fig. 5.11. Transient fractional purification and reaction rates relative to steam ingress rate.

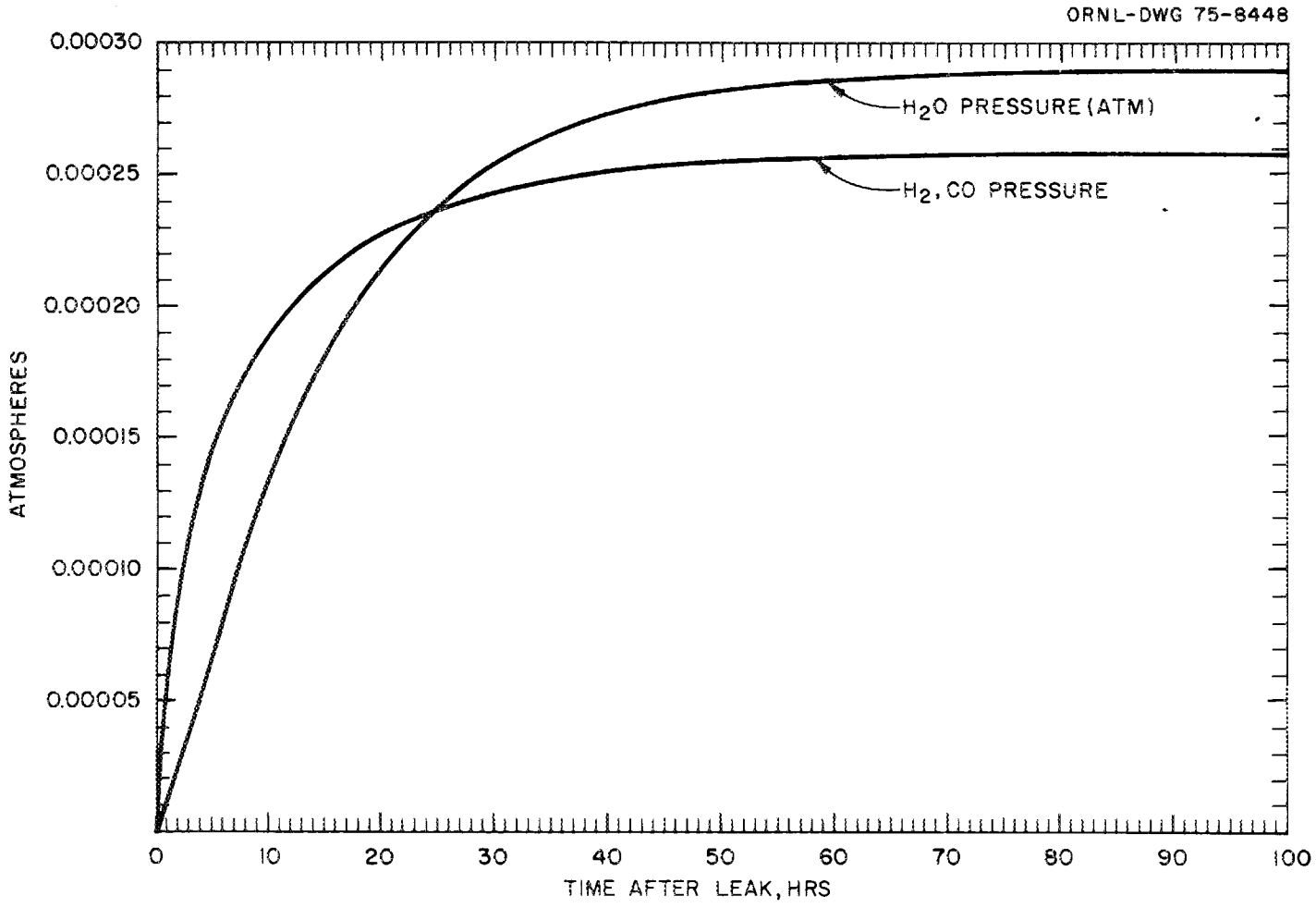

Fig. 5.12. Transient impurity levels. Ingress flow = 0.01 g/sec; purification rate = nominal.

12. F. P. O. Ashworth, J. Kirk, and H. J. de Nordwall, "Gas-Cooled Reactor Safety Technology," Internal Dragon Project memo.

13. A. W. Barsell and M. B. Peroomian, Consequences of Water Ingress Into the HTGR Primary Coolant, GA-A1371 (April 1975).

14. M. B. Peroomian, A. W. Barsell, and J. C. Saeger, OXIDE-3: A Computer Code for the Analysis of HTGR Steam or Air Ingress Accidents, Sect. 3.2.2 and 9, in GA-A12493, GA-LTR-7 (January 1974).

15. W. E. Thomas, ORNL Reactor Division, personal communication, Feburary 1975.

16. Delmarva Power and Light Preliminary Safety Analysis Report, Chapter 15.

6. CORE POST STRENGTH LOSS

Some general features of high-temperature graphite corrosion have been discussed in Sect. 4. At high temperatures, the oxidant penetrates diffusively to a depth, Δh, which diminishes with increasing temperature. For one type of graphite, the reaction zone was found to decrease linearly with temperatures between 950 and 1040°C. If this relationship also holds for core post material, and if it is permissible to extrapolate downward in temperature to the core post region, the reaction depth in the core posts would range from about 2.2 to 2.7 mm.

The corrosion rate is highest in the outer portions of the reaction zone where the oxidant concentration is the highest. Therefore, as time progresses, the corrosion reaction tends to form a characteristic burnoff profile with a gradual increase in density from a minimum at the outside up to the initial graphite density at the inner boundary of the reaction zone. When approximately half the graphite is burned off in the reaction zone, an equilibrium profile is achieved; further corrosion proceeds by an inward movement of the reaction zone leaving behind some graphite residue with a density of about 10% of the original material.

Ultimately, one would hope that a rational theory of graphite strength loss due to corrosion would be developed which connects the details of the corrosion process with the microstructural basis of graphite strength. At this time there is insufficient knowledge in either area for much theorizing towards this goal. Therefore, we will adopt a purely empirical approach and develop a correlation which describes most of the available strength loss data reasonably well but which has no theoretical basis.

6.1 Empirical Strength Loss Correlation Based on Data of Helsby and Everett[1]

The graphite reactivity and burnoff profile aspects of the work of Helsby and Everett[1] have been discussed in Sect. 4.2. In addition to the burnoff studies described, the tensile strength of some specimens was measured before and after being subjected to steam corrosion in order to determine the effect of corrosion on strength.

The material used for the tensile tests was a molded, isotropic Gilsocarbon-based graphite, designated as reference No. 96. Gilsocarbon is a naturally occurring pitch in globular form, which, when graphitized yields an isotropic grist particle. Reference No. 96 graphite is triply pitch impregnated with a density of 1.81 g/cm^3, a tensile strength of 2180 psi, a compressive strength of 10,000 psi, and a total ash content of 790 ppm. The specimens, as previously described, were annular in shape with a 4-mm wall thickness and a 14 mm OD. The corrosion surface was the inner diameter.

The corroded samples were mounted in Araldite, and the tensile strength was determined on a Hounsfield Beam Tensometer. The change in tensile strength for a range of burnoffs was studied for specimens corroded at 950°C, 1070°C, and 1130°C. The reported results are reproduced in Fig. 6.1. A given degree of corrosion has the most deleterious effect on the tensile strength at the lowest of the three temperatures. This behavior is generally consistent with the concept of a reaction zone depth which increases with diminishing temperature. A given degree of corrosion is confined to a narrower zone at higher temperatures, and causes a smaller degree of strength loss than if it had occurred at a lower temperature where a larger volume of graphite would be damaged.

The degree of corrosion needed to establish the equilibrium burnoff profile is indicated in Fig. 6.1 for each temperature. These estimates were obtained from the active corrosion depths given in Table 4.5 as a function of temperature and an approximation of the burnoff profile within the corrosion zone. The burnoff profiles were obtained using a semi-theoretical, phenomenological development[2] which yields approximately the observed profiles shown in Fig. 4.5 within the reactive zone. Effectively, these burnoff profiles could be assumed to be linear with no significant change in the computed amount of graphite removed.

After the fully developed corrosion profile has been developed at the indicated degrees of burnoff shown by the arrows in Fig. 6.1, corrosion proceeds inward by movement of the reactive zone, leaving behind a graphite skeleton of perhaps 10% of the original density. Thus, for

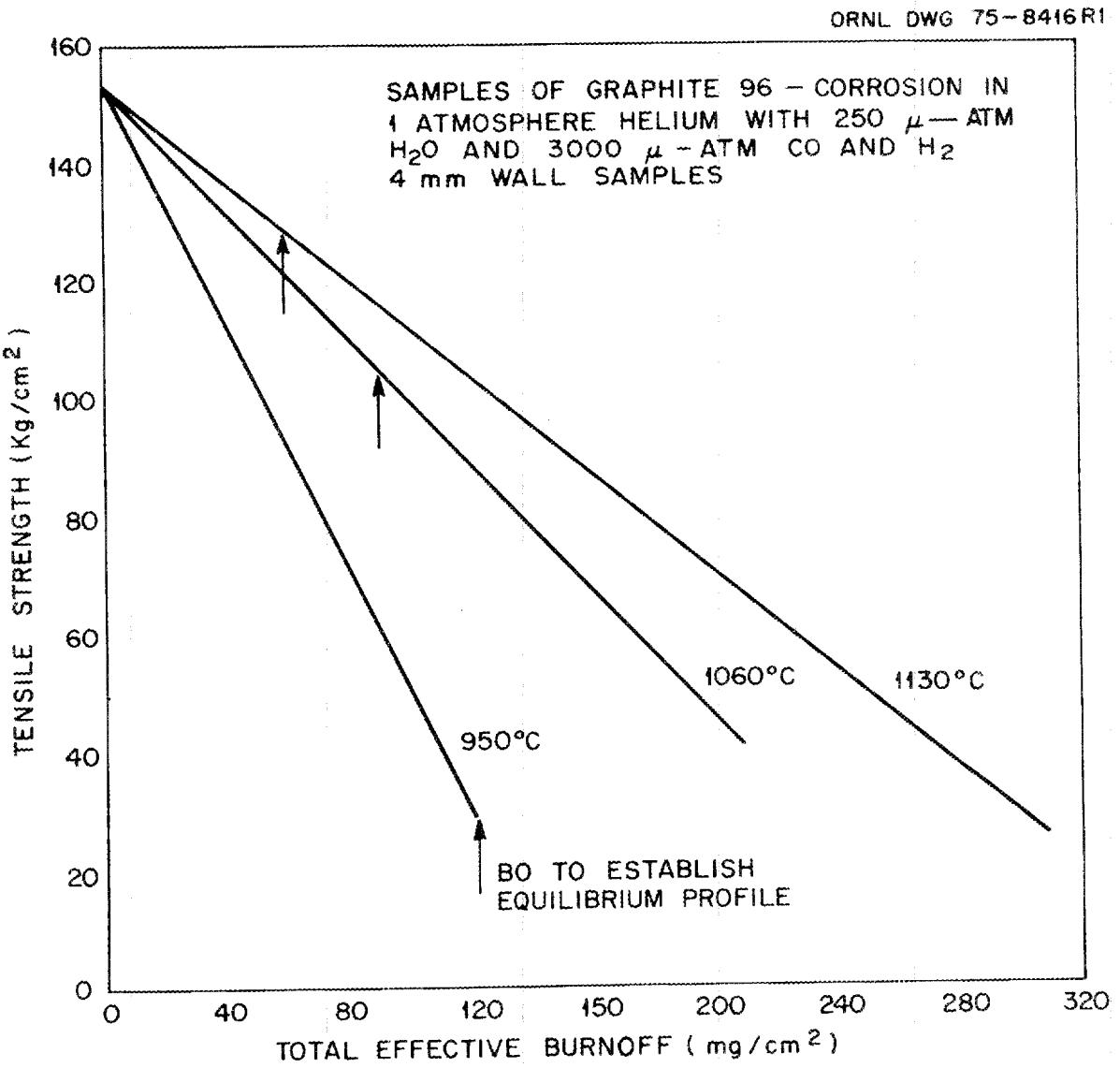

Fig. 6.1. Tensile strength vs burnoff for various temperatures.[1]

burnoffs to the right of the indicated arrows, we should distinguish between the depth of the active zone, which is temperature dependent, and the total depth which depends additionally on exposure time.

The estimated total depth of corrosion at the straight line extrapolation to 100% strength loss for each of the three cases shown in Fig. 6.1 are listed in Table 6.1. For each case, the total predicted corrosion at the burnoff causing 100% strength loss is less than the 4-mm width of the sample. This indicates that the mechanical strength of graphite is damaged by surface corrosion to a greater depth than the obvious or superficial depth of the corrosion. The small extent of the information, however, does not warrant further analysis beyond these more-or-less speculative generalizations.

Table 6.1. Total corrosion depths at 100% strength loss for 4-mm thick samples

Temperature (°C)	Burnoff to reach equilibrium profile (mg/cm^2)	Burnoff (mg/cm^2)	Predicted depth of corrosion at 100% strength loss	
			Active reaction zone (mm)	Total depth (mm)
950	120	150	1.9	2.0
1060	93	290	1.4	2.6
1130	61	370	0.94	2.8

The linear strength loss variation with burnoff depicted in Fig. 6.1 may be organized in an empirical equation of the form

$$FSL = P(T) \cdot \frac{BO}{\rho_{bo}} \cdot \frac{1}{W} \quad , \tag{1}$$

where

FSL = fractional strength loss,

P(T) = penetration depth multiplier which increases with decreasing temperature,

BO = burnoff, g/cm^2,

ρ_{bo} = original density less the density of graphite which remains after complete burnoff ≈ 1.6 g/cm^3,

W = specimen width, cm.

The factor BO/ρ_{bo} would be the corrosion depth if the burnoff were totally drawn from the surface. The temperature dependent factor, P(T), is the required multiplier onto the calculated surface corrosion to yield the observed fractional strength loss shown in Fig. 6.1. Values for the penetration factor at the three test temperatures which yield a fit for the observed degree of strength loss are listed in Table 6.2.

Table 6.2. Burnoff penetration factors as a function of temperature

Temperature (°C)	Penetration factor P(T), Eq. (1)
1140	1.78
1030	2.32
950	4.40
1000	3.20[a]
900	4.50 - 6.00[b]
875[c]	4.80 - 7.10[b]
786[d]	5.95 - 14.0[b]

[a]Interpolated value.

[b]Extrapolated range.

[c]Estimated sustained upper core post temperature.

[d]Nominal core post temperature.

The problem remains of extrapolating values of P(T) down to the core post temperature region. The lowest test temperature of 950°C is 164°C above the nominal core post temperature and 76°C above the estimated

continuous maximum. The penetration factors shown in Table 6.2 for the core post temperature range were obtained by plotting the calculated points and extrapolating graphically. The lower of the two values given for 786°C and 874°C represent a straight line extrapolation, whereas the upper range represents a pessimistic upward trend.

Equation (1) and the penetration multipliers given in Table 6.2 form the basis of the means for determining core post strength loss. The correlation is compared in the next section with strength loss data of 1/2-in.-diam specimens of H-327 corroded at 900°C, and specimens of H-328, S-9567, and TS-688 corroded at 1000°C. In most cases, predicted strength loss compared reasonably well with measured values leading some confidence to the predictive method.

6.2 Comparison of Strength Loss Correlation with Data for H-327, H-328, S-9567, and TS-688

Strength loss data for H-327 graphite undergoing accelerated corrosion by steam in helium at 900°C and 1 atm are shown in Fig. 6.2. The data were reported in ref. 3 and are reproduced also in GASSAR.[4] Both tensile and compressive strength loss data for the 1/2-in.-diam specimens appear to fall on the same smooth curve.

The first step in comparing the strength loss correlation with the data is to convert percent burnoff shown in the figure to surface burnoff used in the strength loss correlation. A simple mass balance yields,

$$BO_1 \cdot \pi D L = \rho \cdot \frac{\pi}{4} D^2 L BO_2 \quad , \tag{2}$$

where BO_2 is the fractional burnoff of a cylindrical specimen of diameter D and density ρ, which is equivalent to a surface burnoff of BO_1, g/cm^2. Thus,

$$BO_1\left(\frac{g}{cm^2}\right) = \frac{D \rho}{4} BO_2 \quad . \tag{3}$$

The fractional strength loss, FSL, of a cylinder of diameter D is obtained from the ratio of the area damaged by corrosion to an estimated

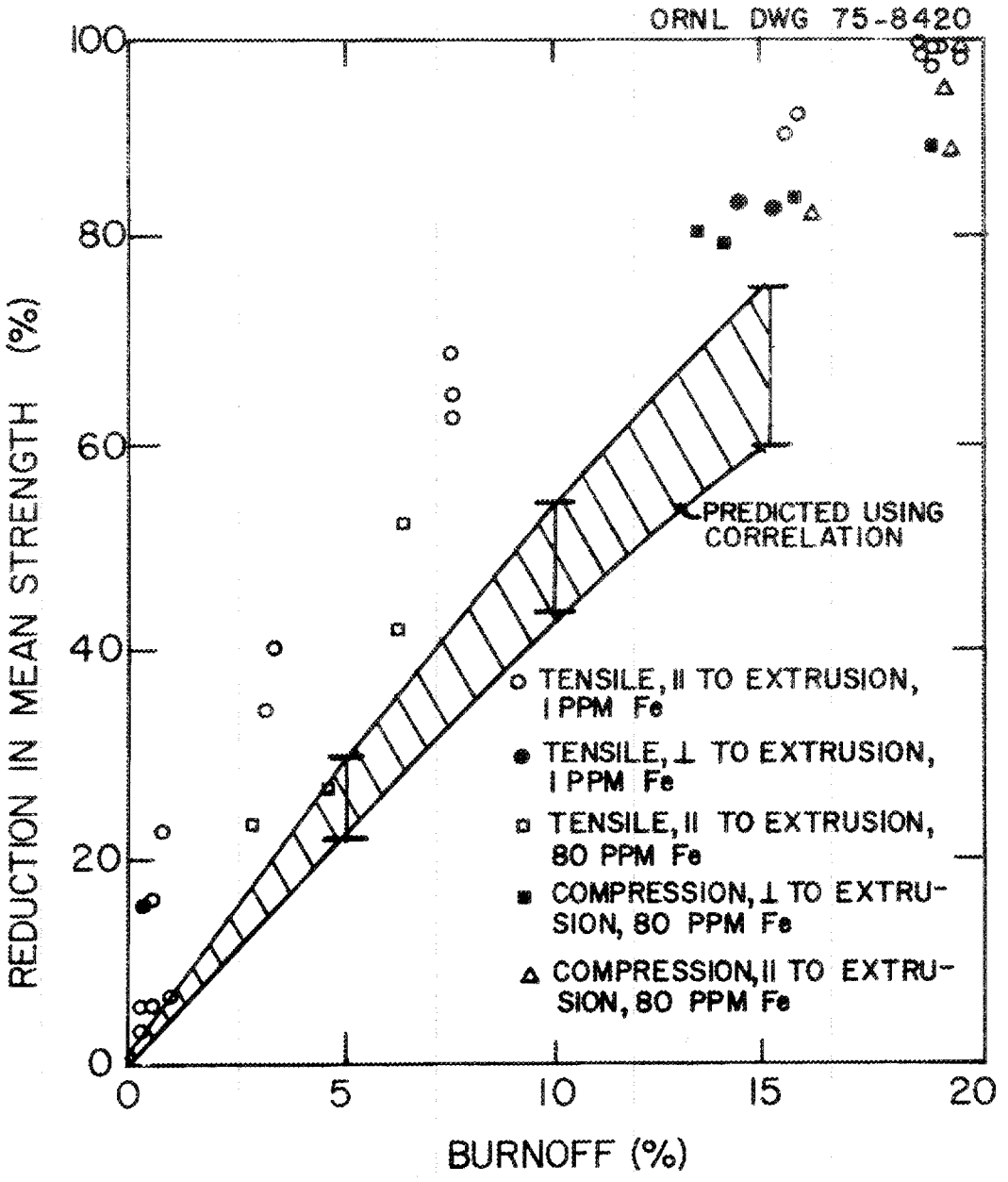

Fig. 6.2. Changes in strength of 1/2-in.-diam samples of H-327 graphite after accelerated steam oxidation at 900°C.

depth $P(T) \cdot BO_1/\rho_{BO}$, to the original specimen cross-sectional area. For cylindrical geometry this yields:

$$FSL = 1 - \left(1 - \frac{2\ P(T)\ BO_1}{\rho_{bo}\ D}\right)^2 \quad . \tag{4}$$

Using the extrapolated range of values for P(T) for 900°C given in Table 6.2 of $4.5 < P(T) < 6.0$, yields the indicated band of predicted strength loss shown in Fig. 6.2. The predicted values fall about 20% below the measured data. This is thought to be good agreement because the specimen shape, temperature, and graphite type all differ from the original study on which the correlation is based.

Figure 6.3,[5] shows tensile strength loss data for 1/2-in.-diam specimens of H-328, S-9567, and TS-688 corroded by steam at 1000°C. The scatter here is rather large, and the envelopes enclosing the S-9567 and TS-688 data were drawn to assist visualization. The predicted strength loss lines were drawn using the penetration parameter value of 3.2 listed in Table 6.2 appropriate for 1000°C. The starting point for the curve was taken as the average tensile strength shown for 0% burnoff.

Despite the scatter of the data, the predicted variation of strength loss generally agrees with the observed trend for H-328 and TS-688 graphites; S-9567 graphite shows a superior behavior under steam corrosion compared with the four other graphites tested. The envelope enclosing the S-9567 data shows a more parallel trend with the axis than either the other data or the prediction by the correlation; but the reason for this behavior is not understood.

6.3 Core Post Loads and Temperatures Under Normal Operating Conditions (NOC)

6.3.1 Core post loads under normal operating conditions

The core support structure must support the core during all normal, upset, emergency, and test conditions. We are concerned solely with the requirements for normal operation which are defined in ref. 6:

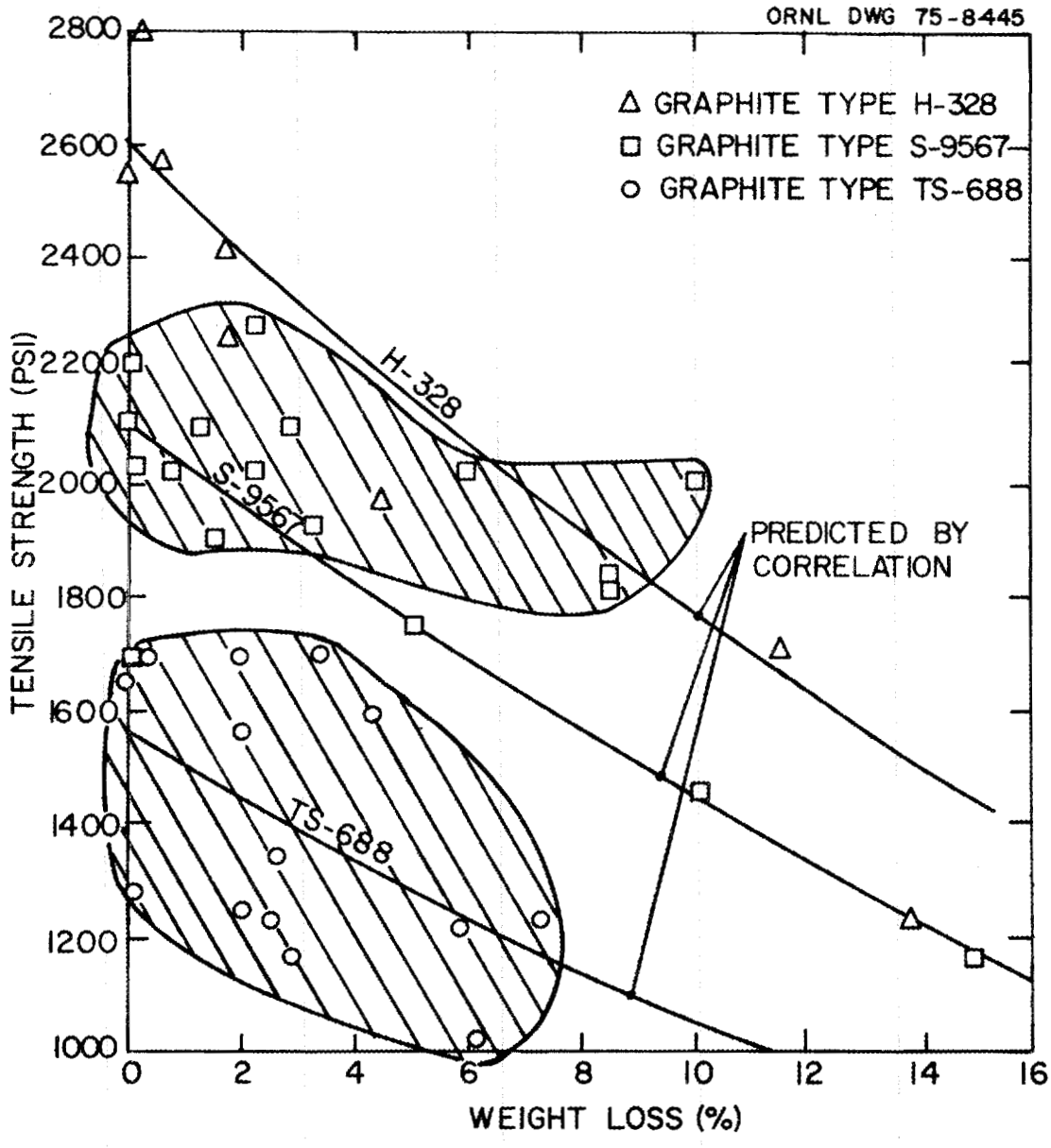

Fig. 6.3. Effect of oxidative weight loss by steam attack at 1000°C on the tensile strength of 1/2-in.-diam graphite specimens.

> "During normal operating conditions, the structure shall have an ultimate static load capacity of five times the primary design load, which consists of the weight of the core support structure, the weight of the core and other supported components, and the core pressure drop. The primary design loads shall include the effects of possible uneven or eccentric load distribution caused by relative displacements of the support members resulting from construction tolerances, PCRV movements, refueling, and thermal expansion."

The portion of the NOC core post load consisting of the static loads and core pressure drop is easily estimated, and may be thought of as an idealized core post load. Under normal operating conditions, many core posts must bear an additional load due to the other factors mentioned above, all of which may be categorized generally as being due to a non-ideal load distribution. The effect of non-ideal load distribution has not been estimated.

The judgment adopted in this study is that non-ideal load distributions can cause a factor of 2 load increase for a significant number of core posts. This is in fair accord with an estimate in GASSAR which states:[7]

> "During NOC, the statically determinate load on a typical core post will be about 12,400 lb_f with a possible upper-bound statically indeterminate load of about 20,000 lb_f."

In our terminology, non-ideal load distributions may cause a factor of 20,000/12,400, or 1.6 increase in load according to ref. 6.

NOC core post stresses are estimated to be 1000 psi, as indicated by statistics shown in Table 6.3. The weight of the core and supporting structures were taken from the Delmarva Power and Light PSAR[8] instead of GASSAR,[6] since we have adopted a 2000 MW(t) HTGR for this study.

The core pressure drop of 11.3 psi must be applied over the entire plenum area including the active core and permanent side reflectors. This area is estimated here simply as the inner PCRV cavity diameters of

Table 6.3. Core post loads and stresses

Weight of core		2,000,000 lb_f
Weight of support structure		250,000
Core pressure drop	11.3 $lb_f/in.^2$	
Applied over area[a]	838 ft^2	
Force due to coolant flow		1,610,000 lb_f
Total ideal NOC load		3,610,000 lb_f
No. of core posts		
3 for each of 55 fuel zones (which include some radial reflector blocks)		165
Assume 3 posts for each of 30 permanent side reflector blocks		90
Total number core posts		255
Ideal load per core post		14,200 lb_f
Ideal compressive stress		500 psi
Total compressive stress		1,000 psi
Ultimate compressive strength of ATJ (clean, cold)[b]		10,000 psi
Safety factor		10

[a] Pertains to cavity diameter of 32 ft 8 in.

[b] Sect. 4.2.

32 ft 8 in. This is slightly high because the thermal barriers are evidently supported by the PCRV and hence do not add to the core post load.

As shown in Table 6.3, a total NOC core post stress of 1000 psi is estimated, which when compared with the ultimate compressive stress for ATJ graphite of 10,000 psi, yields a safety factor of 10. It should be noted that GASSAR[6] also estimates an initial safety factor of 10 for the core posts[6] for the 3000 MW(t) HTGR using the results of model tests. The core post strength loss due to corrosion may reach as high as 50% before the initial safety factor of 10 is reduced to the minimum specified value of 5.

6.3.2 Core post temperature regime

The nominal core post temperature in the reference reactor chosen for this study is 786 °C, which is simply the average coolant exit temperature from the core for this particular design. The average core exit temperature in the GASSAR reference reactor and also in the Delmarva Power and Light Company reactor is 30 °C lower, or 756 °C, whereas 786 °C is representative of the Fort St. Vrain reactor.

It will be shown in Sect. 6.4.3 that these modest differences in assumed nominal core post temperatures do not significantly effect results in spite of the rapid change in reactor rate with temperature — the reaction rate changes by a factor of 2 for about a 30 °C temperature change at these temperatures. However, the core posts are buffered with respect to any modest temperature variability as long as the temperature differences reflect general primary system temperature level differences. The reason for this behavior is that for a given ingress rate a generally hotter primary system will, with its higher core temperatures, be an improved getter for the oxidant. A modest elevation in the primary system temperature would result in lower equilibrium oxidant levels which approximately compensates for the intrinsically elevated corrosion rate at the higher temperature.

The key temperature parameter, and indeed one of the key parameters of this study, is the maximum temperature elevation above the average continually sustained by a significant portion of the core post material.

GASSAR[9] at one point gives the maximum core post "design" temperature as 1048 °C (1918 °F), referred to nominal 770 °C (1418 °F) for a maximum sustained temperature elevation of 278 °C. This appears to be excessively conservative (i.e., too high) for the core posts. No supporting calculations or discussions are offered to justify this high value.

Two factors seem to have a major influence on sustained core post temperature deviations from the mean. First, there are deviations due to departures from the ideal coolant-flow control valve setting for the refueling region. The design of the sensing probe in the core exit thermocouple well is stated in ref. 10 to yield an estimated error of

± 25°C (45°F) in the region exit temperature. However, a later design basis given by GASSAR is not as specific. GASSAR states[11] that the mixed mean coolant temperature for a region will be limited to 827°C (1520°F) for steady state operation. This represents an allowable deviation of +57°C (103°F) referred to the maximum permissible core average exit temperatures for steady state operations of 770°C.

A second factor influencing the maximum sustained core post temperature elevations is hot streaking due to intraregion power tilting. The flow issuing from the coolant channels begins to mix in the exit plenum of the replaceable bottom reflector as shown in Fig. 6.4 (taken from GASSAR). The mixing process continues in the permanent bottom reflector and in the core support block where coolant flows from the seven columns within the zone first begin to mix. The problem of assessing the hot-streaking effect at the core posts is quite complex. Not only is the hydraulic configuration unusual and tortuous, particularly in the support block, but the radial temperature distribution may vary with time during the 4-year life of the fuel elements within the zone.

One indication of the hot-streaking effect at the core posts may be obtained from the results of the steam generator inlet hot streak analysis, the results of which are given in GASSAR,[12] and with somewhat more detail in ref. 13. These results indicate a maximum steam generator "inlet streak temperature" of 790°C (1454°F) at steady state. However, it is not clear whether this refers to the design inlet temperature of 723°C (1330°F), which yields a hot streak temperature rise of 67°C, or if this refers to 751°C (1383°F), which is the maximum anticipated sustained coolant temperatures from one of the four coolant loops. If the latter interpretation is correct, the hot streak temperature rise would be only 39°C. Thus, the value of the hot streak temperature rise at the steam generator inlet lies between 39 and 67°C, depending on interpretation.

A second estimate of the hot streak temperature rise at the core posts may be obtained from the OXIDE-3 computations given in Table 5.8. As noted in Table 5.4, region 2 of the OXIDE-3 program is the hottest column within refueling zones 3 or 6. These results show that the coolant exits the

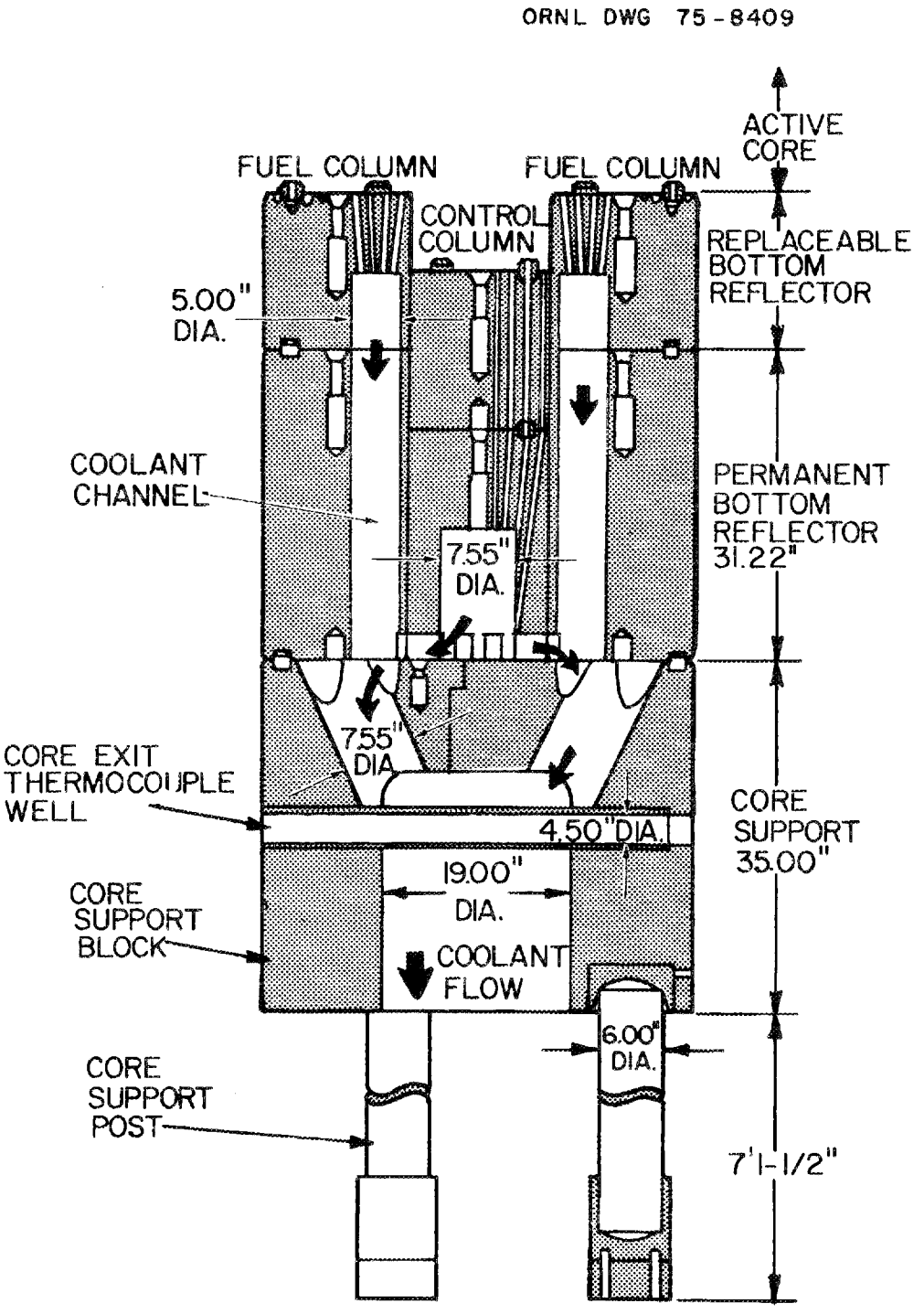

Fig. 6.4. Bottom reflector and core support details.

hottest column in these two refueling zones, 87°C hotter than the core average exit temperatures. This estimate may be high due to the mixing affected in the support block with coolant from the other columns within the region, or it may be low compared with values that might be obtained from other regions. Regions 3 and 6 were selected for this special treatment by the OXIDE-3 program, because the highest radial power factor averaged over one refueling cycle occurs in these two regions. However, other regions with lower average radial power factors may have larger intra-regional power variations, and cause a higher hot streaking effect.

A low value of the hot streaking effect at the core posts may be estimated to be 64°C. This is obtained by summing the thermocouple error of 25°C at the region exit, which determines the value of the regional coolant flow, and 39°C, the low estimate for the hot streak rise at the steam generator.

A higher, reasonable hot streak estimate is obtained by summing the effects of thermocouple error (25°C) with the hot, column temperature increment of 87°C computed for refueling zones 3 and 6. This yields a hot streak effect of 112°C.

Still higher values may be obtained. For example, use of the maximum permissible regional exit temperature elevation of 57°C, instead of solely the thermocouple component of this deviation of 25°C, would add 27°C to the above estimates. At his point, it should perhaps be emphasized that we seek the maximum hot streak effect on a significant portion of the core posts averaged over the 40-year reactor life. Several factors could combine to yield temperature elevations of 112°C or above for times short that are with respect to the 40-year lifetime; however, it may not be reasonable to expect these factors to coincide for the entire 40 years. The time-average hot streak temperatures could be significantly lower than that obtained by simply summing the maximum contributions estimated from each source. Section 6.4 will show that the maximum, continually sustained core post temperature is one of the most sensitive parameters of this study. The attention thus far devoted to a realistic estimate of this parameter has not been adequate. A more careful appraisal would require thermal-hydraulic measurements or analyses such as those performed for the steam

generator hot streak work, combined with intraregional power distribution information, and a reappraisal of the anticipated maximum sustained departure from the ideal regional coolant distribution; all of these effects should be combined and averaged over a sufficiently long time period.

For this study, a judgment has been exercised based on the information presented, that a reasonable estimate of the maximum sustained core post temperature excess over the mean is 90 °C. Thus for this study, the nominal core post temperature is 786 °C, and the maximum sustained core post temperature is taken to be 876 °C.

6.4 Predicted Core Post Burnoffs and Strength Loss at End of Reactor Life

6.4.1 Effect of steam ingress rate

The predicted core post burnoffs that result from 40 years of continuous steam ingress are shown in Fig. 6.5 for the core post at the assumed nominal temperature of 786 °C, and assuming nominal purification flow. The burnoffs, expressed as mg/cm^2, were computed using Eq. (10) derived in Sect. 4.1.3 from ATJ corrosion data. The four curves shown pertain to the four different estimates of the impurity atmosphere at the stated ingress rate. The curve labeled "Dragon" refers to burnoffs calculated from HTGR impurity levels predicted using Dragon steam ingress data as the basis for predicting core reactivity to H_2O. The impurity levels used to obtain this curve are given in Fig. 5.2 and Table 5.6. The remaining three curves were obtained from impurity levels predicted using TIMOX for three assumed corrosion rate expressions for the core graphite. These are derived in Sect. 5.3, and the impurity levels on which these burnoff predictions are based are shown in Figs. 5.8 and 5.9, and Table 5.6.

Figure 6.5 shows that at low steam ingress rates, predicted burnoffs range through about a factor of 5, depending on the assumed core reactivity that determines the environment experienced by the core post. The range begins to narrow for assumed ingress rates of about 0.004 g/sec and reaches only about 50% for ingresses of 0.04 g/sec and above. This is because the

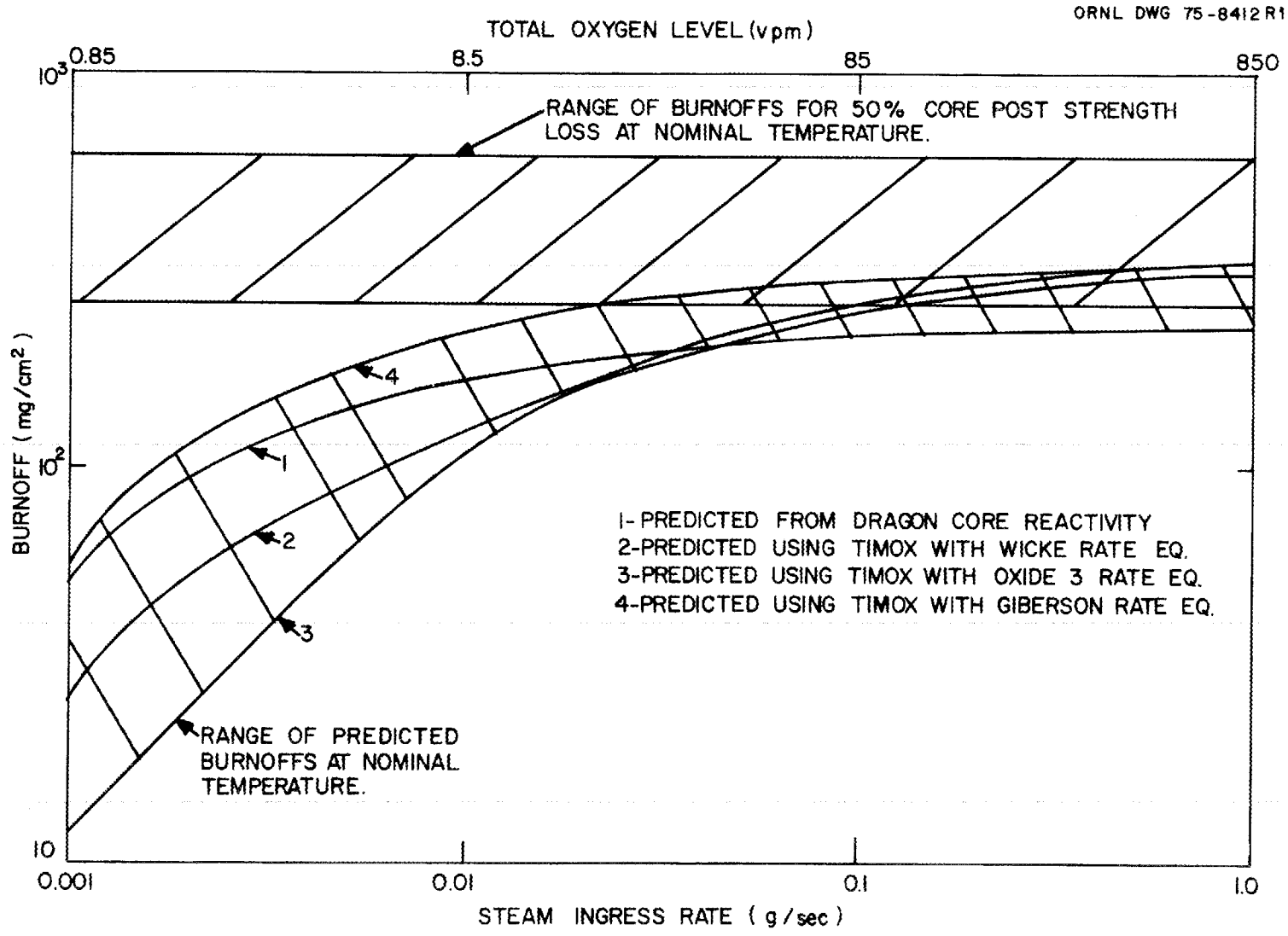

Fig. 6.5. Core post burnoffs at end of 40-year life – for nominal core post temperature and nominal purification flow.

ATJ corrosion expression tends to become zero order (i.e., independent of H_2O concentration) for the higher concentrations resulting from the higher ingress rates. Core reactivity thus is a less sensitive parameter at the higher values of steam ingress.

The degree of burnoff estimated to cause the maximum allowable strength loss of 50% is indicated by the horizontal band. This range was determined by setting the fractional strength loss (FSL) to a value of 0.5 in Eq. (3) of Sect. 6.2, and using the core post diameter, D, of 15.24 cm (6 in.). Solving Eq. (3) for the burnoff for 50% strength loss yields:

$$BO_{50}\left(\frac{g}{cm^2}\right) = \frac{3.68}{P(T)} \quad , \tag{5}$$

where P(T) are temperature-dependent factors given in Table 6.2. For the nominal core post temperature of 786 °C, P(T) is estimated to range between 5.95 and 14.0, which yields the indicated uncertainty band for 50% strength loss.

Figure 6.5 shows that for continuous ingress rated below 0.024 g/sec there is a zero probability of 50% strength loss at the end of the 40-year life, for this case assuming nominal core post temperature. Continuous ingress rates above 0.024 g/sec begin to show some overlap in the range of predicted burnoffs with the range which could result in 50% strength loss. Hence, ingress rates above 0.024 g/sec yield some nonzero probability of 50% strength loss. A general method for predicting the probability for this case of overlapping error bands is outlined in Appendix A. The results show that if the precise burnoff for 50% core post strength loss lies equal probability between the indicated limits (620 mg/cm^2 to 260 mg/cm^2 in Fig. 6.5), and the predicted burnoff also can be with equal probability within the indicated error band at any given ingress rate, the probability for 50% core post strength loss is given by

$$P_1(50) = \frac{(y_2-x_1)^2}{2(x_2-x_1)(y_2-y_1)} \quad , \tag{6}$$

where

$p_1(50)$ = probability for 50% core post strength loss,
y_2, y_1 = upper and lower limit to predicted burnoff range,
x_2, x_1 = upper and lower limit to burnoff range for 50% strength loss.

Equation (6) applies to the case shown in Fig. 6.5 where the error band for predicted burnoffs intrudes partially into the lower portion of the error band for 50% strength loss. The application of values from Fig. 6.5 to Eq. (6) indicates that the probability of 50% core post strength loss at 1.0 g/sec continuous ingress rate is 8%.

The situation with respect to the portions of the core posts at the maximum estimated sustained core post temperature of 876 °C is illustrated in Fig. 6.6. The range of burnoffs is approximately a factor of 8 higher than occurs at the nominal core post temperature. The estimated range of burnoffs that could cause 50% strength loss is also somewhat higher since the values of the penetration factor, P(T), decrease with increasing temperature, as shown in Table 6.2.

The estimates in Fig. 6.6 show that there begins to be some nonzero probability for 50% core post strength loss at ingress rates of 0.0014 g/sec for the core post material at this higher temperature.

For the burnoff range predicted between ingress rates of 0.0014 and 0.0023 g/sec, Eq. (6) may be used to estimate the probability for 50% strength loss. Equation (7), derived in Appendix A, is appropriate for the situation between ingress rates of 0.0023 and 0.007 g/sec, where the estimated range of burnoffs straddles both ends of the range for 50% strength loss. For this case,

$$P_4(50) = \frac{2y_2 - (x_1 + x_2)}{2(y_2 - y_1)} \quad , \tag{7}$$

where definitions are the same as those for Eq. (6). Equation (8) pertains to the region between ingress rates of 0.007 and 0.012 g/sec, where the estimated burnoffs intrude into the upper portion of the 50% strength loss error band:

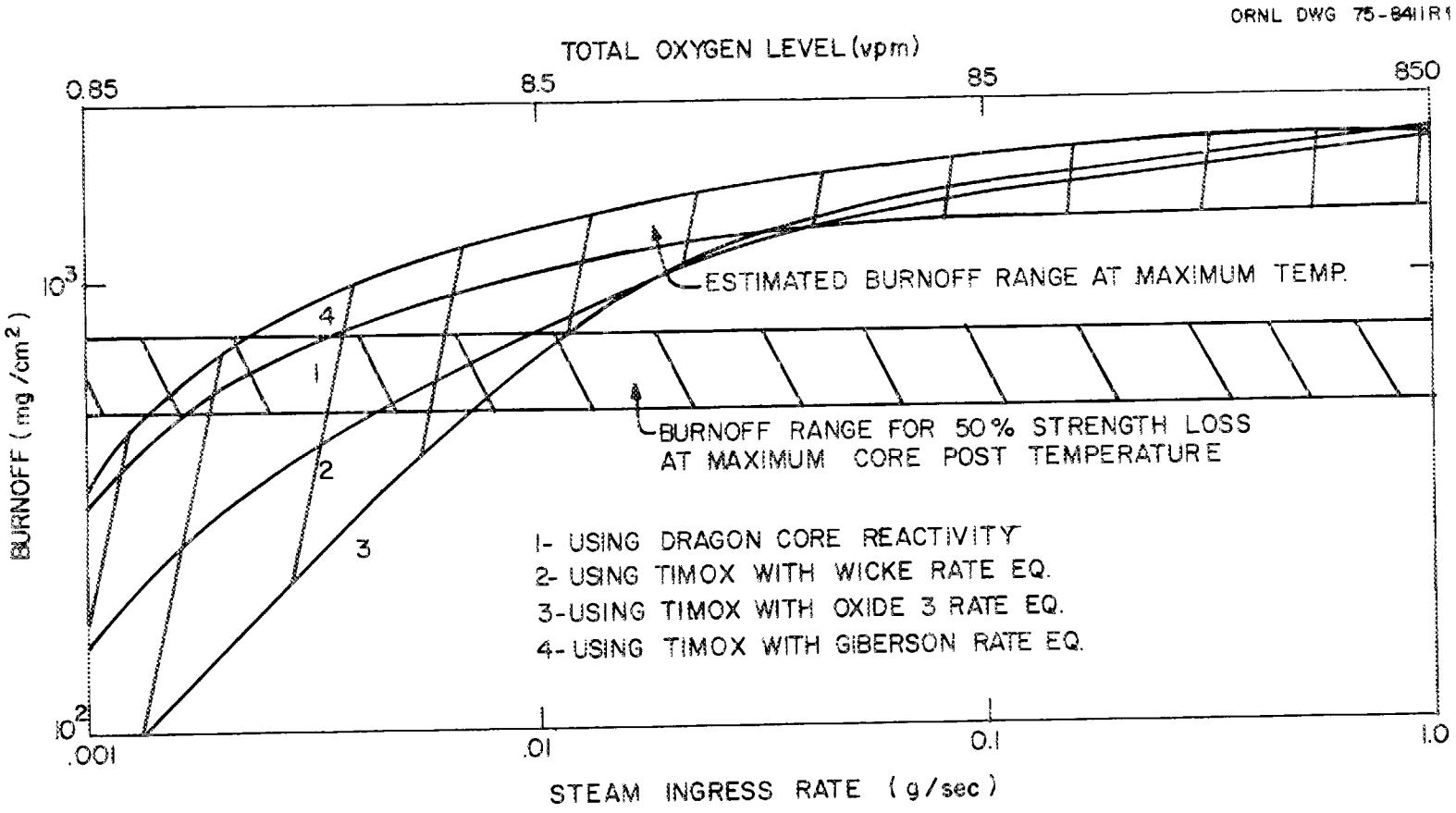

Fig. 6.6. Core post burnoffs at end of 40-year life, for maximum core post temperature and nominal purification flow.

$$P_3(50) = \frac{(x_2-y_1)\left[0.5(y_2+x_1)-x_1\right]}{(x_2-x_1)(y_2-y_1)} + \frac{y_2-x_2}{y_2-y_1} \quad . \tag{8}$$

Ingress rates above 0.012 g/sec yield a probability for 50% strength loss of 100%, since the predicted burnoff band is totally above the 50% strength loss range.

The probabilities for sustaining 50% core post strength loss as a function of continuous, 40-year steam ingress rates are summarized in Fig. 6.7. This figure shows that the probability for 50% strength loss is quite low throughout the examined range of ingress rates for the core posts at the nominal temperature, but is significantly higher for the core post material at maximum sustained temperature. At the 10-vpm total oxygen level projected for ingress rates slightly above 0.01 g/sec, 50% core post strength loss is virtually assured for the post material at the maximum estimated sustained temperature.

Additional details of the predicted range of core post strength loss at nominal purification flow as a function of assumed ingress rates from 0.001 to 1.0 g/sec are given in Figs. B.1-B.4 in Appendix B. These four figures refer to strength losses which result from 40-year exposures to corrosive atmospheres projected from the four estimate methods employed for HTGR core reactivity to H_2O. These figures show that an ingress rate of 0.011 g/sec, which results in a total oxygen level of 10 vpm, would cause a strength loss ranging from 15 to 42% on 40-year exposure of the core posts at the nominal temperature level. The hotter core post material would, under these conditions, lose from 47 to 94% of its initial strength.

6.4.2 Effect of purification rate on core post burnoff and strength

Figure 6.8 illustrates the effect of varying purification flow on burnoff for core posts at both the nominal and highest sustained temperature for an assumed ingress rate of 0.011 g/sec. As in Sect. 6.4.1, the estimated burnoffs are shown as a range covering the span predicted from the four methods employed for calculating the impurity compositions. The burnoff range estimated to cause 50% strength loss at each level of core post temperature is shown as the shaded area on the left of the figure.

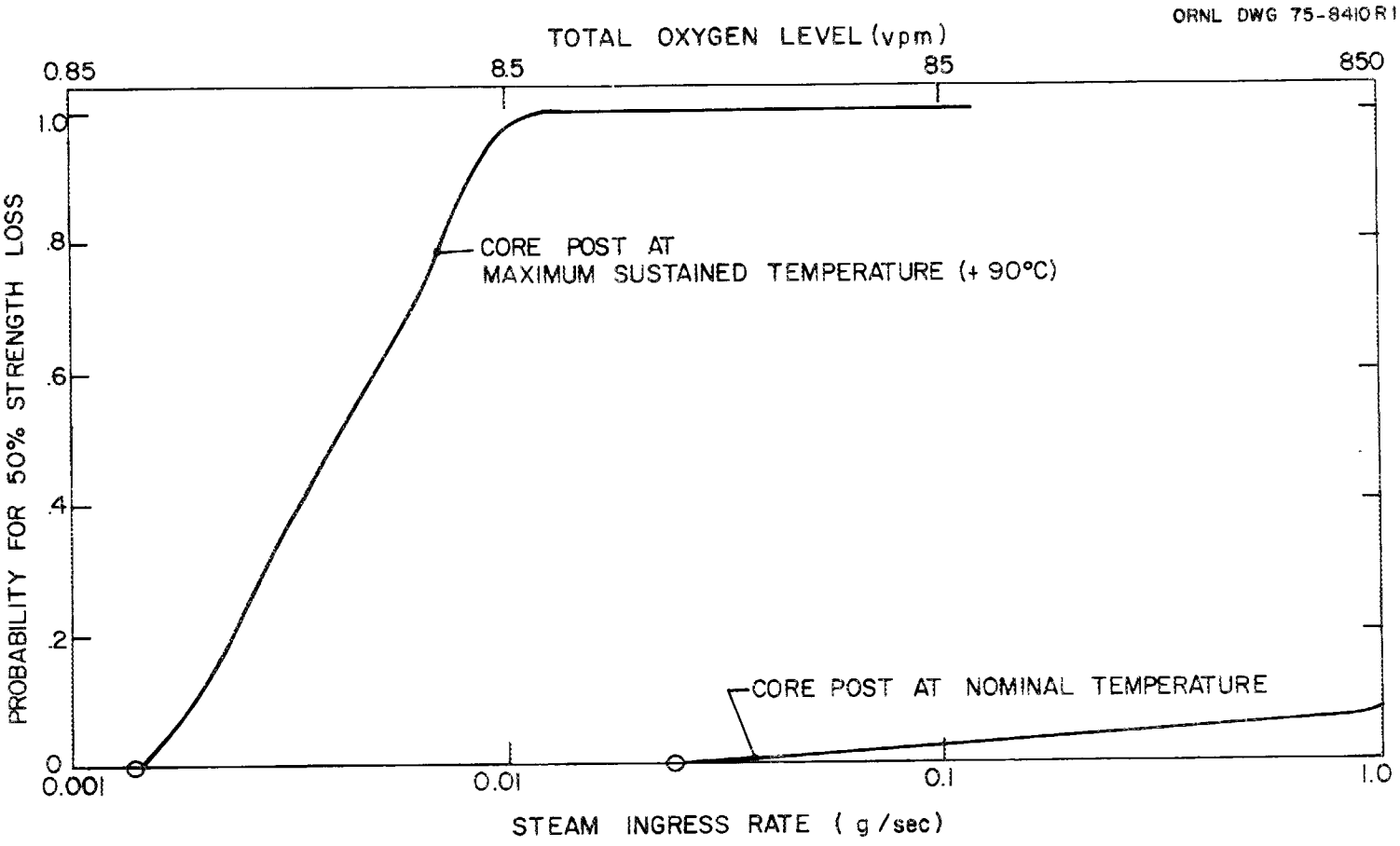

Fig. 6.7. Probability of 50% core post strength loss vs steam ingress rate. Nominal purification rate.

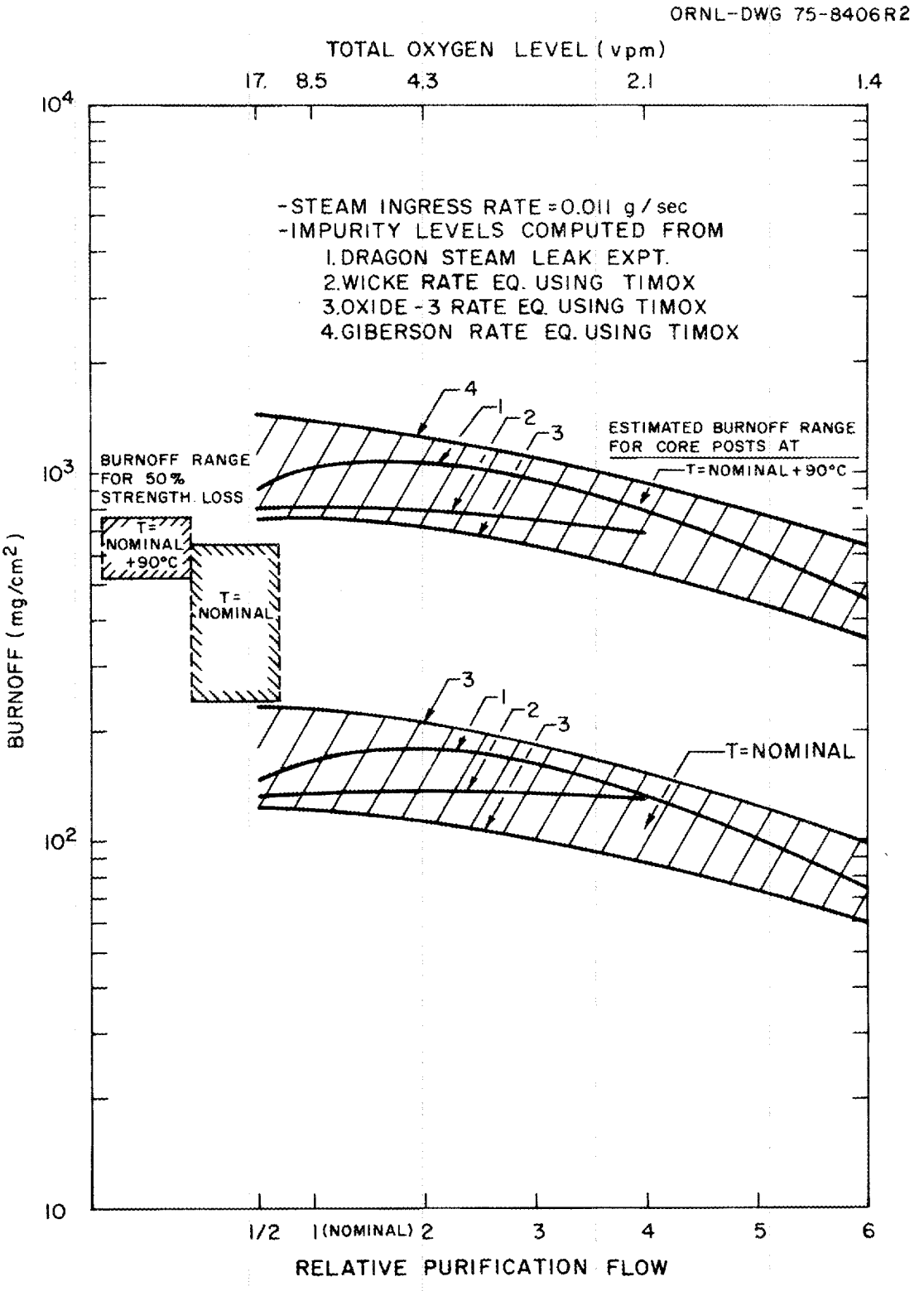

Fig. 6.8. Effect of purification flow on core post burnoff.

A small sensitivity of predicted burnoff to modest variations of the purification rate around the nominal value can be seen. As the purification flow is increased both the products of corrosion, which inhibit the corrosion rate, and the oxidant levels decrease. These concentration trends with purification flow tend to offset each other rendering burnoff insensitive to small changes in purification flow. The figure shows that the burnoff range causing 50% strength loss at the nominal core post temperature lies entirely above these projected burnoffs for 0.011 g/sec steam ingress rate. Thus, the probability for 50% strength loss is zero for the entire range of purification flows. The probability for 50% strength loss is seen to be quite high for the hotter core post material, from purification flows equal to one-half to about five times the nominal rate for this assumed ingress rate.

The probabilities for 50% strength loss, listed in Table 6.4 for these cases, were estimated using the general method outlined in the previous section and in Appendix A.

Table 6.4. Probability for 50% strength loss of core post at maximum sustained temperature as a function of purification rate; assumed steam ingress rate = 0.01 g/sec

Relative purification rate	Total oxygen (vpm)	Burnoff range at maximum temperature (mg/cm^2)	Probability for 50% strength loss
0.5	17	750-1440	0.999
1 (nominal)	8.5	750-1400	0.999
2	4.3	710-1250	0.988
4	2.1	520-940	0.708
6	1.4	370-640	0.111

The estimates in Table 6.4 show that increased purification flows could substantially reduce the probability for 50% strength loss of the hotter core post material, but that significant benefit results only for purification rates above about five times the nominal rate. The results shown in Table 6.4 pertain to an assumed ingress rate of 0.01 g/sec ($\sim$ 0.09 lb_m/hr).

Further details regarding the degree of core post strength loss as a function of purification flow are given in Figs. B.5 and B.6 of Appendix B.

6.4.3 Effect of primary system temperature level on core post burnoff

Since the nominal core post temperature in the reference design chosen for this study is about 30°C higher than selected for GASSAR, and since this temperature difference represents about a factor of 2 increase in intrinsic reactivity of the core post material, it is pertinent to investigate the effect of this difference on the conclusions regarding estimated loss of core post strength.

Several interrelated factors need to be considered for determining the way core post strength loss due to corrosion is affected by increased coolant exit temperatures. As noted above, the intrinsic rate of corrosion increases rapidly with temperature – about a factor of 2 for each 30°C temperature rise for ATJ under these conditions; however, the corrosive environment also changes with increasing coolant temperature. Since the core graphite reactivity to steam determined the corrosive environment, and since an increase in coolant exit temperature must be affected by an increase in core graphite temperature, it is evident that the coolant becomes less oxidizing as the temperature is elevated for a given ingress rate, by virtue of the improved oxidant gettering ability of the core. Hence, the rise in intrinsic corrosion rate of post material with temperature tends to be offset by an accompanying drop in oxidant level. Finally, the burnoff profile in the post material changes with temperature in the manner discussed in Sect. 4.2, with the attendant result that a given amount of corrosion causes less strength loss at a higher temperature. This is

reflected in diminishing values of the penetration factor, P(T), for increasing temperatures.

Figure 6.9 illustrates an estimate of the way core post burnoff varies with a general rise in the primary system temperature of 50°C and 100°C, assuming a nominal purification flow and a steam ingress rate of 0.011 g/sec. The lower set of curves refers to core posts at the nominal temperature, and the upper set of curves refers to post material at the estimated maximum sustained temperature. The impurity levels as a function of temperature were estimated using the TIMOX program in conjunction with the Wicke, OXIDE-3, and Giberson corrosion rate expressions for determining the core reactivity.

The figure shows that when either the Wicke or the OXIDE-3 expression is used to determine the impurity composition, the predicted burnoff is lower when the primary system temperature is elevated 100°C, compared with the predicted burnoff at the nominal temperature level. This is true for both the average core post temperature and the maximum sustained core post temperature. However, when the Giberson rate expression is used for the core graphite, an opposite effect is seen – the estimated burnoff is higher at the elevated primary system temperature.

The way these burnoffs affect core post strength is illustrated in Fig. 6.10. Improved retention of strength with primary system temperature rise is shown for cases where the Wicke and OXIDE-3 rate expressions are used for the core graphite reactivity. When the Giberson rate expression is used, evidently no major change of estimated strength loss with temperature occurs.

Figure 6.10 shows that more precise information on core reactivity to steam corrosion is required before one can confidently predict the effect of primary system temperature changes on core post strength loss due to corrosion. Apparently, a reasonable chance exists that elevated primary system temperatures may improve the core post situation as a result of: (1) improved oxidant gettering by the core, and (2) smaller strength loss for a given degree of corrosion at the higher temperature.

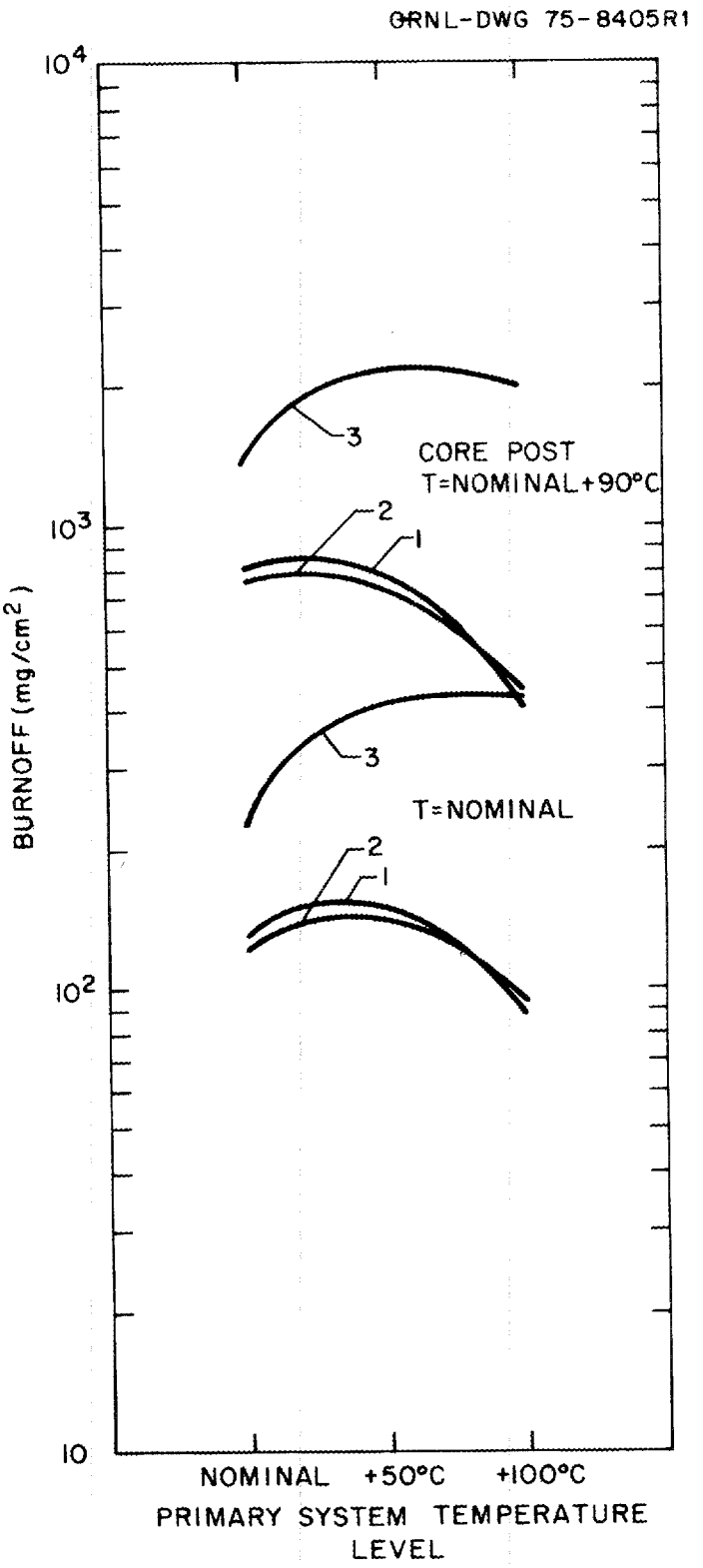

Fig. 6.9. Effect of general temperature level in the primary system on core post burnoff. Purification flow = nominal, steam ingress rate = 0.011 g/sec. Based on impurity levles using TIMOX; 1. Wicke; 2. OXIDE-3; 3. Giberson rate equations.

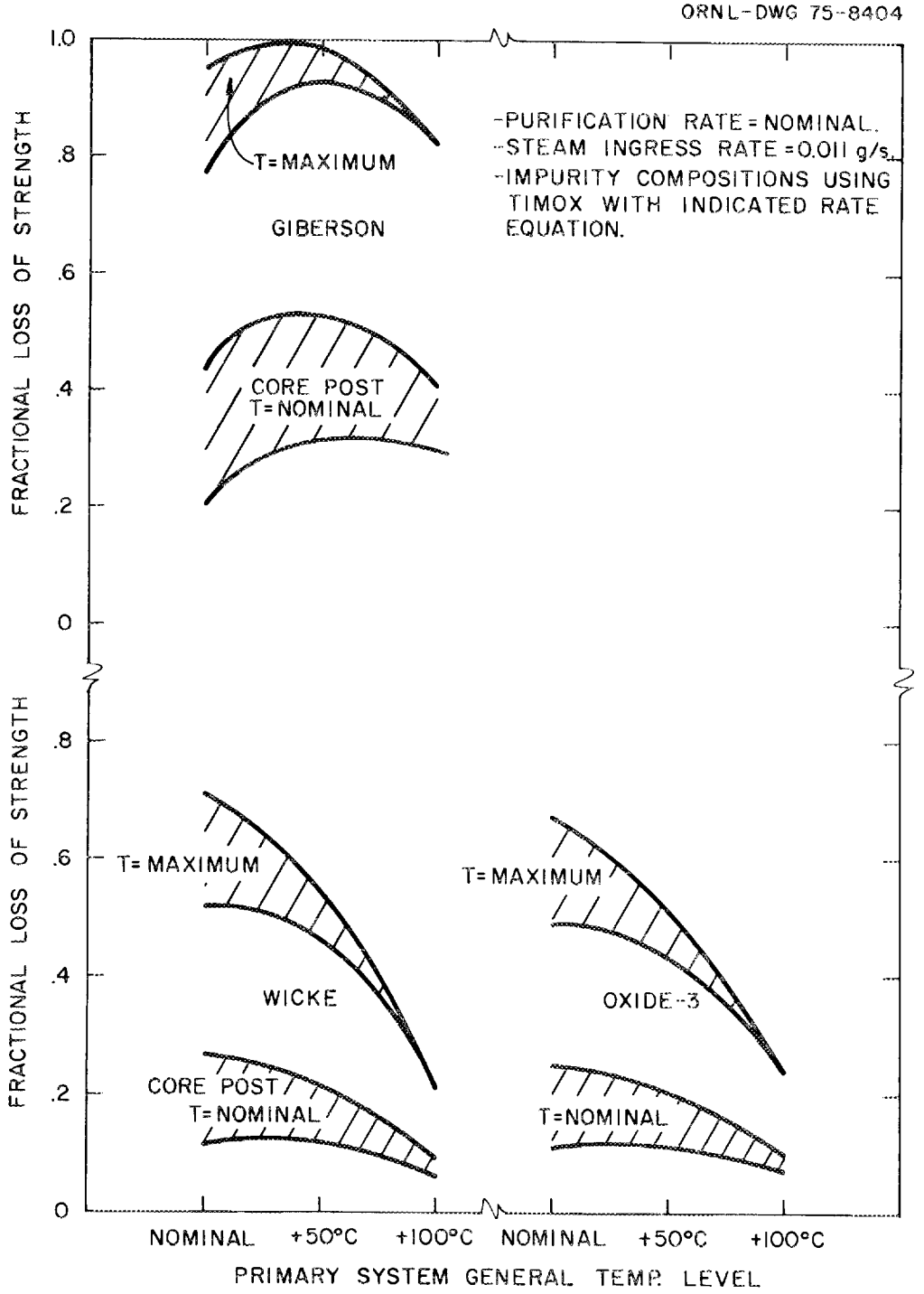

Fig. 6.10. Loss of core post strength vs a general temperature elevation in the primary system.

6.4.4 Maximum permissible oxygen and oxidant levels

The total oxygen concentration (defined as the sum of oxygen in all oxygen-bearing species) in the primary circuit is a function solely of the relative steam ingress and purification rates, which allows the curves in Figs. 6.5-6.7 to be plotted against either the steam ingress rate or total oxygen concentration on the abscissa. Figure 6.7 indicates that the presently considered maximum allowable total oxygen level of 10 vpm assures that the core posts at nominal temperature will not suffer 50% strength loss in 40 years of exposure. However, the core post material at the estimated maximum sustained temperature of 90°C above nominal will likely suffer 50% strength loss.

It is beyond the scope of this report to comment extensively on maximum permissible oxidant levels. Figure 6.7 shows that 10-vpm total oxygen may be too high a limit; however, more extensive studies are needed before any definite limit is set, or before it can be stated positively that 10 vpm is indeed too high. The following additional studies are required:

(1) More precise definition of the maximum sustained core post temperature is needed. This study would involve hot streaking analyses, analyses of flux or power distributions within a refueling zone, and operational characteristics of the coolant orificing system which regulates the coolant distribution radially across the core.

(2) The volume and location of the hot zones should be determined. If the core post material experiencing these higher temperatures is sufficiently small, perhaps the requirement for a safety factor of 5 for this portion of the core posts could be relaxed. For example, if a safety factor of 2 were permitted for a sufficiently small region or set of regions, 80% strength loss would be permissible. The maximum allowable total oxygen level would then be set on the basis of 50% strength loss for the nominal posts and 80% loss for the hotter posts, whichever is lower.

Since the burnoff rate depends far more directly on the oxidant concentration, H_2O and CO_2, than the total oxygen level, which includes CO that actually inhibits corrosion, it appears that an improved definition of maximum permissible impurity level could be stated in terms of total oxidant rather than total oxygen. The broad error band on predicted burnoffs shown in Figs. 6.5 and 6.6 is due to differences in the predicted distribution of a known amount of total oxygen between oxidant, H_2O, and product of corrosion, CO. The four core reactivities employed predict varying distributions. If this information were plotted against H_2O concentration instead, the error band would be much narrower, as seen in Figs. 6.11 and 6.12.

Figure 6.11 indicates that the probability for 50% strength loss is zero for the nominal core posts if the steady H_2O level is sustained below 20 vpm. Very high H_2O levels do not greatly increase the probability for 50% strength loss; for example, P(50) = 8.5% at 1000 vpm H_2O for the nominal core posts. In an actual case where significant radiolytic CO_2 levels exist, the total oxidant concentration would simply be stated as the sum of the H_2O and CO_2 concentrations.

Figure 6.12 shows that the core post material at the maximum sustained temperature has a zero probability of 50% strength loss at continuous oxidant levels below 1.0 vpm, and 100% probability for 50% strength loss above 5.3-vpm oxidant.

6.5 References for Section 6

1. G. H. Helsby and M. R. Everett, Some Graphite Corrosion Problems Related to HTGR's, D.P. Rept. 566 (August 1968).

2. R. P. Wichner, personal communication, August 1975.

3. HTGR Base Program Quart. Progr. Rept. for Period Ending Aug. 31, 1971, GGA-A10784 (September 1971); Fig. 4.1, p. 3.

4. GASSAR-6 – Fig. 4.2-19.

5. Public Services Company of Colorado, Research and Development Program, Quart. Progr. Rept. for Period Ending Sept. 30, 1966, GA-7453 (February 1967), Fig. 3.31, p. 130.

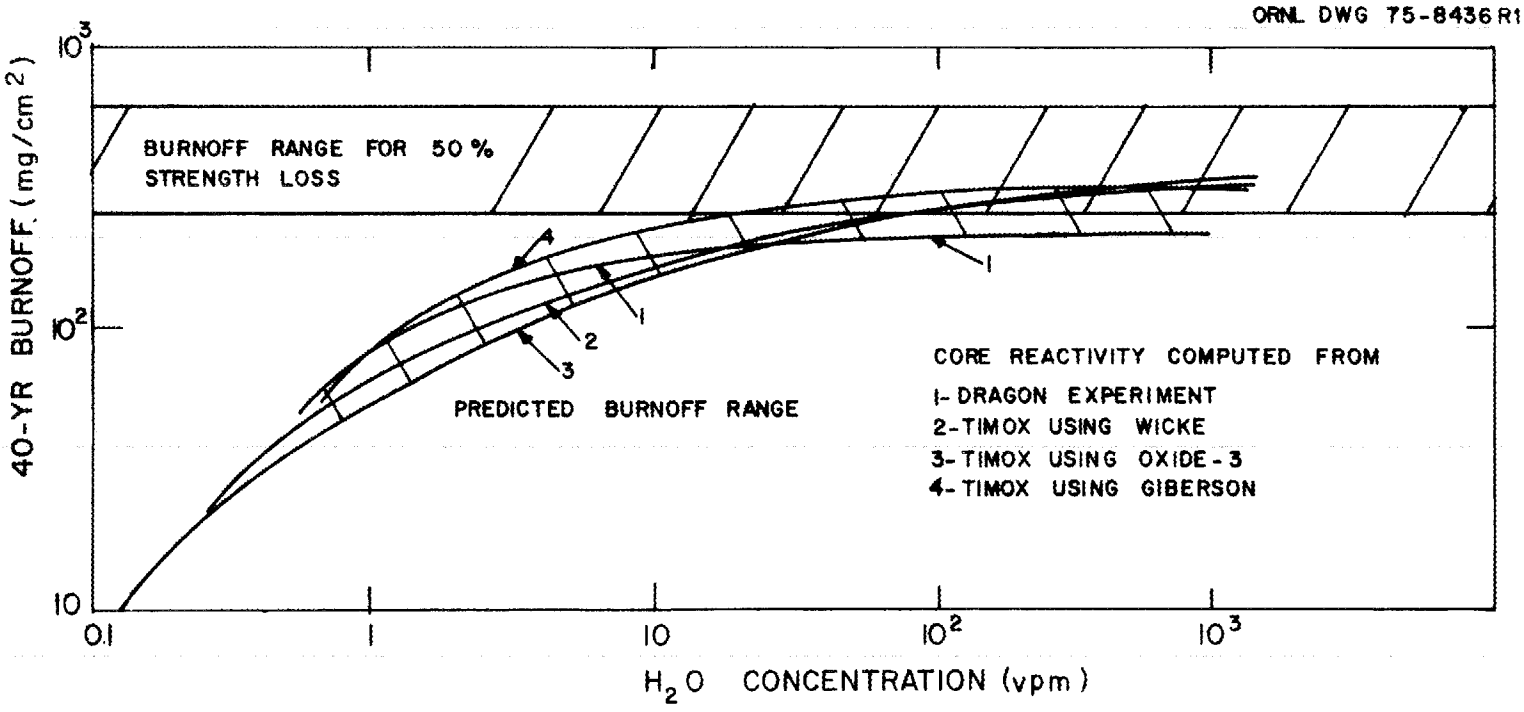

Fig. 6.11. Forty-year core post burnoffs vs vpm-H_2O. Nominal core post temperature.

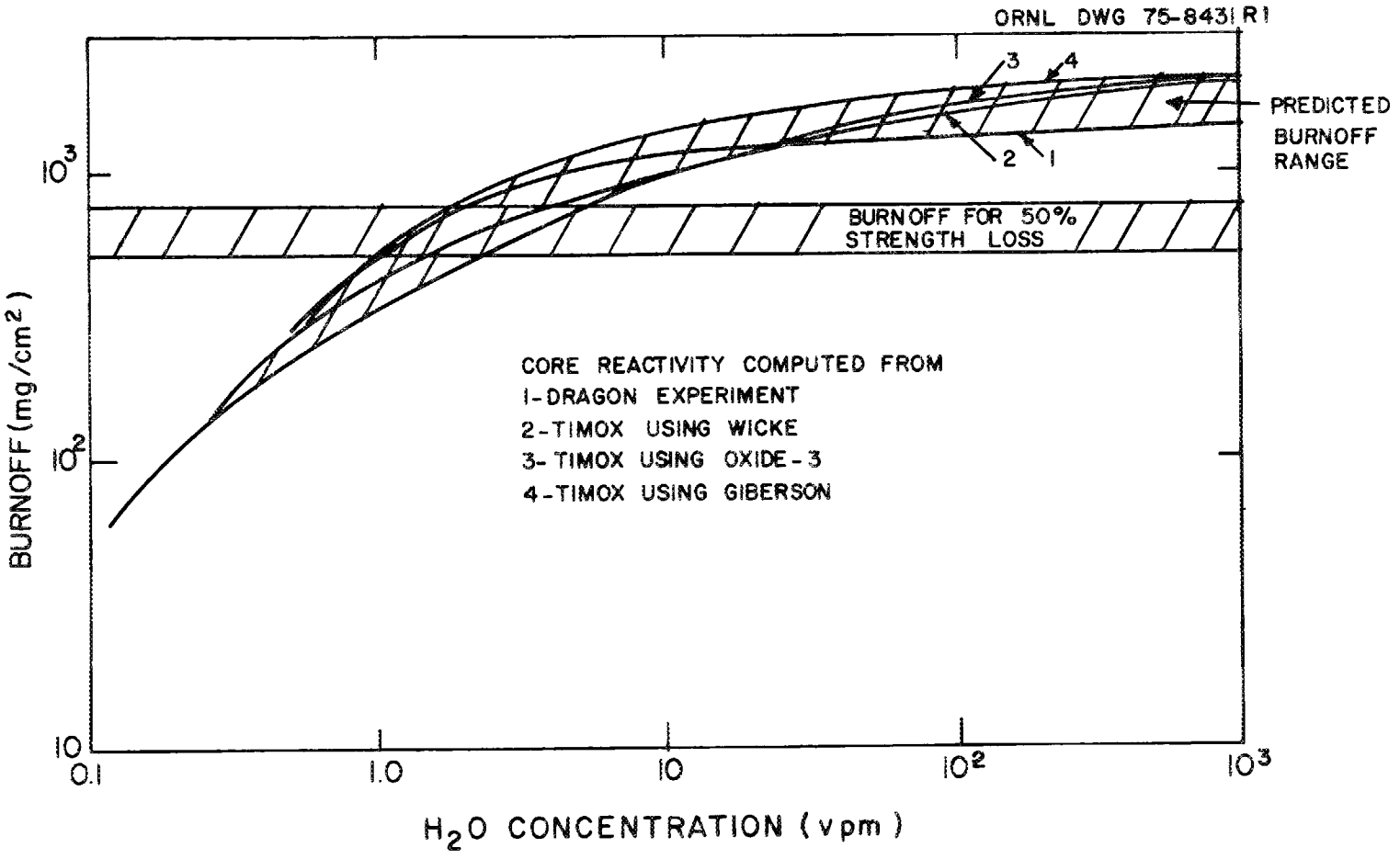

Fig. 6.12. Forty-year core post burnoff vs vpm-H_2O. Maximum sustained core post temperature.

6. GASSAR-6, Section 4.2, p. 57

7. GASSAR-6, Section 4.2, p. 76.

8. Delmarva Power and Light Preliminary Safety Analysis Report, Section 4.2.2.1.2.

9. GASSAR-6, Table 4.2-13.

10. Delmarva Power and Light Preliminary Safety Analysis Report, Section 4.4.2.3.1.

11. GASSAR-6, Section 4.4.1.2.

12. GASSAR-6, Section 5.4.1.5, Table 5.3-1.

13. Delmarva Power and Light Preliminary Safety Analysis Report, Section 5.3.2.5, Table 5.3.1-1, and Appendix E.

7. ACKNOWLEDGMENTS

I am most grateful for the assitance provided by D. J. Strickler of the Computer Sciences Division in communicating with the computer and particularly for the development of the TIMOX program. C. W. Nestor, Jr., also of the Computer Sciences Division aided significantly in developing the probabilistic method of presenting the results which are derived in Appendix A.

APPENDIX A: METHOD FOR ESTIMATING PROBABILITY OF 50% CORE POST STRENGTH LOSS FOR CASES WHERE THE ESTIMATED BURNOFF RANGE AND THE RANGE FOR 50% STRENGTH LOSS OVERLAP

Let f(X) be the probability density function for burnoffs which cause 50% strength loss, where X is a random variable signifying value of burnoff. Thus,

$$\left\{\begin{array}{l}\text{probability that the burnoff} \\ \text{which causes 50\% strength loss} \\ \text{lies in dX about X}\end{array}\right\} = f(X)dX. \tag{A1}$$

The distribution function for burnoffs which cause 50% strength loss, F(X), defines the probability that 50% strength loss has occurred at X value of burnoff or below.

$$F(X) = \int_0^X f(X')dX'. \tag{A2}$$

A flat density function is assumed in this work; that is, the burnoff which causes 50% strength loss can with equal likelihood be a value between the upper and lower limits, x_2 and x_1. For this case, f(X) is given by

$$\begin{array}{ll} 0 & 0 < X < x_1 \ , \\ \dfrac{1}{x_2 - x_1} & x_1 < X < x_2 \ , \\ 0 & X > x_2 \ , \end{array} \tag{A3}$$

hence, F(X) is given by

$$\begin{array}{ll} 0 & 0 < X < x_1 \ , \\ \dfrac{X - x_1}{x_2 - x_1} & x_1 < X < x_2 \ , \\ 1 & X > x_2 \ . \end{array} \tag{A4}$$

Let g(Y) be the probability density function for estimated burnoffs, that is,

$$\left\{\begin{matrix}\text{probability that estimated burnoff}\\ \text{lies within dY about Y}\end{matrix}\right\} = g(Y)dY. \qquad (A5)$$

For a flat distribution between upper and lower limits y_2 and y_1, $g(Y)$ is given by

$$\begin{matrix} 0 & Y < y_1 \\ \dfrac{1}{y_2 - y_1} & y_1 < Y < y_2 \\ 0 & Y > y_2 \end{matrix} \quad , \qquad (A6)$$

Therefore, the probability that burnoff Y about dY occurs within the error band of estimated burnoffs, and that 50% strength loss is caused by this amount of burnoff or less, is given by,

$$P(50) = \int_0^\infty g(Y)F(Y)dY \quad , \qquad (A7)$$

where P(50) is the probability for 50% strength loss.

Expressions for the probability of 50% strength loss will be obtained for four cases of burnoff ranges, each assuming the flat distributions represented by Eqs. (A4) and (A6).

Case I:

The estimated burnoff range, y_1 to y_2, intrudes into the lower portion of the burnoff range for 50% strength loss, x_1 to x_2.

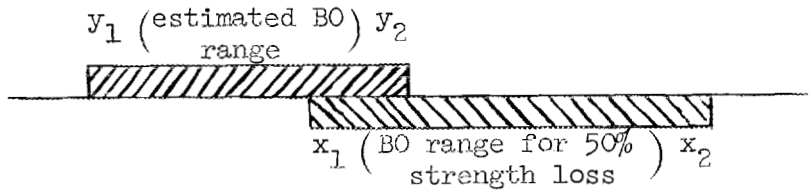

$$P_1(50) = \frac{(y_2 - x_1)^2}{2(x_2 - x_1)(y_2 - y_1)} \quad . \qquad (A8)$$

Case II:

The estimated burnoff range is totally enclosed in the range which may cause 50% strength loss.

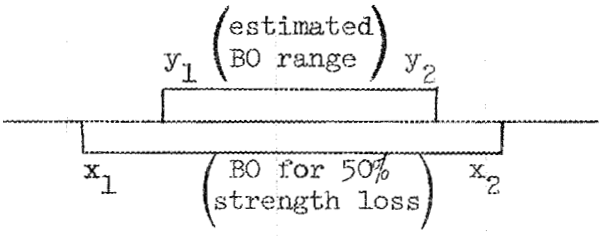

$$P_2(50) = \frac{\frac{1}{2}(y_1 + y_2) - x_1}{(x_2 - x_1)} \quad . \tag{A9}$$

Case III:

The estimated burnoff range extends beyond the upper part of the range for 50% strength loss.

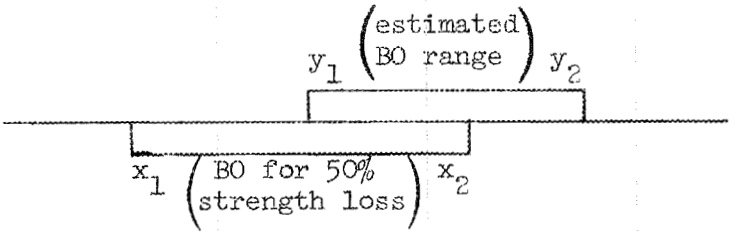

$$P_3(50) = \frac{(x_2 - y_1)\left[\frac{1}{2}(x_2 + y_1) - x_1\right]}{(x_2 - x_1)(y_2 - y_1)} + \frac{y_2 - x_2}{y_2 - y_1} \quad . \tag{A10}$$

Case IV:

The estimated burnoff range straddles the range for 50% strength loss.

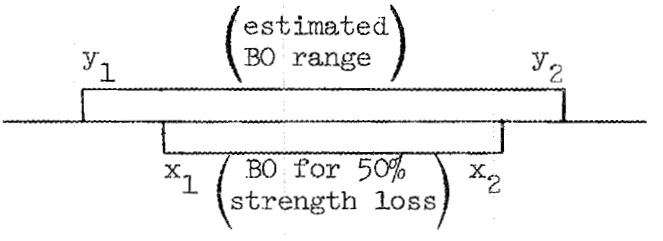

$$P_4(50) = \frac{2y_2 - (x_1 + x_2)}{2(y_2 - y_1)} \quad . \tag{A11}$$

APPENDIX B: CORE POST STRENGTH LOSS VS STEAM INGRESS RATE AND PURIFICATION FLOW. SUPPLEMENTARY INFORMATION TO SECTION 6.4

Figures B.1-B.4 depict the estimated range of core post strength loss for assumed steam ingress rates of from 0.001 to 1.0 g/sec. These estimates all pertain to the case of nominal purification flow.

The information shown in the figures was generated as follows:

(1) The impurity level and composition for an assumed ingress rate was determined from methods described in Sect. 5. Figure B.1 is based on an atmosphere determined from Dragon inleakage data by methods described in Sect. 5.2. Figures B.2-B.4 are based on impurity compositions predicted by using TIMOX, described in Sect. 5.3, and assuming the Wicke, OXIDE-3, and Giberson rate equations for the core reactivity, respectively.

(2) The burnoff was estimated by using Eq. (10) of Sect. 4.1 for ATJ graphite.

(3) The fractional strength reduction was determined using Eq. (3) of Sect. 6.4, with penetration factors for the two temperature levels given by Table 6.2. The depicted range of uncertainty is caused by the uncertainty in the value of the penetration factor.

Figures B.5 and B.6 show the predicted variation of core post strength loss with changing purification flow for an assumed ingress rate of 0.01 g/sec. The calculational procedures correspond closely with those previously described for Figs. B.1-B.4.

The bottom of Fig. B.5 shows the case where the core reactivity was determined from the Dragon steam ingress experiment. The top of Fig. B.5 and the two cases shown in Fig. B.6 refer to estimates made using TIMOX to predict the composition of the impurities in the primary system.

As discussed in Sect. 6.4.2, the variation of strength loss with purification flow tends to be flatter than anticipated, because the

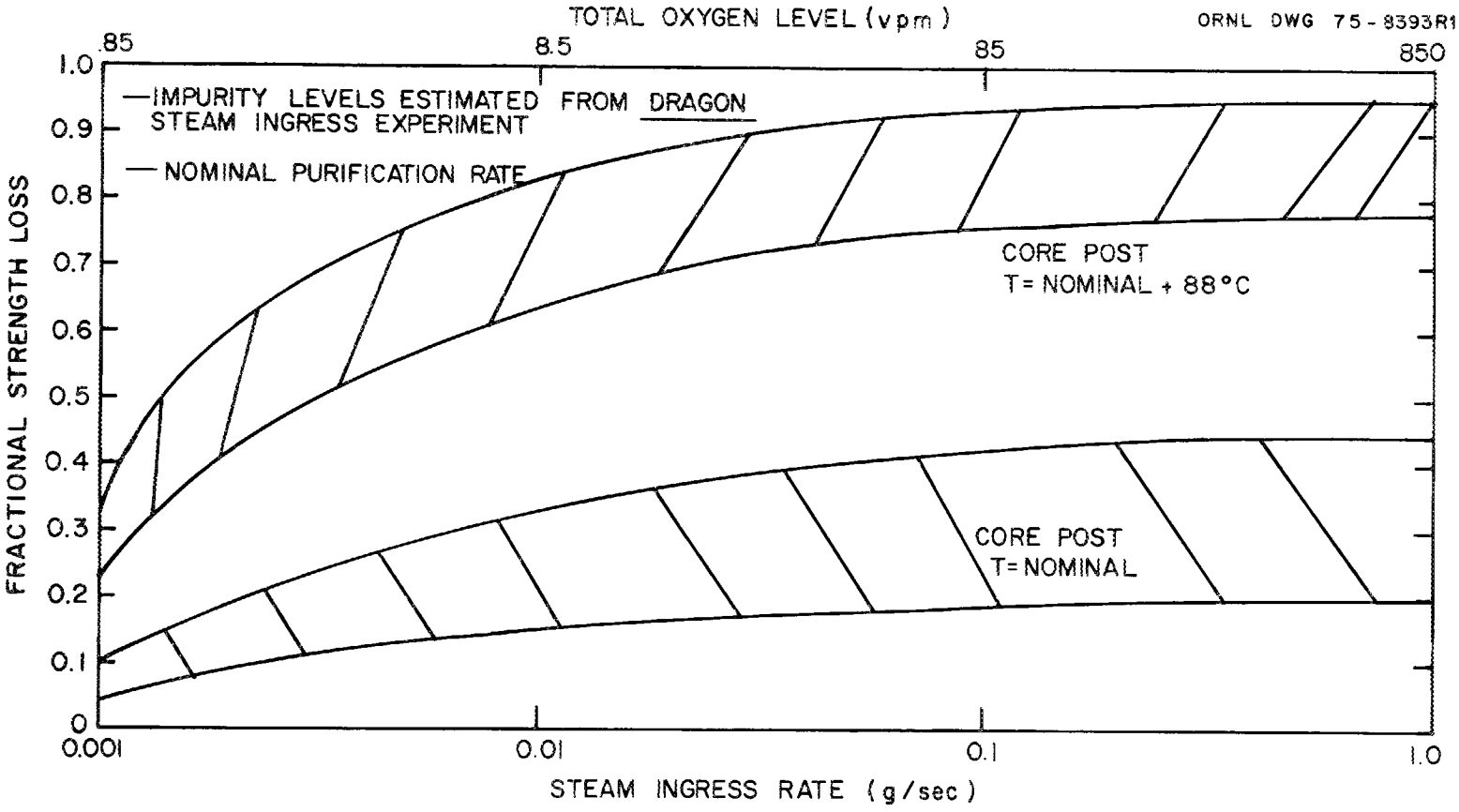

Fig. B.1. Forty-year core post strength loss vs steam ingress rate.

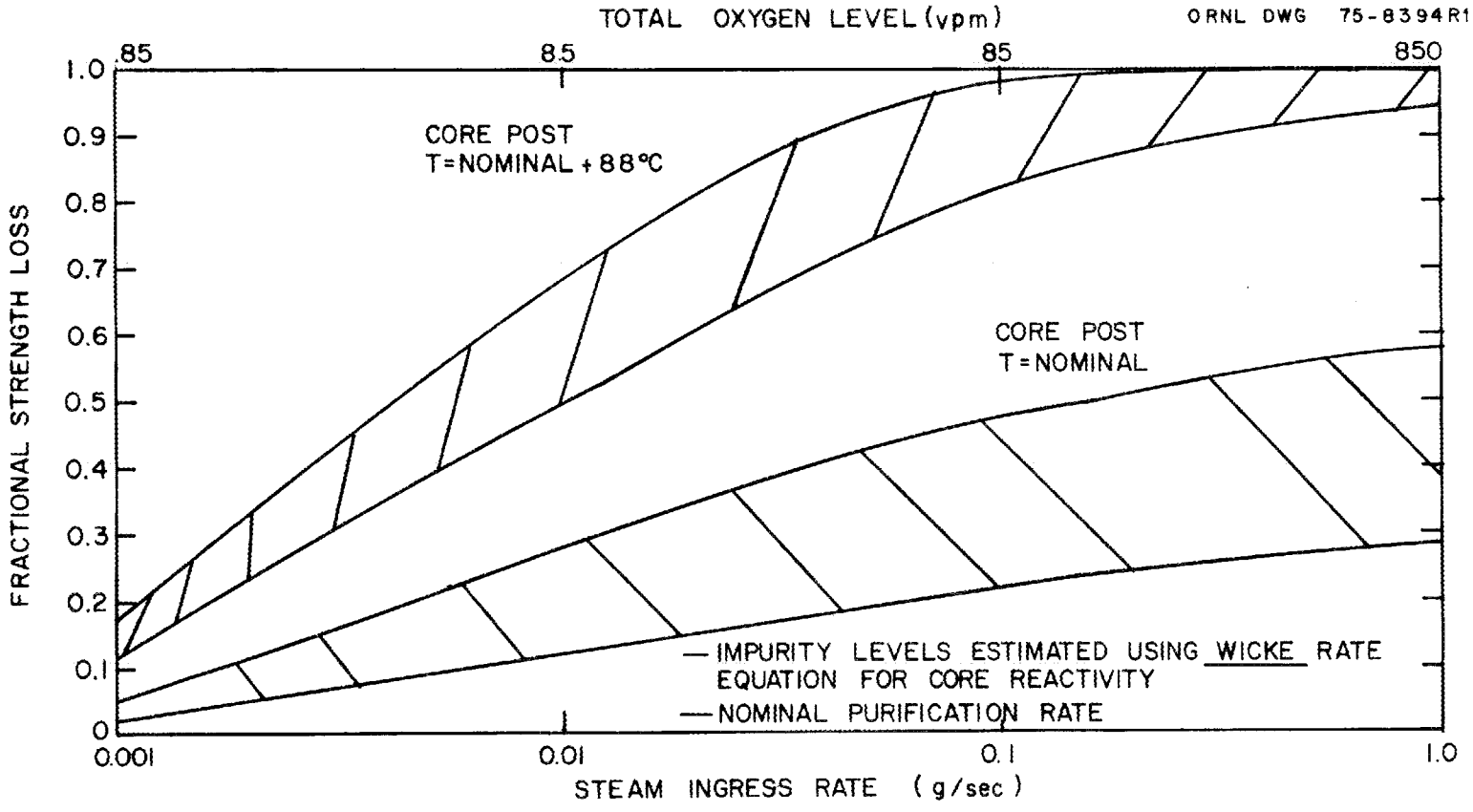

Fig. B.2. Forty-year core post strength loss vs steam ingress rate.

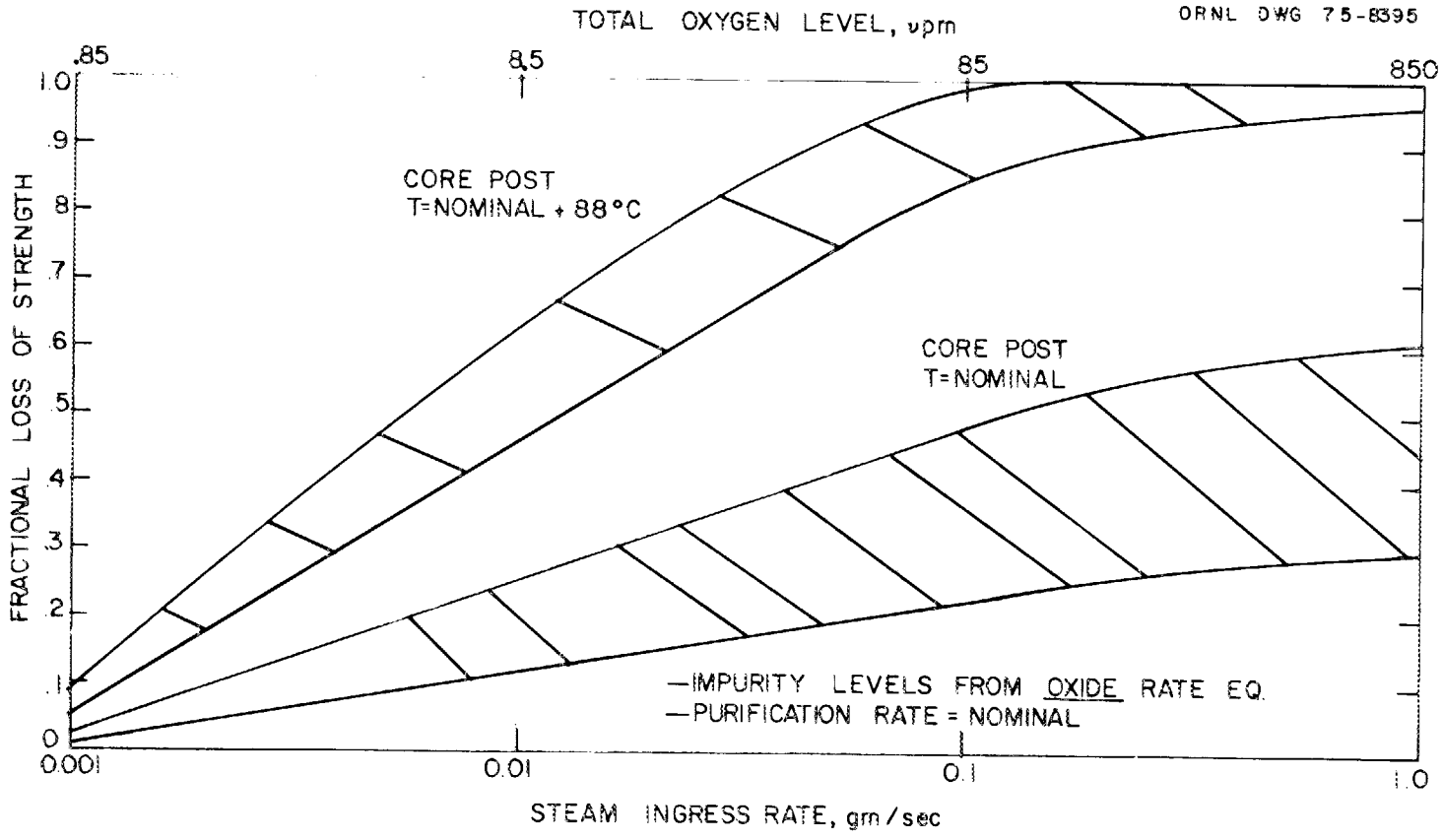

Fig. B.3. Forty-year core post strength loss vs steam ingress rate.

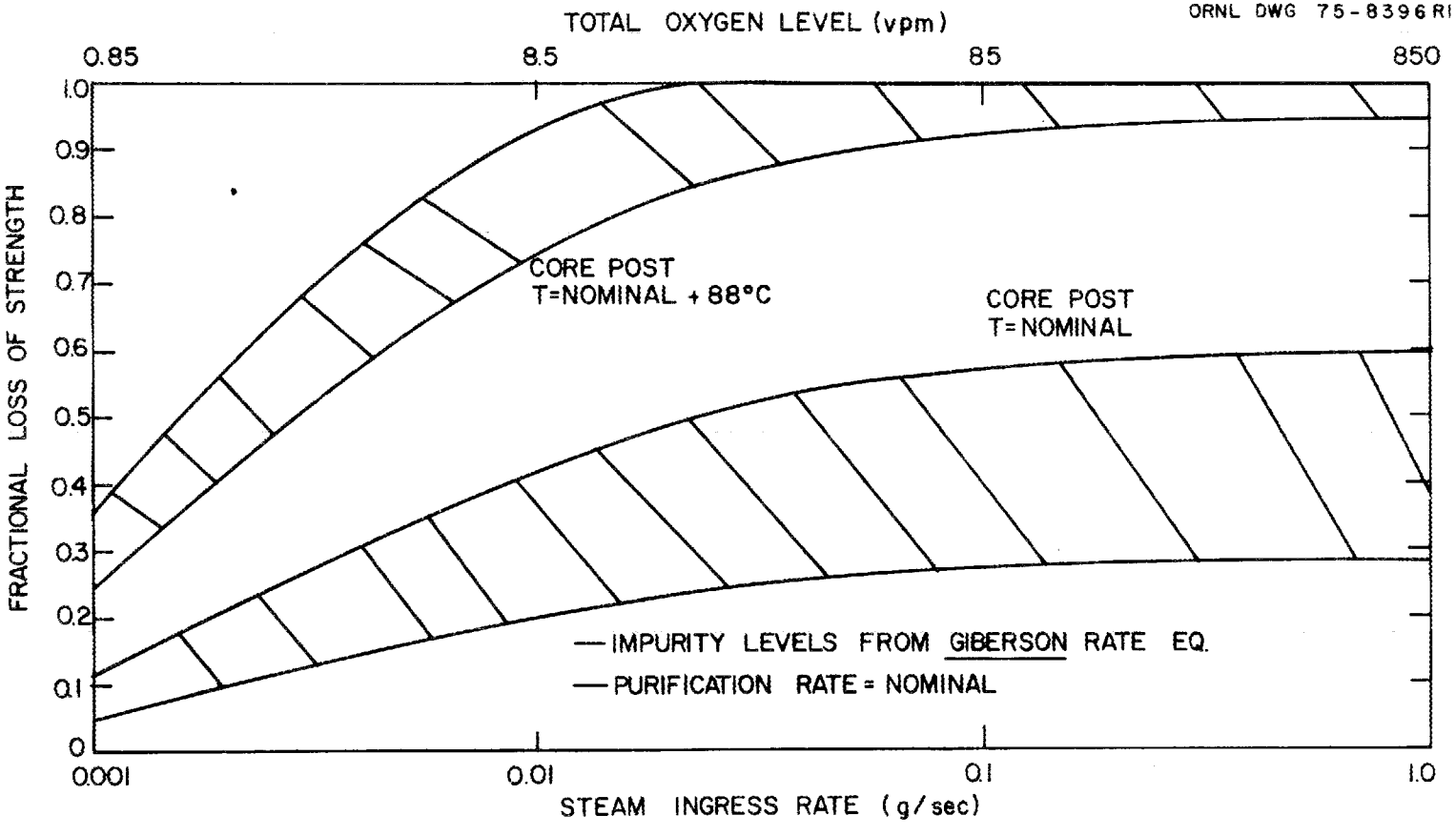

Fig. B.4. Forty-year core post strength loss vs steam ingress rate.

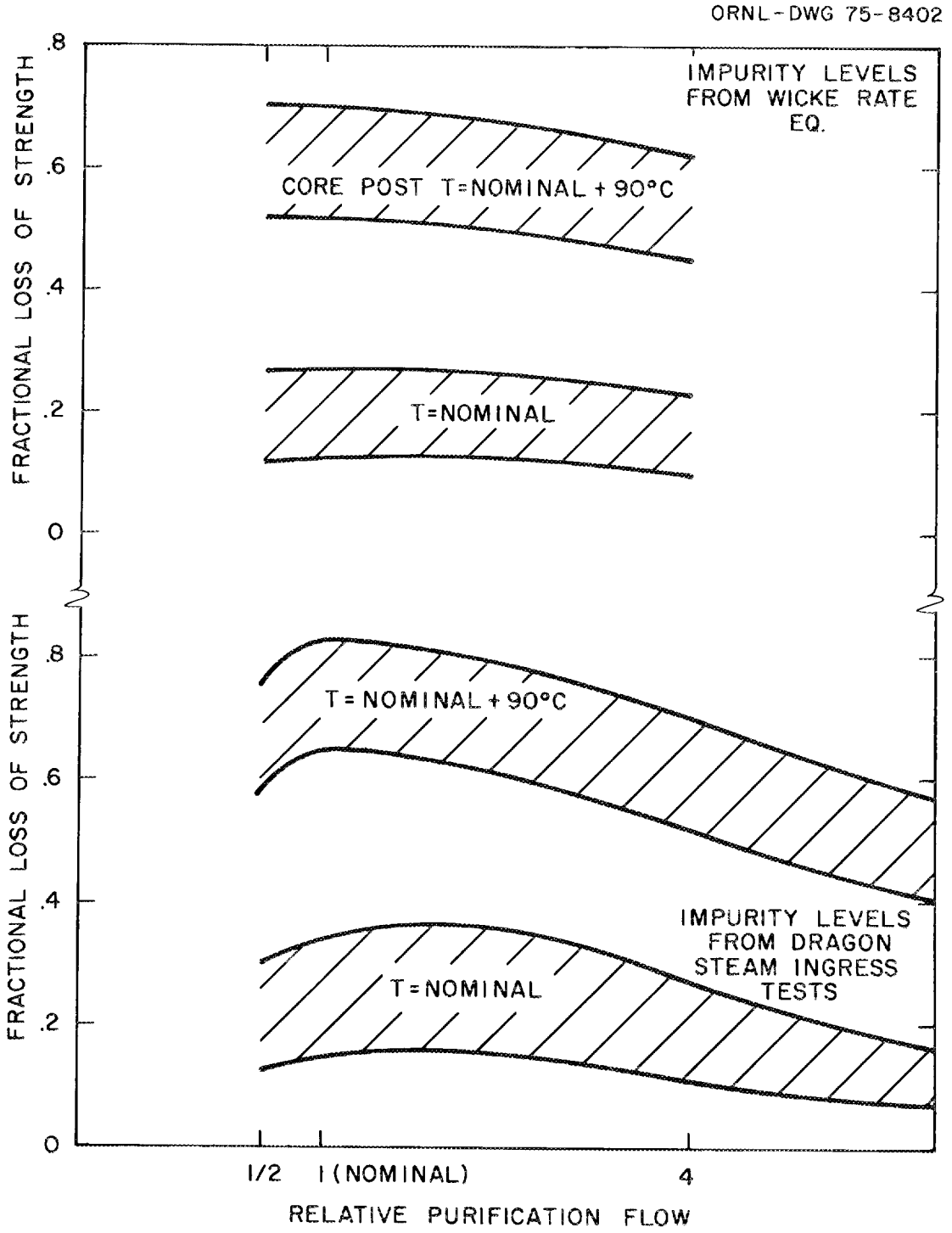

Fig. B.5. Loss of core post strength vs purification flow rate. Assumed ingress rate = 0.01 g/sec.

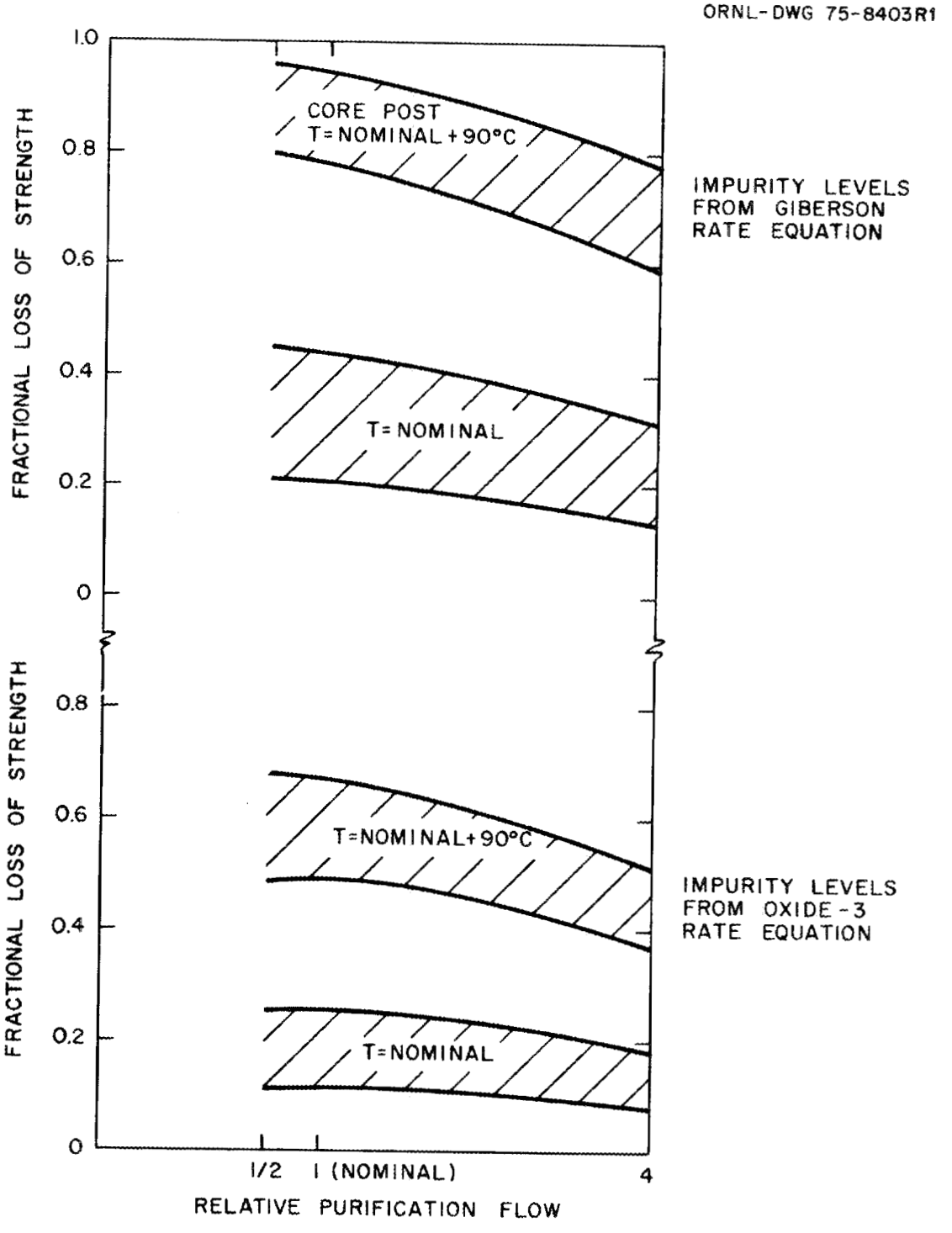

Fig. B.6. Loss of core post strength vs purification flow. Assumed ingress rate = 0.01 g/sec.

purification flow removes materials which inhibit the corrosion reaction as well as augment it. Not until purification rates of about six times the nominal are reached is significant improvement of the behavior at the higher core post temperature achieved.

The above conclusion is reached in Sect. 6.4.2 by superimposing results from the four methods of calculating the impurity compositions. Since the reference core graphite, H-451, could behave differently from the composite of these four cases, the calculations should be repeated when the reaction rate equation for H-451 becomes available.

NOMENCLATURE

A_c	Core surface area, cm^2
BO	Burnoff, mg/cm^2 or g/cm^2
D	Diameter, cm
d_j	Flaw diameter in tubing
f(x)	Probability that 50% strength loss is caused by x burnoff about dx
FSL	Fractional strength loss
K_c	Core reactivity to steam corrosion, mol/cm^3
k_i	Reaction rate constants
m	Specimen mass active in corrosion
m_T	Total specimen mass
M_w	Molecular mass, g/mol
P	Pressure, atm
P_T	Total pressure of inert plus reactive species
P(T)	Penetration parameter for strength loss equation
P_{50}	Probability for 50% strength loss
Q	Volumetric flow
Q_p	Purification flow, cm^3/sec
R	Gas constant
R	Radius, cm
R_s	Reaction rate based on exposed surface, mol/cm^2-hr
R_v	Reaction rate based on mass, g/g-hr
T	Temperature
t	Time
u_j	Velocity of steam or water in tubing flaw
V	Primary system volume, cm^3
W	Graphite width, cm
W_s	Steam ingress rate, mol/sec
w_s	Steam ingress rate, mass/time
x_1, x_2	Lower and upper range of predicted burnoffs
y_1, y_2	Lower and upper range of burnoffs for 50% strength loss

ΔH	Activation energy, cal/mol
Δh	Active corrosion depth, cm
ρ	Density, g/cm^3
μ	Partial pressure, μatm
δt	Time interval, sec
[ ]	Concentration, mol/cm^3

ORNL/TM-5534
Dist. Category UC-77

INTERNAL DISTRIBUTION

1. J. L. Anderson
2. S. J. Ball
3. D. E. Bartine
4. C. D. Baumann
5. R. L. Beatty
6. J. P. Callahan
7. D. A. Canonico
8. C. E. Clifford
9. J. A. Conlin
10. J. H. Coobs
11. D. A. Costanzo
12. F. C. Davis
13. J. R. DiStefano
14. B. C. Duggins
15. W. P. Eatherly
16. D. E. Ferguson
17. Uri Gat
18. A. G. Grindell
19. W. S. Groenier
20. P. A. Hass
21. W. R. Hamel
22. F. E. Harrington
23. C. C. Haws
24. L. C. Hensley
25. R. M. Hill, Jr.
26. F. J. Homan
27. J. R. Horton
28. Vivian Jacobs
29. J. D. Jenkins
30. D. R. Johnson
31-33. P. R. Kasten
34. W. J. Lackey
35. K. H. Lin
36. T. B. Lindemer
37. E. L. Long, Jr.
38. A. L. Lotts
39. R. E. MacPherson
40. A. P. Malinauskas
41. W. R. Martin
42. K. J. Notz
43. L. C. Oakes
44. A. R. Olsen
45. W. H. Pechin
46. H. Postma
47. R. H. Rainey
48. D. P. Reid
49. A. D. Ryon
50. J. P. Sanders
51. Dunlap Scott
52. J. D. Sease
53. J. H. Shaffer
54. R. L. Shepard
55. J. W. Snider
56. P. R. Stein
57. R. S. Stone
58. M. L. Tobias
59. J. E. Van Cleve
60. V. C. A. Vaughen
61-70. R. P. Wichner
71. R. G. Wymer
72-73. Central Research Library
74. Document Reference Section
75. Laboratory Records, ORNL-RC
76-85. Laboratory Records
86. Ken Davis (consultant)
87. E. L. Gaden, Jr. (consultant)
88. C. H. Ice (consultant)
89. R. B. Richards (consultant)

EXTERNAL DISTRIBUTION

90. Research and Technical Support Division, ERDA-ORO, P. O. Box E, Oak Ridge, Tn. 37830
91. Director, Reactor Division, ERDA-ORO, P. O. Box E, Oak Ridge, Tn. 37830
92-93. Director, Division of Nuclear Fuel Cycle and Production, ERDA, Washington, D.C. 20545
94-95. Director, Division of Reactor Research and Development, ERDA, Washington, D.C. 20545
96-266. Given distribution as shown in TID-4500 under category UC-77-Gas-Cooled Reactor Technology

U.S. GOVERNMENT PRINTING OFFICE: 1976-748-189/9